

Diss. ETH No. 22552

Lattice Boltzmann Models for Relativistic Hydrodynamics and Magnetohydrodynamics

A thesis submitted to attain the degree of
DOCTOR OF SCIENCES of ETH ZURICH

presented by

FARHANG MOHSENI

MSc. Mechanical Engineering, University of Tabriz, Iran

born on 03.08.1986

citizen of Iran

accepted on the recommendation of

Prof. Dr. Hans J. Herrmann, examiner

Prof. Dr. Sauro Succi, co-examiner

Prof. Dr. Bastien Chopard, co-examiner

2015

Acknowledgment

First, I would like to thank Prof. Hans Herrmann for supervising this thesis and guidance in this work. I am grateful for the chance he gave me to work in collaboration with many talented colleagues in a truly multidisciplinary environment which allowed me to grow as a researcher. My special thanks go to Dr. Miller Mendoza, who patiently helped me through all the steps of this work. I really appreciate all his brilliant ideas and suggestions. I enjoyed and learned a lot under his expert guidance. I also thank Prof. Sauro Succi for co-supervising this work and all the valuable recommendations to improve the quality of this study. I would also like to thank Prof. Chopard and Prof. Flatt for serving as my committee members.

During my Ph.D. studies, I had a great time at Comphys group at ETH Zürich and I want to thank every member of our group for their friendly attitude and all the enjoyable activities and helpful discussions. Also to Jens-Daniel Debus for translating the abstract to German.

Moreover, I should thank the financial support from the European Research Council (ERC) Advanced Grant 319968-FlowCCS and of the Eidgenössische Technische Hochschule Zürich (ETHZ) under Grant No. 0611-1.

Additionally, I would like to thank my parents for their support during all the years of my studies. And last but not least, I thank my beloved wife for supporting me for everything, and especially for encouraging me throughout this experience.

Contents

1	Introduction	1
2	Relativistic Lattice Boltzmann Model	11
2.1	Lattice Boltzmann method	11
2.2	Special Relativity	13
2.3	Relativistic Boltzmann equation	18
2.4	Model description	21
2.4.1	Basic Model	21
2.4.2	Extended model for high velocities	29
2.5	Validation and results	32
2.5.1	Astrophysical application	43
2.6	Summary	46
3	Relativistic Richtmyer-Meshkov Instability	49
3.1	Extensions to the relativistic lattice Boltzmann	49
3.2	Results and discussions	52
3.2.1	Numerical Simulation	52
3.2.2	Linear stability analysis	59
3.2.3	Linear and nonlinear perturbation amplitude	62
3.3	Cooling effect of Richtmyer-Meshkov instability	67
3.4	Summary	76
4	LB Model for Relativistic Magnetohydrodynamics	79
4.1	Magnetohydrodynamics	79
4.2	The resistive relativistic MHD equations	82

4.3	Lattice Boltzmann model for resistive relativistic MHD	84
4.3.1	Relativistic fluid equations	84
4.3.2	Maxwell equations	86
4.3.3	Coupling between fluid and electromagnetic fields . . .	91
4.4	Test simulations and applications	92
4.4.1	Propagation of Alfvén wave	93
4.4.2	Evolution of self-similar current sheets	95
4.4.3	Magnetic reconnection driven by Kelvin-Helmholtz in- stability	99
4.4.4	Three-dimensional magnetic reconnection in a stellar flare	107
4.5	Summary	112
5	Discussion and Outlook	115
	References	119

List of Figures

2.1	Representation of two inertial systems.	14
2.2	Comparison between the Maxwell Jüttner distribution function and the zeroth, first, and second order expansions in one space dimension for $\beta = 0.2$. In the inset, $F_{(0)}$, $F_{(1)}^x$ and $F_{(2)}^{xx}$ polynomials, in the local rest frame are shown.	25
2.3	D3Q19 lattice configuration.	27
2.4	Comparison between the velocity profile of the basic model and BAMPS, for different values of η/s at weakly relativistic regime.	34
2.5	Comparison between the basic model and the previous LBS model at different η/s , for (a) the pressure and (b) velocity profiles in the weakly relativistic regime.	35
2.6	Comparison between the basic model and the previous LBS model at $\eta/s = 0.01$, for (a) the pressure and (b) velocity profiles in the moderately relativistic regime.	36
2.7	Comparison between the basic and extended models for (a) the pressure and (b) velocity profiles in the moderately relativistic regime.	37
2.8	Comparison between the extended model and analytical results for (a) the pressure and (b) velocity profiles in the highly relativistic regime.	39
2.9	Comparison of the results for the nearly-inviscid case and different η/s , for (a) the pressure and (b) velocity profiles in the highly relativistic regime.	40

2.10	Results of the simulation for (a) the velocity profile and (b) Lorentz's factor in the ultra-high relativistic regime.	41
2.11	Snapshots of the three-dimensional simulation of a relativistic shock wave colliding with a massive interstellar cloud for (a) the weakly relativistic regime and (b) highly relativistic regime.	44
2.12	(a) Pressure, (b) density and (c) temperature profiles in the weakly and highly relativistic regimes, for the nearly-inviscid and viscous cases.	45
3.1	Schematic of the initial condition of the two-dimensional shock tube RM instability.	52
3.2	Snapshots of the density field in the shock tube RM instability for $\rho_L/\rho_M = 28$ and $Ma_r = 2.4$ at different times.	54
3.3	Snapshots of the vorticity field in the shock tube RM instability for $\rho_R/\rho_L = 14$ and $Ma_r = 2.4$ at different times.	55
3.4	Comparison of the density field in the 2D shock tube RM instability for (a) relativistic case and (b) non-relativistic case when $\rho_L/\rho_M = 28$ and $Ma_r = Ma = 2.4$ at different times.	57
3.5	Snapshots of the spikes in the 3D shock tube RM instability with square cross section when the pre-shock density ratio is 28 and the Mach number is 2.4 for (a) relativistic and (b) non-relativistic case.	58
3.6	Snapshots of the density field in the 2D shock tube non-relativistic RM instability with $\rho_L/\rho_M = 8$ and $Ma = 2.4$	62
3.7	Results of the numerical simulation $h(t)$ versus time for different Ma_r and density ratios in the linear regime.	63
3.8	Results of the numerical simulation $h(t)$ versus time for different Ma_r and density ratios in the nonlinear regime. In the inset, $h(t)$ versus time for different values of viscosities are presented for $Ma_r = 2.2$, $\rho_L/\rho_M = 20$	65

3.9	Perturbation growth rate in the linear regime as a function of temperature for different equations of state. In the inset, the effect of increasing $\beta = \Delta u/c$ on the perturbation growth rate in the linear regime (using the ideal gas equation of state), for different temperatures, comparing with the non-relativistic RM instability is shown.	66
3.10	Snapshots of the density profiles for two interacting Mach cones in a relativistic fluid at different times.	69
3.11	Decrease in the average temperature of a relativistic fluid due to the RM instability developed as a result of the interaction of two Mach cones, for different initial temperatures.	70
3.12	Snapshots of the density and temperature field in the shock tube RM instability with perturbed interface.	72
3.13	Decrease of the average temperature due to the RM instability in a shock tube numerical experiment, for different density ratios.	73
3.14	Two particle correlation (TPC) function for interacting and non-interacting Mach cones (a) before the interaction and (b) after the interaction.	74
4.1	The D3Q13 lattice configuration for the LB model to solve the Maxwell equations.	87
4.2	The configuration of the auxiliary vectors for the LB model to solve the Maxwell equations.	89
4.3	Results of the numerical test for the propagation of Alfvén waves in the limit of ideal MHD ($\sigma = 10^5$) for (a) magnetic field in z -direction and (b) electric field in x -direction.	94
4.4	Results of the numerical test for the evolution of a current sheet in the resistive regime, for two values of the conductivity, i.e. $\sigma = 100$ and $\sigma = 50$	97

4.5	Results of the convergence test for the simulation of the evolution of a current sheet in the resistive regime with $\sigma = 100$ in a log-log plot. In the inset the speedup obtained by using the openMP parallelizing method is reported versus the number of threads.	98
4.6	Snapshots of the density for the KH instability at different times for the case with $\sigma = 100$, $\Delta n = 1.8$, $U_0 = 0.6c$	101
4.7	Reconnection rate versus time for the case $\sigma = 100$, $\Delta n = 1.8$ for different values of U_0 . In the inset the results are shown for two different values of $\Delta n = 1.8$ and $\Delta n = 0$ for $\sigma = 100$	102
4.8	Snapshots of the density for the KH instability at different times, for the case with $\sigma = 100$, $\Delta n = 0$, $U_0 = 0.6c$	104
4.9	Reconnection rate versus time for the case $\Delta n = 1.8$ and $U_0 = 0.2c$ for different values of σ	105
4.10	$R(t = t_1)$ for different values of σ based on the numerical results along with best fitting curves using the proportionality relation for the Sweet-Parker and Petschek models.	107
4.11	Snapshots of the 3D magnetic reconnection in a stellar flare due to the shear flow at different times.	110
4.12	Projection of the results presented in Fig. 4.11 onto the xz plane.	111

Zusammenfassung

Im Rahmen dieser Arbeit entwickeln wir Lattice Boltzmann (LB) Modelle zur Beschreibung verschiedener physikalischer Phänomene im Bereich der relativistischen Hydrodynamik und Magnetohydrodynamik. Zunächst leiten wir ein relativistisches LB Modell her, mit dem relativistische Fluide mit ultrahohen Geschwindigkeiten, d.h. mit Lorentz-Faktoren bis zur Ordnung $\gamma \sim 10$, im Rahmen der kinetischen Gastheorie beschrieben werden können. Im Rahmen dieses Modells entwickeln wir die Maxwell-Jüttner-Verteilung nach einer Basis orthogonaler Polynome und verwenden dabei eine spezielle Quadratur, um die diskrete Form der relativistischen Boltzmann-Gleichung und der entsprechenden Gleichgewichtsverteilung zu erhalten. Um ultrahohe Geschwindigkeiten zu erzielen, verwenden wir in der diskreten relativistischen Boltzmann-Gleichung ein Flux-Limiter Schema sowie eine geeignete Erweiterung der Volumenviskosität. Wir validieren unser Modell, indem wir Schockwellen in viskosen Quark-Gluon-Plasmen simulieren, wobei wir eine gute Übereinstimmung mit bereits existierenden Modellen feststellen. Ausserdem zeigen wir, dass unser Modell auch für niederviskose Fluide mit sehr hohen Geschwindigkeiten angewendet werden kann. Als astrophysikalisches Beispiel simulieren wir die Kollision zwischen einer bei einer Supernova-Explosion erzeugten relativistischen Schockwelle mit einer massiven interstellaren Gaswolke, z.B. einer Molekülwolke.

Als weitere Anwendungen unseres Modells studieren wir die relativistischen Effekte auf die Richtmyer-Meshkov (RM) Instabilität. Dabei zeigt sich, dass die RM Instabilität im Vergleich zum nicht-relativistischen Fall aufgrund von relativistischen Effekten abgeschwächt ist, und zwar sowohl in zwei- also

auch in dreidimensionalen Systemen. Diese numerischen Resultate vergleichen wir mit einer analytischen linearen Stabilitätsanalyse und finden eine sehr gute Übereinstimmung. Darüberhinaus stellen wir auf der Basis der numerischen Ergebnisse eine allgemeine Gleichung zur Charakterisierung der nicht-linearen Zeitentwicklung der Instabilität auf. Wir zeigen, dass durch die Anwesenheit von Jet-Teilchen Schockwellen in der Form von Mach-Kegeln erzeugt werden. Die Wechselwirkung zwischen mehreren dieser Schockwellen kann die RM Instabilität auslösen und schliesslich zur Abkühlung der Flüssigkeit führen. Um den beobachteten Abkühlungseffekt zu bestätigen, führen wir zusätzlich Stossrohr-Simulationen für die RM Instabilität durch. Als experimentelle Observable für die RM Instabilität messen wir hierbei die 2-Teilchen-Korrelationsfunktion und arbeiten die Effekte der Wechselwirkung heraus. Die Simulationen der RM Instabilität sowie der Mach-Kegel werden mit einer erweiterten Version unseres relativistischen LB Modells, welche auch die ideale Gasgleichung sowie externe Kräfte berücksichtigt, durchgeführt.

Auf der Basis unseres relativistischen LB Modells sowie eines LB Modells zum Lösen der Maxwellgleichungen entwickeln wir ein kombiniertes Modell für die relativistische Magnetohydrodynamik (MHD). Obwohl unser Modell für die resistive MHD hergeleitet wird, zeigt sich, dass es auch im hochleitfähigen Limes (ideale MHD) numerisch robuste Ergebnissen liefert. Um unser Modell zu validieren, führen wir verschiedene Testsimulationen sowohl im idealen als auch im resistiven Limes durch. Im idealen Limes betrachten wir die Ausbreitung von Alfvén-Wellen, während wir im resistiven Limes die Zeitentwicklung von Stromschichten studieren. In beiden Fällen beobachten wir eine sehr gute Übereinstimmung mit den analytischen Resultaten. Darüberhinaus untersuchen wir das Phänomen der durch die Kelvin-Helmholtz Instabilität getriebenen magnetischen Rekonnexion und erforschen den Einfluss verschiedener Parameter auf die Rekonnexionsrate. Es zeigt sich hierbei, dass das Dichteverhältnis einen vernachlässigbaren Effekt auf die Rekonnexionsrate besitzt, während ein Anstieg der Schergeschwindigkeit einen Abfall der Rekonnexionsrate zur Folge hat. Die Rekonnexionsrate ist dabei proportional zu $\sigma^{-\frac{1}{2}}$ (wobei σ die Leitfähigkeit bezeichnet) und stimmt damit

mit dem Sweet-Parker Modell überein. Schliesslich verwenden wir unser numerisches Modell, um magnetische Rekonnexion in stellaren Flares zu untersuchen. Eine dreidimensionale Simulation einer stellaren Eruption deutet darauf hin, dass die Schergeschwindigkeiten in der Photosphäre für die Rekonnexion zwischen den magnetischen Feldlinien des Hintergrundfeldes und den Feldlinienbündeln verantwortlich sind.

Die von uns entwickelten LB Modelle für die Hydrodynamik und Magneto-hydrodynamik profitieren von den bekannten Vorteilen der LB Methode, insbesondere von Effizienz und von der einfachen Handhabung komplexer Geometrien.

Summary

In this work we develop lattice Boltzmann (LB) models for relativistic hydrodynamics and magnetohydrodynamics and we demonstrate their applications in simulating relevant physical phenomena. First, a relativistic LB model capable of describing relativistic fluid dynamics at ultra-high velocities, with Lorentz factors up to $\gamma \sim 10$ is derived. To this purpose, we first build a new lattice kinetic scheme by expanding the Maxwell-Jüttner distribution function in an orthogonal basis of polynomials and applying an appropriate quadrature, providing the discrete versions of the relativistic Boltzmann equation and the equilibrium distribution. To achieve ultra-high velocities, we include a flux limiter scheme, and introduce the bulk viscosity by a suitable extension of the discrete relativistic Boltzmann equation. The model is validated by performing simulations of shock waves in viscous quark-gluon plasmas and comparing with existing models, finding very good agreement. Moreover, we show that our model can also be used for low-viscous flows even at very high velocities. As an astrophysical example, we simulate a relativistic shock wave, generated by a supernova explosion, colliding with a massive interstellar cloud, e.g. molecular gas.

As an application for the model, a detailed investigation of the relativistic effects on the Richtmyer-Meshkov (RM) instability is presented. It is found that the relativistic effects weaken the RM instability as compared to the non-relativistic case, both in two and three spatial dimensions. Linear stability is studied analytically and compared with numerical results in the linear growth regime. Also, based on the numerical results, a general expression characterizing the nonlinear evolution of the instability, is proposed.

Additionally, we provide numerical evidence that the Richtmyer-Meshkov instability contributes to the cooling of a relativistic fluid. We show that due to the presence of jet particles traveling throughout the medium, shock waves are generated in the form of Mach cones. The interaction of multiple shock waves can trigger the RM instability, and we have found that this process leads to a down-cooling of the relativistic fluid. To confirm the cooling effect of the instability, shock tube RM instability simulations are performed. Furthermore, in order to provide an experimental observable of the RM instability resulting from the Mach cone interaction, we measure the two particle correlation function and highlight the effects of the interaction. The simulations of the RM instability and Mach cones are performed by an extended version of the relativistic LB model which includes the ideal gas equation of state and external forces.

Based on our relativistic LB model and an LB solver for the Maxwell equations, we develop an LB model for relativistic magnetohydrodynamics (MHD). Even though the model is derived for resistive MHD, it is shown that it is numerically robust even in the high conductivity (ideal MHD) limit. In order to validate the numerical method, test simulations are carried out for both ideal and resistive limits, namely the propagation of Alfvén waves in the ideal MHD and the evolution of current sheets in the resistive regime, where very good agreement is observed comparing to the analytical results. Additionally, two-dimensional magnetic reconnection driven by Kelvin-Helmholtz instability is studied and the effects of different parameters on the reconnection rate are investigated. It is shown that the density ratio has negligible effect on the magnetic reconnection rate, while an increase in the shear velocity decreases the reconnection rate. Also it is found that the reconnection rate is proportional to $\sigma^{-\frac{1}{2}}$, with σ being the conductivity, which is in agreement with the scaling law of the Sweet-Parker model. Finally, the numerical model is used to study the magnetic reconnection in a stellar flare. Three-dimensional simulation suggests that the reconnection between the background and flux rope magnetic lines in a stellar flare can take place as a result of a shear velocity in the photosphere.

Our proposed LB models for hydrodynamics and magnetohydrodynamics

open up the possibility of exporting the proven advantages of LB methods, namely computational efficiency and easy handling of complex geometries, to the context of relativistic fluid dynamics.

Chapter 1

Introduction

Relativistic fluid dynamics plays an important role in many contexts of astrophysics, nuclear and high-energy physics, e.g. jets emerging from the core of galactic nuclei or gamma-ray bursts [8], shock induced Richtmyer-Meshkov instabilities [88] and quark-gluon plasmas produced in heavy-ion collisions [104]. Another system that behaves as a relativistic fluid, is the electronic gas in graphene [89, 90] where many of its fascinating properties are partially related to the fact that due to the special symmetries of the honeycomb lattice, graphene is a very special, slow-relativistic electronic fluid [84, 75].

The dynamics of flows in such systems requires solving highly nonlinear equations, rendering the analytic treatment of practical problems extremely difficult. Hence, various numerical methods have been developed to study the relativistic hydrodynamics. Most of these methods are focussed on the solution of the corresponding relativistic macroscopic conservation equations. Among others, one can mention the methods based on second-order Lax-Wendroff scheme [25], smoothed particle hydrodynamics techniques [47, 105], Glimm's (random choice) method [121] and high resolution shock-capturing methods [36]. Other methods, instead of solving the macroscopic equations, tackle the problem from the microscopic and mesoscopic points of view [126].

To this regard, the lattice Boltzmann (LB) method [4, 15, 108] a relatively new numerical approach, based on a minimal lattice version of the Boltzmann kinetic equation, has enjoyed increasing popularity for the last two decades. Within LB, representative particles stream and collide on the nodes of a reg-

ular lattice, with sufficient symmetry to reproduce the correct equations of macroscopic hydrodynamics. The main highlights of LB are its computational simplicity, easy handling of complex geometries, and high amenability to parallel computing [112]. The LB method has met with remarkable success for the simulation of a broad variety of complex flows, from fully developed turbulence, all the way down to nanoscale flows of biological interest [71, 49, 109].

From a mathematical viewpoint, the standard lattice Boltzmann model can be obtained by expanding the equilibrium distribution, i.e. Maxwell-Boltzmann distribution, in Hermite polynomials up to a certain order [103], and applying the Bhatnagar-Gross-Krook (BGK) approximation for the collision operator [7]. While the applications of the LB scheme cover an impressive array of complex fluid flows, its relativistic extension has been developed only in last few years [74, 73].

The idea of the relativistic LB model was based on the observation that the kinetic formalism is naturally covariant, hyperbolic and conservative. The model was constructed using the moment-matching procedure, which means that the local kinetic equilibrium is expressed as parametric polynomial of the relativistic fluid velocity $\beta = |\vec{u}|/c$, \vec{u} being the typical flow speed and c the speed of light, with the Lagrangian parameters fixed by the condition of matching the moments of the Maxwell-Jüttner distribution in continuum velocity space.

It is worth mentioning that Jüttner derived a relativistic analogue of the Maxwell-Boltzmann equilibrium distribution for classical gases by using an entropy maximization procedure, subject to the relativistic energy-momentum constraints [54], and proposed a form of the equilibrium distribution function (Maxwell-Jüttner distribution) for relativistic particles. Recently, conclusive evidence for the original form proposed by Jüttner has been brought by numerical simulations of fully relativistic molecular dynamics in one and two dimensions [22, 83].

Relativistic LB model was shown capable of simulating weakly and moderately relativistic viscous flows, with $\beta \sim 0.3$. In fact, weakly/moderately relativistic flows are relevant for some applications such as, quark-gluon

plasma generated by recent experiments on heavy-ions and hadron jets [33, 30, 32, 34, 35, 31, 29], as well as some astrophysical flows, such as interstellar gas and supernova remnants [69, 28]. In particular, the relativistic LB was applied to the simulation of shock waves in quark-gluon plasmas, showing very good agreement with the results obtained by solving the full Boltzmann equation, using a numerical model called Boltzmann Approach for Multi-Parton Scattering (BAMPS) [10].

However, apart from the fact that this model can not handle strongly relativistic flows, the aforementioned matching procedure does not provide a unique solution for the discrete equilibrium distribution function, satisfying the hydrodynamics moments of the Maxwell-Jüttner distribution. It is therefore highly desirable to develop more general and systematic approaches which are capable of simulating relativistic flows with higher velocities.

To this purpose, let us observe that, due to the non-separability of the Maxwell-Jüttner distribution function into the three components of the momentum in Cartesian coordinates, its expansion in orthogonal polynomials is not as natural as in the classical case and some deliberation is required. For the fully relativistic regime, neglecting particle masses, and by using spherical coordinates, a lattice Boltzmann algorithm for the relativistic Boltzmann equation was developed in Ref. [100], where the Maxwell-Jüttner distribution function was expanded in an orthogonal polynomials basis and discretized using a Gauss quadrature procedure. The model was based on the Anderson-Witting collision operator [1]. The results of simulating viscous quark-gluon plasma were compared to other hydrodynamic simulations and very good agreement was observed. However, using spherical coordinates one gets spherical lattices which are not space filling, and consequently, in the streaming procedure, a linear interpolation is required at each time step. Therefore, some crucial properties of the classical LB, e.g. exact streaming and zero numerical dispersion, are lost in the process.

In this work, we develop a relativistic lattice Boltzmann model by expanding the Maxwell-Jüttner distribution in a set of orthogonal polynomials, and performing an appropriate quadrature in order to adjust the scheme to a D3Q19 (19 discrete velocities in three spatial dimensions) cell configuration.

Moreover, we extend the model by using a minimum modulus flux limiter scheme and introducing the bulk viscosity term into the Boltzmann equation. We show that the model is numerically stable also at very high velocities, i.e. Lorentz factors up to $\gamma \sim 10$. Additionally, we show that this model can also be used to simulate nearly-inviscid flows, which corresponds to solve the Euler equation on the macroscopic level. This is well suited for astrophysical applications, where the viscosity is usually negligible. In fact, the astrophysical context presents possibly the richest arena for applications of the present relativistic LB scheme.

The relativistic lattice Boltzmann methods fill a missing entry in the remarkably broad spectrum of LB applications across most areas of fluid dynamics, including quantum fluids [110]. Relativistic LB approaches might nevertheless offer a fairly inexpensive alternative to more sophisticated methods mentioned before. In addition, since LB is recognized as an excellent solver for flows in complex geometries it is plausible to expect that the present relativistic LB scheme may play a useful role for the simulation of relativistic flows in non-idealized geometries. We provide indications that the relativistic LB stands concrete chances of carrying the recognized advantages of LB schemes for classical fluids, over to the relativistic context. The description of the model along with some applications are presented in Ch. 2.

Having a strong numerical model for relativistic fluid dynamics, as a particular application for the model, we study the relativistic effects on the Richtmyer-Meshkov (RM) instability. The RM instability is one of the fundamental fluid instabilities, which occurs whenever a shock wave passes through an interface, separating two fluids with different densities. This instability was theoretically predicted by Richtmyer [97] and experimentally detected by Meshkov [79] in the non-relativistic context. The study of the RM instability is also of great importance in several phenomena, ranging from high energy physics [43] to astrophysics [3], especially wherever shock-wave propagation is involved.

For instance, in a collapsing core supernova explosion, the generated shock wave propagates outwards through a hydrogen-helium interface. Observations have shown that the outer regions of the supernovae are more uniformly

mixed than expected, as a consequence of the RM instability [3]. Moreover, it is believed that in gamma-ray bursts, relativistic shocks as well as intermittent and inhomogeneous outflows play a major role [80]. Thus, we can expect that the RM instability can also appear in this context. Therefore, the study of the relativistic effects can contribute to a deeper understanding of these phenomena.

The RM instability in the non-relativistic regime has been investigated extensively [97, 124, 123, 118, 60]. However, to the best of our knowledge, systematic investigations in the relativistic regime are still lacking. Therefore, in Ch. 3, we perform numerical simulations of the relativistic RM instability using the relativistic LB model. To this purpose, the model needs to be extended to deal with the ideal gas equation of state. To single out the relativistic effects, we also provide comparisons between the relativistic and non-relativistic cases. In order to gain a deeper understanding of the instability, we develop a simple linear stability analysis for the relativistic RM instability and derive a theoretical asymptotic expression for the growth rate of the perturbation amplitude in the linear regime. Furthermore, based on our numerical results, we propose a general relation for the evolution of the instability in the nonlinear regime. Also, we analyse the growth rate of the instability for different equations of state (EoS) and show that the linear growth rate depends explicitly on the EoS, unlike the non-relativistic case. Therefore, the study of the instability can provide information on the EoS, the same way shock waves can offer insights [107, 6]. In other words, gaining information about the RM instability may provide a new means of studying the thermodynamic properties of relativistic fluids.

We know that particles traveling through a compressible fluid generate waves moving at the speed of sound. Moreover, if the particles travel faster than the speed of sound of the medium, the disturbances in the fluid are confined to the so-called Mach cone. This phenomenon is very common in many natural systems, including astrophysics and high energy physics [39, 43, 122, 64, 125], where relativistic fluid effects are important. As mentioned, the existence of relativistic shock-waves in the presence of density variations, leads to the appearance of the RM instability. Density variations can appear in relativistic

fluids whenever particles travel through the medium, due to the sweeping effect of the shock waves [102], as well as due to external mechanisms.

We show numerically that the RM instability may reduce the average temperature of the relativistic fluid. In particular, we investigate the interaction of two relativistic Mach shocks, and show that the RM instability arises due to this interaction and we find that the appearance of this hydrodynamic instability leads to a decrease in the average temperature of the medium. To justify this finding and to single out the effect of the instability, thermal behavior of the shock tube RM instability is studied. The effect of the initial domain temperature and density ratio on the cooling effect of the instability is also investigated. Furthermore, we propose a way to detect the interaction between Mach cones from an experimental observable, namely the two-point correlation function.

In the above examples we have neglected the presence of magnetic fields, however, they are an essential component of many astrophysical phenomena, such as relativistic jets [81], active galactic nuclei [2], gamma ray bursts [95], pulsar winds [12], and stellar flares [68]. Since in most of these phenomena the plasma is electrically neutral and the characteristic times between collisions are much smaller than the typical time scale of the system, the magnetohydrodynamics (MHD) approximation is appropriate. Due to the fact that relativistic effects play a major role in the dynamics of these phenomena, relativistic MHD description is of special interest in this perspective. Since the equations of relativistic MHD are extremely difficult to solve analytically, except for some simple geometries, most of the studies are based on numerical simulations.

Ideal MHD is defined as the limit where the electrical conductivity σ goes to infinity (electrical resistivity $\eta \equiv 1/\sigma \rightarrow 0$). In this framework many numerical models have been developed over the last decade dealing with the ideal relativistic MHD [57, 26, 40]. As it will be explained later, the ideal MHD assumption not only makes the solution of the relativistic MHD considerably simpler, but it is also a fairly good approximation for many high-energy phenomena. However, in several situations such as neutron star mergers [37] or central engines of gamma ray bursts [66], the conductivity

can be small and the ideal MHD assumption is not valid any longer.

More importantly, magnetic reconnection only takes place when resistivity exists in the plasma. This process is the driver of explosive events in astrophysical plasmas, in which magnetic field lines break and reconnect and the magnetic field topology goes through a sudden change. During this process, plasma releases the magnetic energy and converts it into thermal and kinetic energy on a short timescale. Magnetic reconnection has been proposed to have an influential role in many astrophysical observations, namely as a cause of particle acceleration in extragalactic jets [51], as a source of high energy emission [52], as an explanation of the rapid variability observed in active galactic nuclei [41] and many others. Therefore, studying magnetic reconnection is of great importance, especially considering the fact that the relativistic theory of magnetic reconnection is not yet well established and its mechanism is poorly understood [127]. It should be mentioned that, numerical results of ideal relativistic MHD models sometimes show magnetic reconnection, which is non-physical, since it is caused by numerical resistivity and hence depends on the details of the numerical scheme and resolution [58].

Therefore, there is a strong interest in developing numerical models for resistive relativistic MHD. However, the corresponding governing equations turn out to be numerically very challenging, since the source terms in the equations become stiff, especially when the conductivity is not small [58]. This is the natural consequence of the fact that the time-scale of the diffusive effects and the overall dynamical time-scale are of the same order. Thus, it is not surprising that the first numerical model for resistive relativistic MHD appeared only recently in 2007 [58], where the fluxes are computed by using the Harten-Lax-van-Leer (HLL) approximate Riemann solver, and the Strangs splitting technique is used for the stiff source terms. Later on, a numerical method which uses an implicit-explicit (IMEX) Runge-Kutta method to solve the stiff source terms in the equations is proposed in Ref. [91]. Also, a unified framework for the construction of one-step finite volume and discontinuous Galerkin schemes for the resistive relativistic MHD is introduced in Ref. [27]. More recently, a different approach has been suggested in Ref. [116], where

the method of characteristics is used to solve the Maxwell equations. Additionally the role of the equation of state in the resistive relativistic MHD is investigated in Ref. [82].

All the above mentioned models are based on solving the macroscopic governing equations of the resistive relativistic MHD. In Ch. 4, we develop an LB model for relativistic MHD. The model is proposed for resistive MHD but, as we will show later, it is robust enough in the ideal MHD limit as well. The hydrodynamics part is based on the model which will be described in Chs. 2 and 3, with some extensions to include the contribution of electromagnetic fields in the energy-momentum tensor (corresponding to adding the Lorentz force and Joule heating in the macroscopic equations). For the electromagnetic part, i.e., solving the Maxwell equations, the LB model for electrodynamics proposed in Ref. [78] is modified and extended for coupling with the fluid equations and to include the relativistic Ohm's law. Here again, our goal is to bring the well-known advantages of the lattice Boltzmann schemes to the context of resistive relativistic MHD.

The model is validated using numerical tests for the ideal MHD and resistive MHD regimes. In particular, the propagation of Alfvén waves in high conductivity media, and the evolution of current sheets in resistive media are validated against analytical solutions. Moreover, as an application for the model, the magnetic reconnection process driven by Kelvin-Helmholtz (KH) instability is studied in detail. The KH instability is another fundamental hydrodynamic instability which occurs during the shear flow of a uniform fluid, or two fluids with different densities. It was discovered independently by Kelvin and Helmholtz in the 19th century [55, 46]. It is believed that the KH instability appears in the solar-wind interaction with the Earth's magnetosphere which can influence the magnetic reconnection process that takes place there [38]. Moreover, the KH instability has been widely investigated for astrophysical applications, e.g. astrophysical jet morphology [63] motion of interstellar clouds [119] and clumping in supernova remnants [120], where in many of these phenomena, relativistic and magnetic field effects cannot be ignored. Here, we study the KH instability as a potential driver of magnetic reconnection. In the non-relativistic context this has been discussed in

Refs. [56, 87]. Here we focus on this phenomenon in the relativistic context and we are interested in the effects of the hydrodynamics parameters, i.e., shear velocity and density ratio, as well as the effects of the value of the conductivity on the magnetic reconnection rate.

Finally, the results of a three-dimensional simulation of the magnetic reconnection in a stellar flare driven by a shear velocity on its photosphere are presented. It has been suggested that solar flares are good prototypes for stellar flares in relativistic stars like neutron stars [68]. Therefore, a solar type initial condition, consisting of a potential quadrupole background field and a flux rope [115], is chosen to study the stellar flare. We show that the shear velocity on the photosphere of the star can cause the magnetic reconnection to take place between the flux rope and the background magnetic field lines.

Chapter 2

Relativistic Lattice Boltzmann Model

In this chapter we discuss about the description, derivation and some applications of the relativistic lattice Boltzmann model. The chapter is organized as follows: in Sec. 2.1, the basics of the LB method is briefly reviewed; in Sec. 2.2 the principles of special relativity is introduced; in Sec. 2.3, the relativistic Boltzmann equation is discussed; in Sec. 2.4, the relativistic LB model description is presented in detail; and in Sec. 2.5, several validations with other existing numerical models along with some results for shock waves in viscous quark-gluon plasmas and a 3D simulation of a shock wave colliding with a massive interstellar cloud are presented. Finally, in Sec. 2.6, discussions about the model and the results are provided.

2.1 Lattice Boltzmann method

The standard LB method reads as follows:

$$f_i(\vec{x} + \vec{c}_i \delta t, t + \delta t) - f_i(\vec{x}, t) = -\frac{\delta t}{\tau} (f_i - f_i^{eq}), \quad (2.1)$$

where $f_i(\vec{x}, t)$ is the probability of finding a particle at lattice site \vec{x} and time t , moving along the direction pointed by the discrete velocity \vec{c}_i . The left-hand side is readily recognized as an exact lattice transcription of the free-streaming term $(\partial_t + v_a \nabla_a) f$ of the continuum Boltzmann equation,

with v_a being the a component of the microscopic velocity, where the Latin index a denotes spatial coordinates and repeated indices are summed upon. The right-hand-side, on the other hand, is a discrete version of the collision operator, here taking the form of a simple relaxation around a local equilibrium f_i^{eq} on a timescale τ (single time BGK relaxation [7]). The local equilibrium encodes the conservation laws governing the ideal fluid regime, namely mass, momentum and energy conservation and Galilean invariance. While molecular details of the collisional processes can be safely foregone, these conservation properties must necessarily be preserved in the lattice formulation.

The discrete local equilibrium is usually expressed as a local Maxwellian, expanded up to second order in the local Mach number $Ma = u/c_{so}$, with u being the local flow speed and c_{so} the sound speed. For the case of isothermal flows, this takes the form

$$f_i^{eq} = w_i \rho \left(1 + \frac{c_{ia} u_a}{c_{so}^2} + \frac{Q_{iab} u_a u_b}{2c_{so}^4} \right), \quad (2.2)$$

where

$$\begin{aligned} \rho &= \sum_i f_i, \\ \rho u_a &= \sum_i f_i c_{ia}, \end{aligned}$$

are the fluid density and mass current density, respectively. In the above, w_i are discretized weights and $Q_{iab} = c_{ia} c_{ib} - c_{so}^2 \delta_{ab}$ is the projector along the i -th direction. Provided that w_i and c_i are properly chosen, it is readily checked that the local equilibria fulfil the following relations

$$\begin{aligned} \sum_i f_i^{eq} &= \sum_i f_i = \rho, \\ \sum_i f_i^{eq} c_{ia} &= \sum_i f_i c_{ia} = \rho u_a, \\ \sum_i f_i^{eq} c_{ia} c_{ib} &= \rho (u_a u_b + c_{so}^2 \delta_{ab}). \end{aligned} \quad (2.3)$$

The first two are the usual mass and momentum density, whereas the latter is the equilibrium momentum-flux tensor. Recovering the momentum flux tensor is crucial to secure the proper non-linear structure of the Navier-Stokes

equations, and indeed only specific classes of discrete lattices fulfil the aforementioned constraints. As mentioned, discretized equilibrium distribution function can be obtained by the expansion of the continuum expression of the Maxwell-Boltzmann distribution. Due to the well-known property of the local Maxwellian to serve as the generating function of Hermite's polynomials H_n , one can write (here $\vec{v} = \vec{v}/c_{so}$ and $\vec{u} = \vec{u}/c_{so}$):

$$e^{-\frac{(\vec{v}-\vec{u})^2}{2}} = e^{-\frac{v^2}{2}} \sum_{n=0}^{\infty} H_n(\vec{v}) u^n. \quad (2.4)$$

Note that the Galilean invariance manifestly encoded at the left hand side through the dependence on the magnitude of the relative speed $(\vec{v} - \vec{u})$, can only be preserved by including all terms in the Mach-number expansion at the right hand side. The fact that the Navier-Stokes equations only involve quadratic non-linearities in the flow field allows us to develop a consistent lattice hydrodynamic theory by retaining only second order terms in the Mach-number expansion. A similar line of thinking can also be applied to the relativistic equations, with due changes in the mathematical-physical details, to be discussed shortly.

2.2 Special Relativity

Before discussing the relativistic Boltzmann equation, in this section we introduce the basics of special relativity. The special theory of relativity was developed by Einstein and is based on two postulates (see Ref. [14] for more information)

- The laws of physics should be invariant in all inertial frames of references (it should be impossible for an observer to detect a uniform translational motion by measurements made by him).
- The speed of light in free space has the same value for all observers that are in inertial frames.

Inertial frame is defined as a frame with respect to which a point-like body at rest removed from the action of other bodies remains at rest. The first

postulate of special relativity states that the physical laws are identical in all inertial frames of reference, i.e., they are invariant with respect to space-time transformations between inertial systems. From the second postulate it follows that the velocity of propagation of signals is the same in all inertial systems of references, which is a universal constant, $c = 299792458 \text{ m/s}$ (speed of light in free space).

One consequence of the second postulate is that the time interval is not absolute and that the simultaneous events in one frame of reference are not simultaneous in another frame of reference. An event is characterized by the point occupied at the time it has occurred, which means it is a point in a space-time coordinate system. The set of all events form a four-dimensional space, where the events are represented by points called world points and the trajectory of a particle in space-time is called world line.

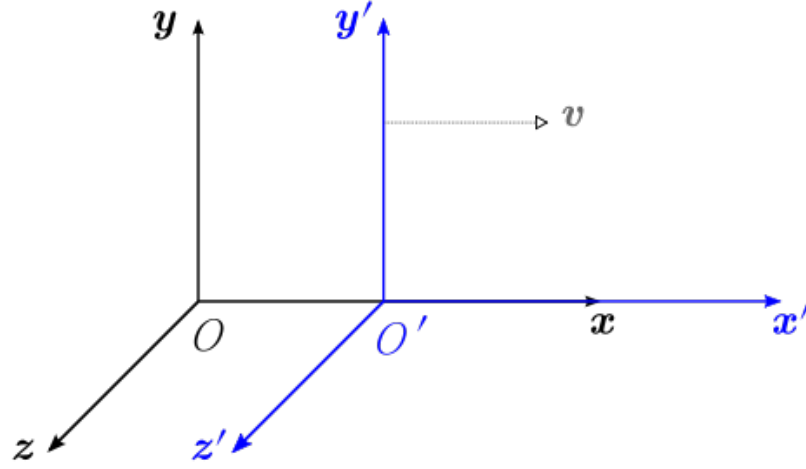


Fig. 2.1: Representation of two inertial systems.

Let us consider two reference systems O and O' such that O' has a uniform velocity v directed along the x axis in the perspective of a stationary observer in reference O , like in Fig. 2.1. The times in O and O' are denoted by t and t' , respectively. Let x_1, y_1, z_1, t_1 and x_2, y_2, z_2, t_2 be the coordinates of two events in the reference frame O . The interval between this two events s_{12}

can be defined as

$$s_{12}^2 = c^2(t_2 - t_1)^2 - (x_2 - x_1)^2 - (y_2 - y_1)^2 - (z_2 - z_1)^2. \quad (2.5)$$

For the infinitesimal close events we have

$$ds^2 = c^2 dt^2 - dx^2 - dy^2 - dz^2, \quad (2.6)$$

where one can show that $ds^2 = ds'^2$, which means the interval between two events is the same in all inertial frames of references.

We can formalize our discussion by introducing a four-dimensional space with the so-called Minkowski coordinates defined as:

$$x^0 = ct, \quad x^1 = x, \quad x^2 = y, \quad x^3 = z. \quad (2.7)$$

Using this definition, we can write Eq. (2.6) as

$$ds^2 = \eta_{\alpha\beta} dx^\alpha dx^\beta, \quad (2.8)$$

where Greek indices are used to specify the four-dimensional space-time coordinate system running from 0,1,2,3 and the Einstein summation convention over repeated indices is used. Here, $\eta_{\alpha\beta}$ are the components of the metric tensor in the four-dimensional space characterized by the element ds . This space is called Minkowski space and the metric tensor is given by:

$$(\eta_{\alpha\beta}) = \begin{pmatrix} +1 & 0 & 0 & 0 \\ 0 & -1 & 0 & 0 \\ 0 & 0 & -1 & 0 \\ 0 & 0 & 0 & -1 \end{pmatrix}. \quad (2.9)$$

If we denote the elements of the inverse matrix by $\eta^{\alpha\beta}$, we have

$$(\eta^{\alpha\beta}) = \begin{pmatrix} +1 & 0 & 0 & 0 \\ 0 & -1 & 0 & 0 \\ 0 & 0 & -1 & 0 \\ 0 & 0 & 0 & -1 \end{pmatrix}. \quad (2.10)$$

Also, the transformation matrix between the two inertial systems can be denoted by Λ_{β}^{α} . For instance,

$$x'^{\alpha} = \Lambda_{\beta}^{\alpha} x^{\beta}. \quad (2.11)$$

One can show that the transformation matrix between reference systems O and O' in Fig. 2.1 can be written as

$$(\Lambda_{\beta}^{\alpha}) = \begin{pmatrix} \frac{1}{\sqrt{1-v^2/c^2}} & \frac{-v/c}{\sqrt{1-v^2/c^2}} & 0 & 0 \\ \frac{-v/c}{\sqrt{1-v^2/c^2}} & \frac{1}{\sqrt{1-v^2/c^2}} & 0 & 0 \\ 0 & 0 & 0 & 0 \\ 0 & 0 & 0 & 0 \end{pmatrix}. \quad (2.12)$$

Thus, the Lorentz transformation for this two systems are

$$x'^1 = \frac{x^1 - vt}{\sqrt{1 - v^2/c^2}}, \quad x'^2 = x^2, \quad x'^3 = x^3, \quad t' = \frac{t - x^1 v/c^2}{\sqrt{1 - v^2/c^2}}. \quad (2.13)$$

As a particular case of the Lorentz transformation, when the velocities are small relative to the light speed ($v \ll c$) we obtain the Galilean transformations:

$$x'^1 = x^1 - vt, \quad x'^2 = x^2, \quad x'^3 = x^3, \quad t' = t. \quad (2.14)$$

In this context we can introduce the concept of proper time of a particle which is the time measured by a clock that moves with the particle, and is denoted by τ (not to be confused with the relaxation time in the lattice Boltzmann equation) and for the system O' we have $t' = \tau$. Thus, we can obtain

$$d\tau = dt' = dt \sqrt{1 - v^2/c^2}. \quad (2.15)$$

This means the time interval in the system O at rest is longer than the time interval in the system O' that is moving with velocity v (time dilation).

Another consequence of the Lorentz transformation is Lorentz contraction. We consider a rod parallel to the x axis which has a proper length given by $l_0 = x_A^1 - x_B^1$ with A and B denote the end points of the rod. By denoting $l = x_A'^1 - x_B'^1$ as the length of the rod in the frame of reference O' we can obtain the Lorentz contraction as

$$l = l_0 \sqrt{1 - v^2/c^2}. \quad (2.16)$$

This means the a rod has its largest length in a system at rest.

The general transformation law for two inertial systems in which one of them is moving with a relative velocity, $\vec{u} = (u_1, u_2, u_3)$, with an arbitrary direction with respect to the other is given by

$$(\Lambda_\beta^\alpha) = \begin{pmatrix} \gamma & -\gamma \frac{u^1}{c} & -\gamma \frac{u^2}{c} & -\gamma \frac{u^3}{c} \\ -\gamma \frac{u^1}{c} & 1 + \frac{(\gamma-1)u^1 u^1}{|\vec{u}|^2} & \frac{(\gamma-1)u^1 u^2}{|\vec{u}|^2} & \frac{(\gamma-1)u^1 u^3}{|\vec{u}|^2} \\ -\gamma \frac{u^2}{c} & \frac{(\gamma-1)u^1 u^2}{|\vec{u}|^2} & 1 + \frac{(\gamma-1)u^2 u^2}{|\vec{u}|^2} & \frac{(\gamma-1)u^2 u^3}{|\vec{u}|^2} \\ -\gamma \frac{u^3}{c} & \frac{(\gamma-1)u^3 u^1}{|\vec{u}|^2} & \frac{(\gamma-1)u^3 u^2}{|\vec{u}|^2} & 1 + \frac{(\gamma-1)u^3 u^3}{|\vec{u}|^2} \end{pmatrix}. \quad (2.17)$$

Note that from now on we use the usual abbreviation

$$\gamma = \frac{1}{\sqrt{1 - |\vec{u}|^2/c^2}}, \quad (2.18)$$

where γ is the Lorentz factor.

Let us now introduce the notations related to the special relativity that we are going to use in this work. A four-vector is a quantity which can be described by four-components A^α with respect to a given reference frame, which transforms according to

$$A'^\alpha = \Lambda_\beta^\alpha A^\beta. \quad (2.19)$$

There are two representations for the components of a four-vector: the contravariant components denoted by A^α , and the covariant components denoted by A_α . These two representations are related through

$$A_\alpha = \eta_{\alpha\beta} A^\beta, \quad A_0 = A^0, \quad A_i = A^i, \quad (2.20)$$

where the Latin indices denote the three-dimensional space coordinate system running from 1, 2, 3. The contravariant and covariant components can also be represented as

$$(A^\alpha) = (A^0, \vec{A}) = (A_0, \vec{A}), \quad (A_\alpha) = (A_0, -\vec{A}). \quad (2.21)$$

The scalar product of two four-vectors A^α and B_α is defined by

$$A^\alpha B_\alpha = A^0 B_0 + A^i B_i = A^0 B_0 - \vec{A} \cdot \vec{B}, \quad (2.22)$$

where $\vec{A} \cdot \vec{B}$ is the usual scalar product of two vectors in a three-dimensional space.

The components of the gradients can be defined as

$$\left(\frac{\partial}{\partial x^\alpha}\right) = \left(\frac{\partial}{\partial x^0}, \vec{\nabla}\right), \quad \left(\frac{\partial}{\partial x_\alpha}\right) = \left(\frac{\partial}{\partial x_0}, -\vec{\nabla}\right), \quad (2.23)$$

where $\vec{\nabla}$ is the usual gradient in a three-dimensional space. We will also use the notation

$$\frac{\partial}{\partial x^\alpha} \equiv \partial_\alpha, \quad \frac{\partial}{\partial x_\alpha} \equiv \partial^\alpha. \quad (2.24)$$

When working in space-time it is convenient to define a four-velocity of a particle, U^α , as

$$U^\alpha = \frac{dx^\alpha}{d\tau}, \quad (2.25)$$

with τ being the proper time. The contravariant and covariant components of the four-velocity are given by:

$$(U^\alpha) = (c\gamma, \vec{u}\gamma), \quad (U_\alpha) = (c\gamma, -\vec{u}\gamma). \quad (2.26)$$

From the above relations it is easy to verify that $U^\alpha U_\alpha = c^2$.

The product of the rest mass of a particle m with the four velocity $p^\alpha = mU^\alpha$ defines a momentum four-vector. Thus, we have

$$(p^\alpha) = (mc\gamma, m\vec{u}\gamma) = \left(\frac{E}{c}, \vec{p}\right) = (p^0, \vec{p}), \quad (2.27)$$

where the energy of a particle is given by

$$E = cp^0 = mc^2\gamma, \quad (2.28)$$

and the scalar product of the momentum four-vector with itself is

$$p_\alpha p^\alpha = m^2 c^2. \quad (2.29)$$

2.3 Relativistic Boltzmann equation

For the case of a single non-degenerated gas, and in the absence of external forces, the relativistic Boltzmann equation reads as follows [14]:

$$\partial_\mu(p^\mu f) = \int (f'_* f' - f_* f) \Phi \sigma d\Omega \frac{d^3 p_*}{p_{*0}}. \quad (2.30)$$

In the above, $f_* \equiv f(\vec{x}, \vec{p}_*, t)$ and $f \equiv f(\vec{x}, \vec{p}, t)$ denote the distribution functions before the collision, while $f'_* \equiv f(\vec{x}, \vec{p}'_*, t)$ and $f' \equiv f(\vec{x}, \vec{p}', t)$ are the resulting ones after the collision. The base of the so-called collision cylinder is described by $\sigma d\Omega$, with σ being the differential cross section, where Ω is the solid angle, and

$$\Phi = \frac{p^0 p_*^0}{c} \sqrt{(\vec{v} - \vec{v}_*)^2 - \frac{1}{c^2} (\vec{v} \times \vec{v}_*)^2} = \sqrt{(p_*^\mu p_\mu)^2 - m^2 c^4}, \quad (2.31)$$

the Lorentz invariant flux, with \vec{v} and \vec{v}_* , the velocity of the particles with momentum \vec{p} and \vec{p}_* , respectively. The right hand side of Eq. (2.30) is the collision term, whose details fix the value of the transport coefficients in the macroscopic equations. Although the collision integral can be expressed in terms of the second kind modified Bessel functions and numerical integrations [14], simpler expressions have been proposed, along the lines of the BGK approximation for non-relativistic fluids. The first relativistic BGK, proposed by Marle [67], reads as follows:

$$\partial_\mu(p^\mu f) = \frac{m}{\tau}(f^{eq} - f), \quad (2.32)$$

where f^{eq} is a local relativistic equilibrium and τ represents a characteristic time between subsequent collisions.

The Marle model provides a good approximation of the full collision term at low temperatures [14]. A more general model, which provides a reasonable approximation of the transport coefficients at both, low and high, temperatures, was subsequently proposed by Anderson and Witting [1], and it reads as follows:

$$\partial_\mu(p^\mu f) = \frac{U^\mu p_\mu}{c^2 \tau}(f^{eq} - f), \quad (2.33)$$

with τ being the relaxation time.

Both models can reproduce at the macroscopic level the conservation equations given by

$$\partial_\mu T^{\mu\nu} = 0, \quad (2.34)$$

and

$$\partial_\mu N^\mu = 0, \quad (2.35)$$

where

$$T^{\mu\nu} = p\eta^{\mu\nu} + (\epsilon + p)\frac{U^\mu U^\nu}{c^2} + \pi^{\mu\nu}, \quad (2.36)$$

is the energy-momentum tensor, ϵ the energy density (including the rest mass energy), p the hydrostatic pressure and $\pi^{\mu\nu}$ is the dissipative component of the stress-energy tensor and

$$N^\mu = nU^\mu, \quad (2.37)$$

is the particle 4-flow, with n the number of particles per volume.

Applying the conservation rule to energy momentum tensor and particle 4-flow, we obtain the macroscopic hydrodynamic equations,

$$\partial_t(n\gamma) + \partial_a(n\gamma u_a) = 0, \quad (2.38)$$

for the conservation of particle number and

$$\partial_t((\epsilon + p)\gamma^2 - p) + \partial_a((\epsilon + p)\gamma^2 u_a) + \partial_t\pi^{00} + \partial_a\pi^{a0} = 0, \quad (2.39)$$

$$\partial_t((\epsilon + p)\gamma^2 u_b) + \partial_b p + \partial_a((\epsilon + p)\gamma^2 u_a u_b) + \partial_t\pi^{0b} + \partial_a\pi^{ab} = 0, \quad (2.40)$$

for the momentum and energy conservation. For instance, for the inviscid case (no dissipation) the momentum equation can be written in a more familiar form, using Eq. (2.40) as

$$(\epsilon + p)\gamma^2 \left(\frac{\partial \vec{u}}{\partial t} + \vec{u} \cdot \vec{\nabla} \vec{u} \right) + \vec{u} \frac{\partial p}{\partial t} + \vec{\nabla} p = 0, \quad (2.41)$$

where Eq.(2.39) is used to eliminate the time derivative of $\epsilon + p$.

The models of Marle and Anderson-Witting result in different expressions for the dissipative terms and transport coefficients. For instance, the shear viscosity using the Marle model is given by $\eta_M \simeq \frac{4p^{eq}\tau_M}{\zeta}$ for high temperatures (ultrarelativistic case), with p^{eq} the equilibrium pressure and $\zeta = mc^2/k_B T$, here k_B is the Boltzmann constant and T the temperature, while with the Anderson-Witting model yields to $\eta_A \simeq \frac{4p^{eq}\tau_A}{5}$ [14].

In general, the dissipation parameters, like the bulk viscosity, thermal conductivity and shear viscosity, are only approximations of the values obtained

by linearization of the full collision term in the relativistic Boltzmann equation, Eq. 2.30.

Finally, the equilibrium distribution in the relativistic Boltzmann equation is the Maxwell-Jüttner equilibrium distribution function which in the absence of chemical potential has the form

$$f^{\text{eq}} = A \exp(-p_\mu U^\mu / k_B T), \quad (2.42)$$

where, A is a normalization constant.

2.4 Model description

2.4.1 Basic Model

Let us start the description of our model. One can write the Maxwell-Jüttner distribution in a simpler form by introducing the following change of variables:

$$\xi^\mu = \frac{p^\mu / m}{c_s}, \quad \chi^\mu = \frac{U^\mu}{c_s}, \quad (2.43)$$

$$c_s = \sqrt{\frac{k_B T}{m}}, \quad \nu = c / c_s, \quad (2.44)$$

and therefore, by replacing the new variables in Eq. (2.42), we have

$$f^{\text{eq}} = A \exp(-\xi_\mu \chi^\mu). \quad (2.45)$$

The temporal components, ξ^0 and χ^0 , can be calculated by the relations

$$\xi^0 = \sqrt{|\vec{\xi}|^2 + \nu^2}, \quad (2.46)$$

$$\chi^0 = \nu \gamma(u), \quad \gamma(u) = \sqrt{1 + \frac{|\vec{\chi}|^2}{\nu^2}}. \quad (2.47)$$

In analogy to the classical procedure of expanding the Maxwell-Boltzmann distribution in Hermite polynomials, we can also expand the Maxwell-Jüttner distribution, using orthogonal polynomials of the following form:

$$f^{\text{eq}}(\vec{\xi}, \vec{x}, t) = w(\vec{\xi}) \sum_{n=0}^{\infty} \frac{a_{(n)}(\vec{x}, t)}{N_{(n)}} F_{(n)}(\vec{\xi}), \quad (2.48)$$

where

$$\int w(\vec{\xi}) F_{(n)}(\vec{\xi}) F_{(m)}(\vec{\xi}) \frac{d^3\xi}{\xi^0} = 0, \quad (2.49)$$

for $m \neq n$, and

$$N_{(n)} = \int w F_{(n)} F_{(n)} \frac{d^3\xi}{\xi^0}. \quad (2.50)$$

Therefore, we need to construct the appropriate orthogonal polynomials. Hence, we introduce the corresponding weight function as the equilibrium distribution at the local rest frame,

$$w(\vec{\xi}) = A \exp(-\nu \xi^0). \quad (2.51)$$

Using the procedure proposed by Stewart [106], where the non-equilibrium distribution was expanded around the equilibrium, and the Maxwell-Jüttner distribution as the weight function to find the orthogonal polynomials, we can take up to second order,

$$F_{(0)} = 1, \quad (2.52)$$

and

$$F_{(1)}^\alpha = \xi^\alpha - a^\alpha, \quad (2.53)$$

$$F_{(2)}^{\alpha\beta} = \xi^\alpha \xi^\beta - a_\gamma^{\alpha\beta} F_{(1)}^\gamma - b^{\alpha\beta}, \quad (2.54)$$

where a^α , $a^{\alpha\beta}$ and $b^{\alpha\beta}$ are unknowns to be calculated using the Gram-Schmidt orthogonalization procedure

$$\int w F_{(0)} F_{(1)}^\alpha \frac{d^3\xi}{\xi^0} = \int w F_{(0)} F_{(2)}^{\alpha\beta} \frac{d^3\xi}{\xi^0} = \int w F_{(1)}^\alpha F_{(2)}^{\alpha\beta} \frac{d^3\xi}{\xi^0} = 0. \quad (2.55)$$

The normalization coefficient for each polynomial is given by $\sqrt{N_{(n)}}$, and the coefficient $a_{(n)}$ is calculated using the relation

$$a_{(n)} = \int f^{\text{eq}} F_{(n)} \frac{d^3\xi}{\xi^0}. \quad (2.56)$$

To calculate the coefficients a^α , $a^{\alpha\beta}$ and $b^{\alpha\beta}$, one needs the moments of the Maxwell-Jüttner distribution, which up to second order are given by [14]

$$\int f^{\text{eq}} \frac{d^3\xi}{\xi^0} = 4\pi A K_1(\nu^2), \quad (2.57)$$

$$\int \xi^\alpha f^{\text{eq}} \frac{d^3\xi}{\xi^0} = 4\pi A K_2(\nu^2) \chi^\alpha, \quad (2.58)$$

$$\int \xi^\alpha \xi^\beta f^{\text{eq}} \frac{d^3\xi}{\xi^0} = -4\pi A (K_2(\nu^2) \eta^{\alpha\beta} - K_3(\nu^2) \chi^\alpha \chi^\beta), \quad (2.59)$$

where $K_n(\nu^2)$ is the modified Bessel function of the second kind of order n . The moments with respect to the weight function can be determined by considering the above integrals in the local Lorentz rest frame.

For the sake of simplicity we define ϕ^α as

$$(\phi^\alpha) = (\chi^0, \vec{0}), \quad (2.60)$$

and by using the orthogonalization relations to calculate the unknowns, the resulting relativistic orthogonal polynomials are given by

$$F_{(0)} = 1, \quad (2.61)$$

$$F_{(1)}^\alpha = \xi^\alpha - \frac{K_2(\nu^2)}{K_1(\nu^2)} \phi^\alpha, \quad (2.62)$$

$$F_{(2)}^{\alpha\beta} = \xi^\alpha \xi^\beta - a_\gamma^{\alpha\beta} F_{(1)}^\gamma - b^{\alpha\beta}, \quad (2.63)$$

where

$$b^{\alpha\beta} = \frac{K_3(\nu^2)}{K_1(\nu^2)} \phi^\alpha \phi^\beta - \frac{K_2(\nu^2)}{K_1(\nu^2)} \eta^{\alpha\beta}, \quad (2.64)$$

and

$$\begin{aligned} a_\gamma^{\alpha\beta} = & \frac{\eta_{\gamma\delta} + D(\nu) \phi_\gamma \phi_\delta}{2K_2(\nu^2) D(\nu)} \left[K_3(\nu^2) (\eta^{\alpha\delta} \phi^\beta + \eta^{\beta\delta} \phi^\alpha) \right. \\ & - \left(K_3(\nu^2) - \frac{[K_2(\nu^2)]^2}{K_1(\nu^2)} \right) \eta^{\alpha\beta} \phi^\delta \\ & \left. + \left(K_4(\nu^2) - \frac{K_2(\nu^2) K_3(\nu^2)}{K_1(\nu^2)} \right) \phi^\alpha \phi^\beta \phi^\delta \right]. \end{aligned} \quad (2.65)$$

Here, the function $D(\nu)$ is defined by

$$[1 + D(\nu)]^{-1} = 1 + \frac{K_2(\nu^2)}{K_1(\nu^2)} - \frac{K_3(\nu^2)}{K_2(\nu^2)}. \quad (2.66)$$

By following this procedure, we can calculate higher order polynomials. However, since here we are interested in recovering only up to the second moment of the Maxwell-Jüttner distribution (energy-momentum tensor), using the expansion up to second order is sufficient. In particular, the third, fourth, and

fifth order moments, which are needed to describe highly viscous fluids, would increase dramatically the complexity of our expansion, and consequently its numerical implementation.

Additionally, in the ultrarelativistic limit, $k_B T \gg mc^2$, i.e. $\nu \ll 1$, we can use the following asymptotic relation:

$$\lim_{\nu \rightarrow 0} K_n(\nu^2) = \frac{2^{n-1}(n-1)!}{\nu^{2n}}. \quad (2.67)$$

Using the resulting polynomials $F_{(n)}$, coefficients $a_{(n)}$ and $N_{(n)}$, with Eqs. (2.48) and (2.67), we can expand the Maxwell-Jüttner distribution in orthogonal polynomials,

$$\begin{aligned} f^{\text{eq}} \simeq A e^{-\nu \xi^0} & \left\{ 1 + \left(\frac{\chi^0 \xi^0 + 3}{2} - \frac{\chi^0}{\nu} - \frac{\xi^0 \nu}{4} \right) (\vec{\xi} \cdot \vec{\chi}) \right. \\ & + \xi^x \xi^y \chi^x \chi^y + \xi^x \xi^z \chi^x \chi^z + \xi^y \xi^z \chi^y \chi^z \\ & + \frac{4}{\nu^4 - 6\nu^2 + 15} [(\xi^x)^2 (\chi^x)^2 + (\xi^y)^2 (\chi^y)^2 + (\xi^z)^2 (\chi^z)^2 \\ & \left. + \left((1 - \nu^2) \xi^0 - \frac{4 - 2\nu^2}{\nu^2} \right) (\vec{\chi} \cdot \vec{\chi}) \right\}, \end{aligned} \quad (2.68)$$

up to second order.

One can compare the Maxwell Jüttner distribution with the zeroth, first, and second order expansions in the one dimensional case. The result of the distributions versus ξ_x for the case $\beta = 0.2$ is presented in Fig. 2.2. Here, we can observe that, as expected, as the order of the expansion increases, the expansion becomes more accurate. For illustrative purposes, in the inset of Fig. 2.2, we show in the local rest frame, the polynomials corresponding to the zeroth ($F_{(0)}$), first ($F_{(1)}^x$), and second ($F_{(2)}^{xx}$) orders.

We can write the Boltzmann equation, Eq. (2.32), as follows:

$$\xi^0 \partial_t f + \xi^a \partial_a f = -\frac{\nu}{\tau c} (f - f^{\text{eq}}), \quad (2.69)$$

where again Latin subscript a runs over the spatial coordinates. In order to discretize Eq. (2.69) and avoid a multi-time lattice, we need to consider the temporal components of the discretized velocity 4-vector, i.e. ξ_i^0 , as constant. Therefore, a transformation of the temporal component of both ξ^α and χ^α is

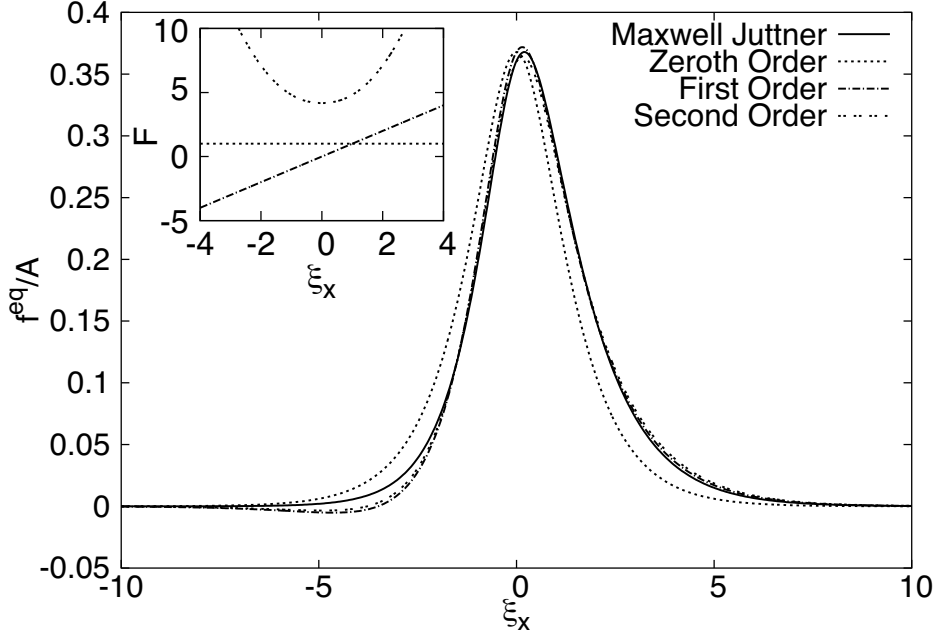


Fig. 2.2: Comparison between the Maxwell Jüttner distribution function and the zeroth, first, and second order expansions in one space dimension for $\beta = 0.2$. In the inset, $F_{(0)}$, $F_{(1)}^x$ and $F_{(2)}^{xx}$ polynomials, in the local rest frame are shown.

required. We can write $(\xi_i^\alpha) = (c_t/c_0, \vec{c}_a)$ and $(\chi^\alpha) = (\chi^0/c_0, \vec{\chi})$, where c_t , c_0 and c_a are constants related to the size of the lattice.

We will use a lattice configuration D3Q19, which can be expressed as

$$\vec{c}_a = \begin{cases} (0, 0, 0) & i = 0; \\ c_a(\pm 1, 0, 0)_{FS} & 1 \leq i \leq 6; \\ c_a(\pm 1, \pm 1, 0)_{FS} & 7 \leq i \leq 18, \end{cases} \quad (2.70)$$

where the subscript FS denotes a fully symmetric set of points (see Fig. 2.3). To find the discretized weights for the lattice, we use a quadrature procedure. According to the quadrature rule, the discretized weights should satisfy the relation

$$\int R(\vec{\xi}) w(\vec{\xi}) \frac{d^3 \xi}{\xi^0} = \sum_{i=1}^N R(\xi_i) w_i, \quad (2.71)$$

where $R(\vec{\xi})$ is an arbitrary polynomial of order $2N$ or less. Using this relation, we can construct a system of equations by replacing $R(\vec{\xi})$ with different combinations of zeroth, first, and second order polynomials. The left hand side of the above equation can be calculated by using Eqs. (2.57) to (2.59). Thus, the resulting discrete weights are given by

$$w_0 = 1 + \frac{4c_t^2\nu^2}{361c_0^2} - \frac{c_t^2}{c_a^2c_0^2}, \quad (2.72)$$

$$w_i = \frac{c_t^2}{2166c_0^2c_a^2} (361 - 8c_a^2\nu^2), \quad (2.73)$$

for $1 \leq i \leq 6$, and

$$w_i = \frac{c_t^2\nu^2}{1083c_0^2}, \quad (2.74)$$

for $7 \leq i \leq 18$. Note that we still need to calculate the constants related to the size of the lattice, i.e. c_a, c_t and c_0 .

Considering the mentioned temporal transformation, the discretized form of the equilibrium distribution function, in the ultrarelativistic limit ($\nu \ll 1$), becomes

$$\begin{aligned} f_i^{\text{eq}} = & \frac{3}{4}(\epsilon + p)\frac{c_0^2}{c_t^2}w_i \left\{ 1 + c_a^x c_a^y \chi^x \chi^y + c_a^x c_a^z \chi^x \chi^z + c_a^y c_a^z \chi^y \chi^z \right. \\ & + \left(\frac{c_t \chi^0}{2c_0^2} - \frac{\chi^0}{\nu c_0} \right) (\vec{c}_a \cdot \vec{\chi}) + \frac{4}{15} [(c_a^x)^2 (\chi^x)^2 + (c_a^y)^2 (\chi^y)^2 \\ & \left. + (c_a^z)^2 (\chi^z)^2 - \frac{4}{\nu^2} (\vec{\chi} \cdot \vec{\chi})] \right\}. \end{aligned} \quad (2.75)$$

Additionally, the discretized 4-momenta should satisfy the following relation for the energy-momentum tensor, i.e. the second order moment of the distribution function,

$$\begin{aligned} \int p^\alpha p^\beta f^{\text{eq}} \frac{d^3 p}{p^0} &= \sum_{i=1}^N p_i^\alpha p_i^\beta f_i^{\text{eq}} \\ &= (\epsilon + p) \frac{U^\alpha U^\beta}{c^2} - p \eta^{\alpha\beta} = T_{\text{eq}}^{\alpha\beta}, \end{aligned} \quad (2.76)$$

where $T_{\text{eq}}^{\alpha\beta}$ denotes the energy-momentum tensor at equilibrium and, here, N is the number of discrete velocities, which is 19 in our case. Note that higher

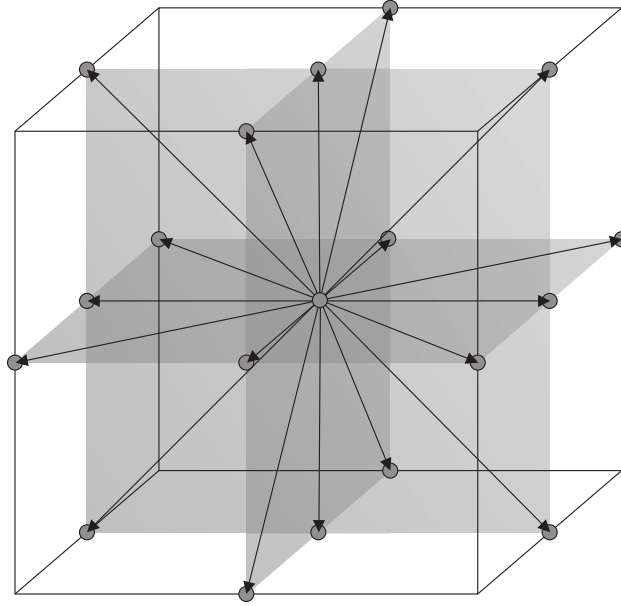


Fig. 2.3: D3Q19 lattice configuration.

order moments of the discrete equilibrium distribution can be calculated by performing the respective sums, i.e.,

$$T^{\alpha\beta\ldots\gamma} = \sum_{i=1}^N p_i^{\alpha} p_i^{\beta} \ldots p_i^{\gamma} f_i^{\text{eq}}. \quad (2.77)$$

However, they would not correspond to the ones of the Maxwell-Jüttner distribution, because the latter require an expansion in higher order polynomials. Their contribution to the dynamics of the fluid become important at high values of viscosity, and since they are not exactly recovered, our model does not work properly in that regime. Fortunately, many applications in astrophysics and high energy physics deal with nearly-inviscid or weakly viscous fluids.

We can simply find the constants related to the lattice size, using the fact that in the tensor, the coefficient of $U^{\alpha}U^{\beta}$ for different α and β should be always the same. The calculated values for the constants are

$$c_a = \frac{\sqrt{19}}{\nu}, \quad c_t/c_0 = \frac{\sqrt{27}}{\nu}, \quad c_0 = \frac{3}{8}(9 - 2\sqrt{3}). \quad (2.78)$$

Considering the natural units $c = k_B = 1$, from the energy-momentum tensor, one can obtain the following relations:

$$\epsilon + p = \frac{4n}{\nu^2}, \quad p = \frac{n}{\nu^2}, \quad \epsilon = 3p, \quad (2.79)$$

finding that the relation between ϵ and p corresponds to the well-known equation of state in the ultrarelativistic limit.

Note that due to the fact that we have supposed ξ_i^0 to be constant, to avoid a multi-time evolution lattice, there are some equations in the quadrature procedure for the first order moment and the second order moment of the distribution function which could not be satisfied simultaneously. Indeed, we can choose whether to recover the first order moment or the second order moment in the quadrature. To satisfy the first moment of the Maxwell-Jüttner distribution function leads to recover the equation for the conservation of number of particles, $\partial_\alpha N^\alpha = 0$, and the second order moment, the equation for the conservation of momentum-energy, $\partial_\alpha T^{\alpha\beta} = 0$. To calculate the four unknowns, namely U^x, U^y, U^z and ϵ , knowing the values of the components of energy-momentum tensor and the equation of state $\epsilon = 3p$ would be enough, as will be discussed later. Therefore, by using the ultrarelativistic equation of state the dynamics of the system is not affected by the number of particles and the equation for the conservation of momentum-energy is therefore sufficient to describe the entire dynamics of the relativistic fluid. For this reason, our quadrature is targeted to recover the second order moment, using a separate distribution function to recover the equation for the conservation of number of particles, $\partial_\alpha N^\alpha = 0$, based on the model proposed by Hupp et al. [50] as we will discuss shortly.

Using the mentioned lattice to discretize the Boltzmann equation, Eq. (2.69) can be written as follows:

$$f_i(\vec{x} + \vec{c}_a \frac{c_0}{c_t} \delta t, t + \delta t) - f_i(\vec{x}, t) = -\frac{c_0 \nu \delta t}{\tau c_t} (f_i - f_i^{\text{eq}}). \quad (2.80)$$

The left hand side of the equation is readily recognized as free-streaming, while the right hand side is the discrete version of the collision operator according to the model of Marle. In this equation, the following relation

between δt and δx has been used:

$$\delta t = \frac{c_t \delta x}{c_a c_0}. \quad (2.81)$$

In the ultrarelativistic limit, the shear viscosity using the model of Marle can be calculated as:

$$\eta = \frac{(\epsilon + p)}{\nu^2} \left(\tau - \frac{1}{2} \right). \quad (2.82)$$

As explained, in our model, this expression is only valid for small values of τ (which leads to small values of the Knudsen number), where higher order moments of the distribution can be neglected.

At each time step and at each lattice point, the values of the macroscopic velocity and energy density can be evaluated using the calculated energy-momentum tensor as follows

$$\sum_{i=1}^N p_i^\alpha p_i^\beta f_i = (\epsilon + p) \frac{U^\alpha U^\beta}{c^2} - p \eta^{\alpha\beta}. \quad (2.83)$$

Thus, a system of four equations, corresponding to the T^{00} , T^{0x} , T^{0y} and T^{0z} , using the equation of state $\epsilon = 3p$, can be solved to calculate the macroscopic parameters.

2.4.2 Extended model for high velocities

At high velocities ($\beta \gtrsim 0.6$), due to the high compressibility effects (high Mach numbers), the described numerical scheme shows artificial discontinuities in the velocity and pressure profiles, leading to numerical instabilities in the long-term evolution [76]. We shall return to this issue in Sec. 2.5. The relativistic Mach number can be expressed as $Ma_r = \gamma(u)|\vec{u}|/\gamma(c_{so})c_{so}$ where c_{so} is the velocity of sound, which is $c_{so} = c/\sqrt{3}$ in the ultrarelativistic regime. In order to overcome this problem, we first use a modified version of the D3Q19 cell configuration, which is denoted by $(\xi_i^\alpha) = (c_t/c_0, \vec{c}_a)$, where \vec{c}_a takes now the following form:

$$\vec{c}_a = \begin{cases} (0, 0, 0) & i = 0; \\ c_a(\pm 1, 0, 0)_{FS} & 1 \leq i \leq 6; \\ 2c_a(\pm 1, \pm 1, 0)_{FS} & 7 \leq i \leq 18. \end{cases} \quad (2.84)$$

Since some of the discrete velocities go beyond the first and second neighbors in the lattice, the scheme can support higher flow speeds. In order to find the discretized weights, as well as the size of the lattice cells, we repeat the same procedure as before obtaining

$$w_0 = 1 + \frac{7c_t^2\nu^2}{676c_0^2} - \frac{c_t^2}{c_a^2c_0^2}, \quad (2.85)$$

$$w_i = \frac{c_t^2}{1014c_0^2c_a^2} (169 - 2c_a^2\nu^2), \quad (2.86)$$

for $1 \leq i \leq 6$,

$$w_i = \frac{c_t^2\nu^2}{8112c_0^2}, \quad (2.87)$$

for $7 \leq i \leq 18$, and

$$c_a = \frac{\sqrt{13}}{\nu}, \quad c_t/c_0 = \frac{\sqrt{27}}{\nu}, \quad c_0 = \frac{3}{8}(9 - 2\sqrt{3}). \quad (2.88)$$

The second step to extend our model, is to introduce the minimum modulus (min mod) scheme to discretize the spatial components in the streaming term in the Boltzmann equation, Eq. (2.69), i.e. $p_i^a \partial_a f_i$. The min mod scheme is a flux limiter method that efficiently reduces the instability especially when step discontinuities occur (e.g. in shock waves). The following relations characterize this scheme [92]:

$$\partial_a(p_i^a f_i) = \frac{1}{|\delta x \vec{e}_a|} [h_i^a(\vec{x} + \delta x \vec{e}_a) - h_i^a(\vec{x})], \quad (2.89)$$

$$h_i^a(\vec{x}) = f_i^{aL}(\vec{x}) + f_i^{aR}(\vec{x}), \quad (2.90)$$

$$f_i^{aL}(\vec{x}) = f_i^{a+}(\vec{x}) + \frac{1}{2} \min \text{ mod} \left(\Delta f_i^{a+}(\vec{x}), \Delta f_i^{a+}(\vec{x} - \delta x \vec{e}_a) \right), \quad (2.91)$$

$$f_i^{aR}(\vec{x}) = f_i^{a-}(\vec{x} + \delta x \vec{e}_a) - \frac{1}{2} \min \text{ mod} \left(\Delta f_i^{a-}(\vec{x}), \Delta f_i^{a-}(\vec{x} + \delta x \vec{e}_a) \right), \quad (2.92)$$

$$f_i^{a+} = \frac{1}{2}(p_i^a + |p_i^a|)f_i, \quad f_i^{a-} = \frac{1}{2}(p_i^a - |p_i^a|)f_i, \quad (2.93)$$

$$\Delta f_i^{a\pm}(\vec{x}) = f_i^{a\pm}(\vec{x} + \delta x \vec{e}_a) - f_i^{a\pm}(\vec{x}), \quad (2.94)$$

where \vec{e}_a is a unit vector in the direction of the corresponding spatial coordinate. Let us remind that p_i^a is independent of spatial coordinates. The min mod function is defined as

$$\min \text{mod}(X, Y) = \frac{1}{2} \min(|X|, |Y|) \times [\text{Sign}(X) + \text{Sign}(Y)]. \quad (2.95)$$

Note that in non-relativistic flows, the bulk viscosity plays an important role in highly compressible flows and enhances the stability of numerical simulations of fluids at very high velocities, including shock waves [24]. However, in the ultrarelativistic limit, the energy-momentum tensor is traceless and the bulk viscosity is zero [99, 77]. Therefore, in order to include the bulk viscosity, we add the following term to the right hand side of the Boltzmann equation, Eq. (2.69):

$$\lambda_i \sum_{a=x,y,z} \partial_a^2 f_i, \quad (2.96)$$

where

$$\lambda_i = \begin{cases} 0 & i = 0; \\ \alpha \delta x & i \neq 0, \end{cases} \quad (2.97)$$

where α is a constant. A central finite difference scheme is used to calculate the second order derivative. Chapman-Enskog analysis reveals that the bulk viscosity obtained by this extra-term takes the form

$$\eta_b = \frac{4p\alpha\nu^6}{27}. \quad (2.98)$$

Note that, like the analytical expression of the bulk viscosity for the model of Marle, the above-mentioned bulk viscosity is also proportional to T^{-3} , and as expected goes to zero in the ultrarelativistic limit $\nu \rightarrow 0$. However, this small value of bulk viscosity is sufficient to stabilize the system at high velocities, as we are going to show in the next section.

Once all of the extensions above are taken into account, the discretized form of the relativistic Boltzmann equation takes the following expression:

$$\begin{aligned} f_i(\vec{x}, t + \delta t) - f_i(\vec{x}, t) + \frac{c_0}{c_t} \frac{\delta t}{\delta x} [h_i^a(\vec{x} + \delta x \vec{e}_a) - h_i^a(\vec{x})] = \\ - \frac{c_0 \nu \delta t}{\tau c_t} [f_i(\vec{x}, t + \delta t) - (2f_i^{\text{eq}}(\vec{x}, t) \\ - f_i^{\text{eq}}(\vec{x}, t - \delta t))] + \frac{c_0 \nu \delta t}{c_t} \lambda_i \sum \partial_a^2 f_i(\vec{x}, t), \end{aligned} \quad (2.99)$$

where an implicit representation of the collision term is used, as proposed in Ref. [72] to enhance the stability of the collision term.

As mentioned above, for the cases where the dynamics of the number of particles density is also needed, one has to solve the conservation equation, i.e. $\partial_\alpha N^\alpha = 0$, with $N^\alpha = nU^\alpha$. For this purpose, we add an extra distribution function, g_i , based on the model proposed by Hupp et al. [50], which follows the dynamics of the Boltzmann equation given by Eq. (2.99), without the λ_i coefficient term. The corresponding modified equilibrium distribution function is given by:

$$g_i^{\text{eq}} = w'_i n \gamma(u) \left(\frac{c_0}{c_t} + 3(\vec{c}_a \cdot \vec{u}) + \frac{9}{2}(\vec{c}_a \cdot \vec{u})^2 - \frac{3}{2}|\vec{u}|^2 \right), \quad (2.100)$$

$$w'_0 = \frac{1}{10}, \quad w'_i = \frac{6}{35} - \frac{1}{42c_a^2}, \quad (2.101)$$

for $1 \leq i \leq 6$,

$$w'_i = \frac{1}{84c_a^2} - \frac{3}{280} \quad (2.102)$$

for $7 \leq i \leq 18$, where we have used our new cell configuration, and w'_i are the respective discrete weights. Knowing the velocity from the second order moment relation, the value of the number density in the model can be calculated using the relation for the first moment, which is

$$\sum_{i=1}^N p_i^\alpha g_i = nU^\alpha. \quad (2.103)$$

Having discussed the model, we move on to the next section, where different validations and results for the Riemann problem are provided, along with a simulation of a shock wave colliding with an interstellar cloud.

2.5 Validation and results

In order to validate the model and the numerical procedure, we present results for the simulation of relativistic shock wave propagation in viscous quark-gluon plasma. The associated Riemann problem is studied and several comparisons are drawn between the present relativistic LB model and the

existing literature. Indeed, the Riemann problem is a challenging test for numerical methods, since it involves a shock and rarefaction waves.

The initial condition of the Riemann problem consists of two regions with different pressure, which are separated by a membrane in the middle of the interval. The pressure in the left region (p_0) is higher than the pressure in the right region (p_1). Both sides of the discontinuity are supposed to be initially in the rest frame. Hence, spatial components of the initial velocities for both sides are set to zero. At time $t = 0$, the membrane is removed and a shock wave propagates from the high pressure region into the low pressure region with velocity v_{shock} and a rarefaction wave propagates in the opposite direction. The shock velocity depends on the pressure difference, the equation of state, and can be calculated analytically [98, 117]. The region between the shock wave and the rarefaction wave has a constant pressure, corresponding to the so-called shock plateau. In this region the velocity is also constant (v_{plat}).

In order to compare our results with existing models, we use the same conditions as in Ref. [10, 74]. Therefore, one dimensional simulations are carried out using $800 \times 1 \times 1$ cells, where open boundary conditions are considered at the two ends by copying the distribution vectors from the neighbour cells. The cell size δx is taken to be unity, which corresponds to $\delta x = 0.008 fm$ in IS units and δt can be calculated from Eq. (2.81). We use η/s as the characteristic parameter of shear viscosity, where the viscosity is defined in Eq. (2.82) and the entropy density is given by $s = 4n - n \ln \lambda$, with $\lambda = n/n^{eq}$ being the fugacity of gluons, $n^{eq} = d_G T^3/\pi^2$ the equilibrium density, and $d_G = 16$ the degeneracy of gluon.

First we compare the existing numerical results with the non-extended model (hereafter basic model). For the first validation test, we set the initial pressure at the left and right sides to $p_0 = 5.43 GeV/fm^3$ and $p_1 = 2.22 GeV/fm^3$, respectively. This corresponds to 2.495×10^{-7} and 1.023×10^{-7} in numerical units, respectively. Fig. 2.4 shows the pressure profiles at time $t = 3.2 fm/c$ for different values of η/s , compared to the results reported by Ref. [10] (hereafter BAMPS) and an analytical solution for the inviscid case reported in Ref. [98]. As one can notice, very satisfactory agreement for different

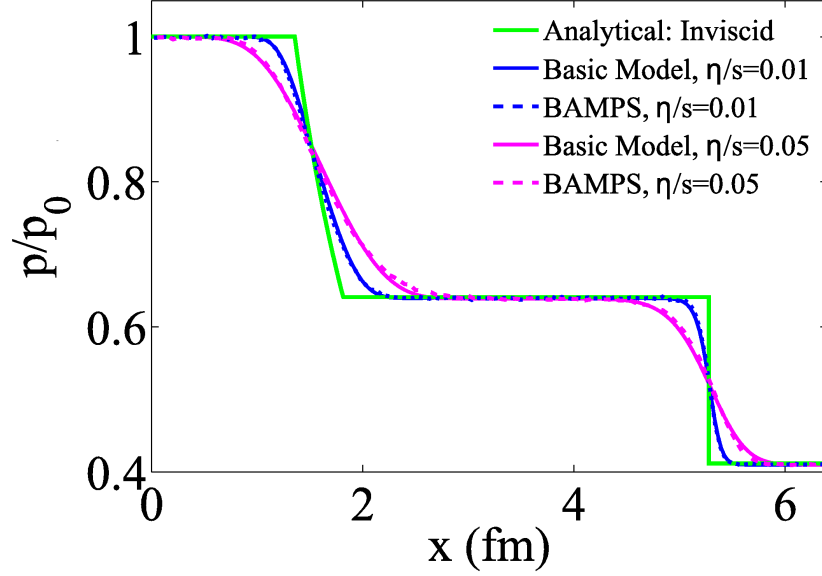


Fig. 2.4: Comparison between the velocity profile of the basic model and BAMPS, for different values of η/s at weakly relativistic regime.

values of η/s is obtained.

As mentioned previously, the lattice Boltzmann method is computationally very efficient. For instance, the above simulation took ~ 220 ms on a single core of an Intel CPU with 2.40 GHz clock speed, which is approximately an order of magnitude faster than corresponding hydrodynamic simulations. This corresponds to 1.4 Msup/s (million site update per second). To further elaborate on the validity of our model, we compare with the results of Ref. [74] (hereafter previous LBS) for different values of η/s . Fig. 2.5 shows that pressure and velocity profiles are in good agreement with previous LBS simulations. It is worth mentioning that, as it is apparent from Fig. 2.5, the above mentioned pressure difference corresponds to $\beta = |v_{plat}| \sim 0.2$ (weakly relativistic regime), while the velocity of the shock is $v_{shock} \sim 0.65$.

To study higher velocities, we consider higher pressure difference between the left side and the right side, namely $p_0 = 5.43 \text{ GeV}/\text{fm}^3$ and $p_1 = 0.339 \text{ GeV}/\text{fm}^3$. This corresponds to 2.495×10^{-7} and 1.557×10^{-8} in numerical units, respectively. The resulting pressure and velocity profiles for

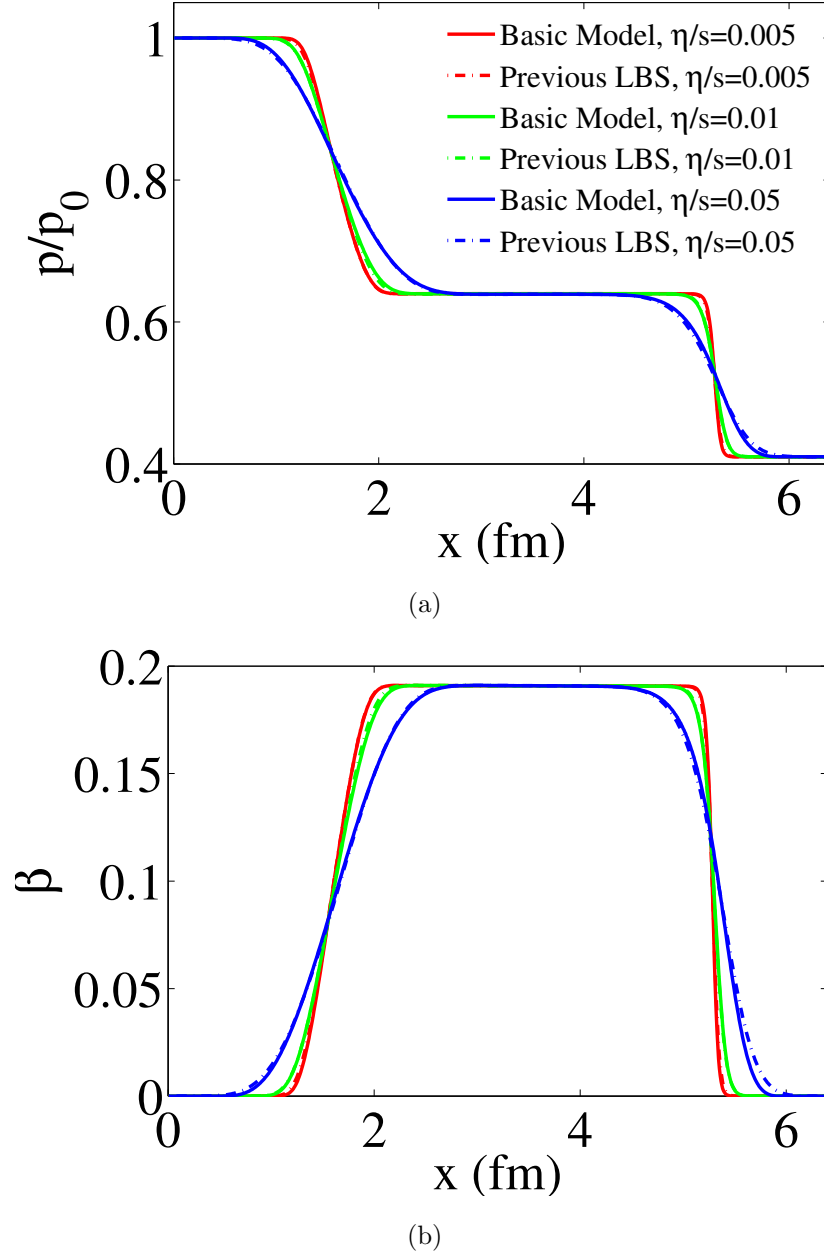
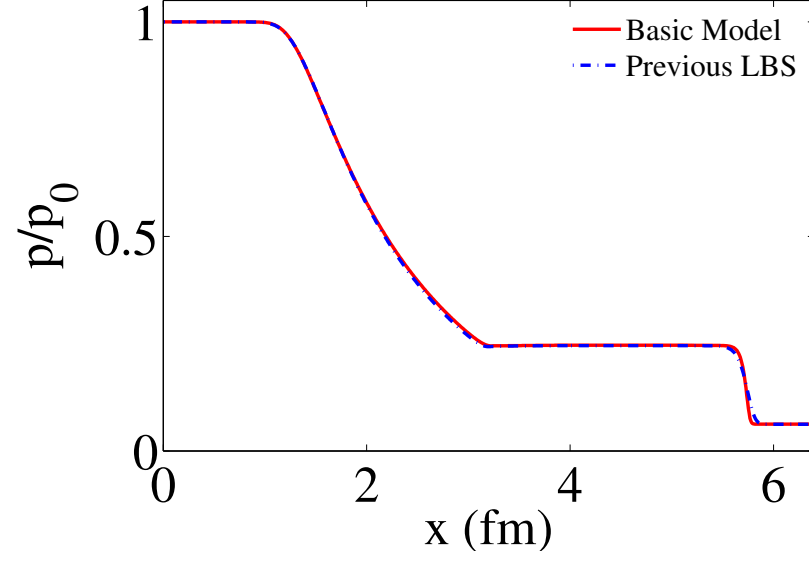
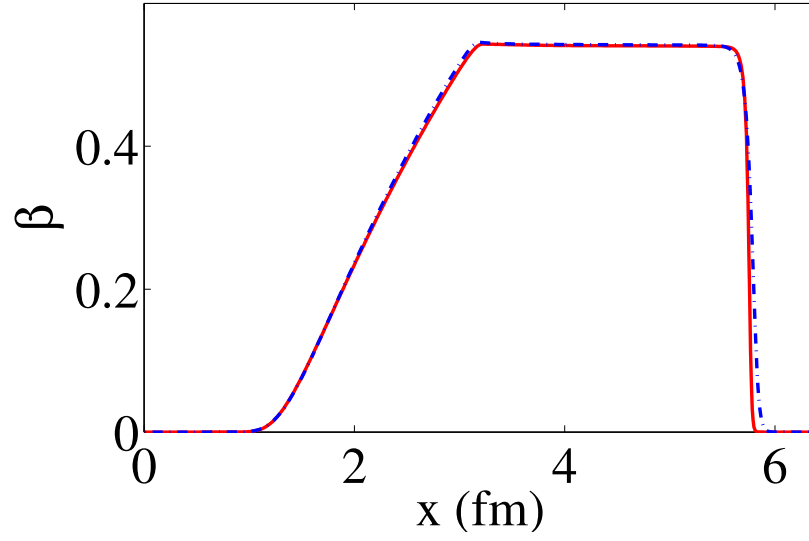


Fig. 2.5: Comparison between the basic model and the previous LBS model at different η/s , for (a) the pressure and (b) velocity profiles in the weakly relativistic regime.

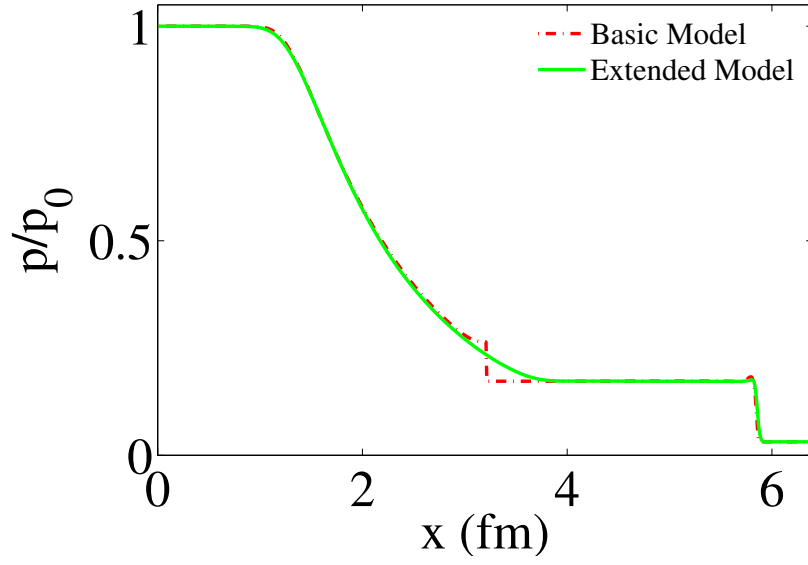


(a)

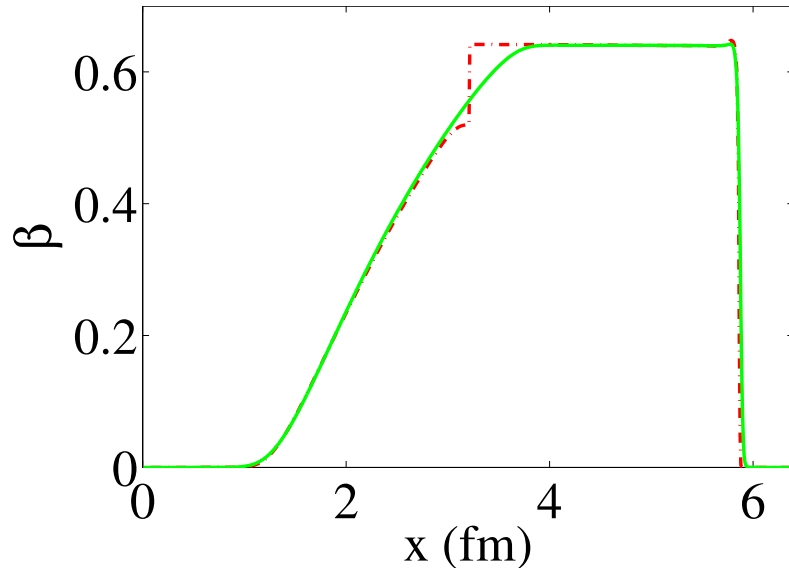


(b)

Fig. 2.6: Comparison between the basic model and the previous LBS model at $\eta/s = 0.01$, for (a) the pressure and (b) velocity profiles in the moderately relativistic regime.



(a)



(b)

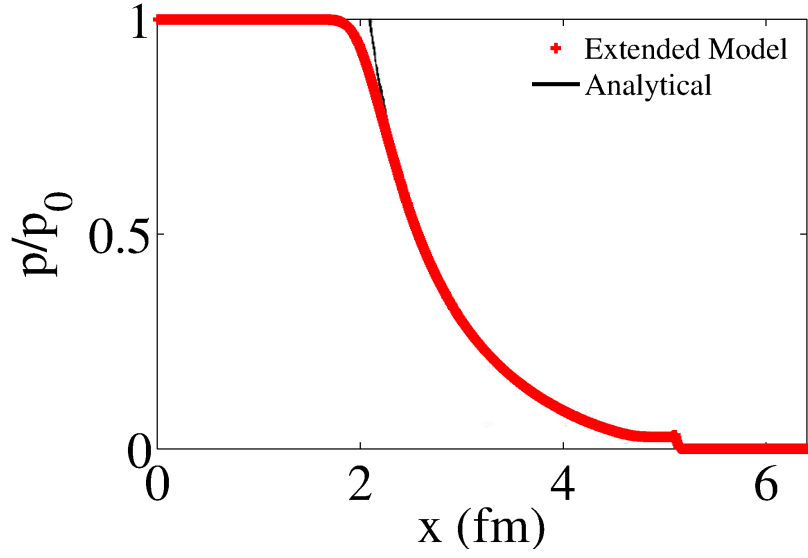
Fig. 2.7: Comparison between the basic and extended models for (a) the pressure and (b) velocity profiles in the moderately relativistic regime.

$\eta/s = 0.01$, are compared to the results with previous LBS in Fig. 2.6, showing again very good agreement. It should be noted that, due to the above-mentioned pressure difference, the matter behind the shock moves with the velocity $\beta \sim 0.6$ (moderately relativistic regime), while the shock itself goes with the velocity $v_{shock} \sim 0.92$.

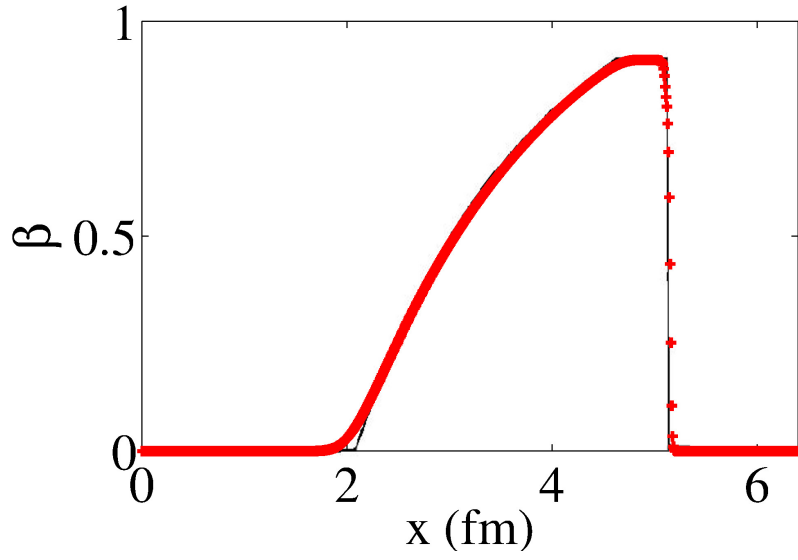
Note that the proposed model in the non-extended form (basic model) becomes numerically unstable for higher velocities ($\beta \gtrsim 0.6$). In order to overcome this problem, we use our extended model, which enhances the stability of the numerical procedure without any appreciable loss of computational efficiency. To further investigate this issue, we carry out two simulations with the same conditions for relatively higher velocity, one using the basic model, and the other one using the extended one. The pressure is set to be $p_0 = 5.43 \text{ GeV}/\text{fm}^3$ and $p_1 = 0.1695 \text{ GeV}/\text{fm}^3$ for the left side and the right side, respectively, which corresponds to 2.495×10^{-7} and 7.785×10^{-9} in numerical units. Here, $\eta/s = 0.01$, $\delta t/\delta x = 0.25$, and $\alpha = 0.15$ for the extended model.

The results for the pressure and velocity profiles are shown in Fig. 2.7 at time $t = 3.2 \text{ fm}/c$. Note that the applied pressure difference corresponds to $\beta \sim 0.7$. Using the basic model, an artificial discontinuity is observed in both the pressure and velocity profiles, and for higher velocities the numerical scheme becomes numerically unstable. However, the extended model proves capable of handling the simulation, the problem of the artificial discontinuity being solved completely. Additionally, apart from the region affected by the discontinuity, the good agreement between the results of two models can be interpreted as a validation for the precision of the extended model. For the extended model, with the same level of optimization as before, we can achieve 1.2 Msup/s for a single core CPU.

To the best of our knowledge, to date, there was no reported simulation of shock wave in viscous flow for $\beta \gtrsim 0.6$. However, for the inviscid case, which corresponds to the Euler equation at macroscopic scale, there exists an analytical solution for the Riemann problem. Therefore, in order to validate our extended model, we compare our results with the analytical solution of the inviscid case in Ref. [117]. Hence, we need to solve the Euler equation by ig-

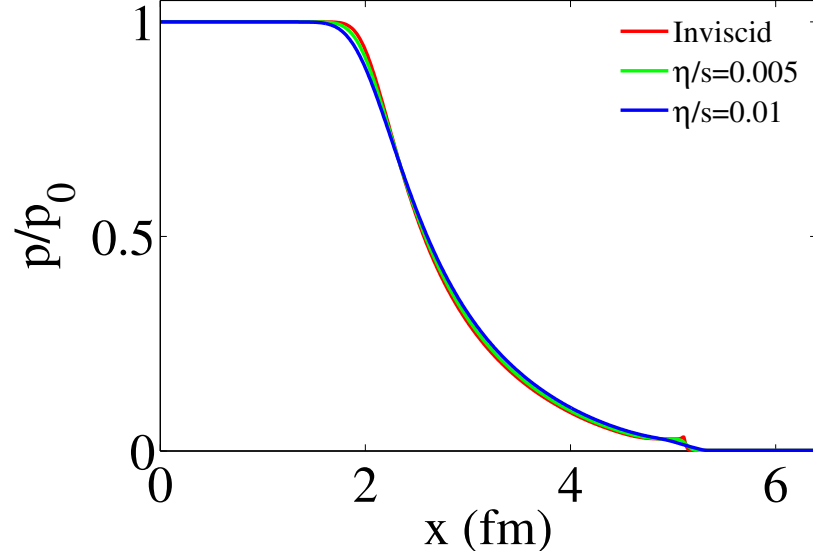


(a)

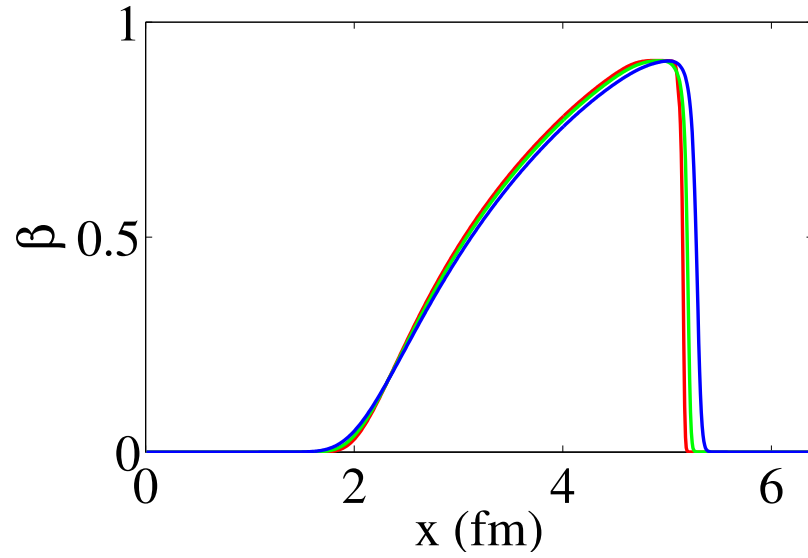


(b)

Fig. 2.8: Comparison between the extended model and analytical results for (a) the pressure and (b) velocity profiles in the highly relativistic regime.

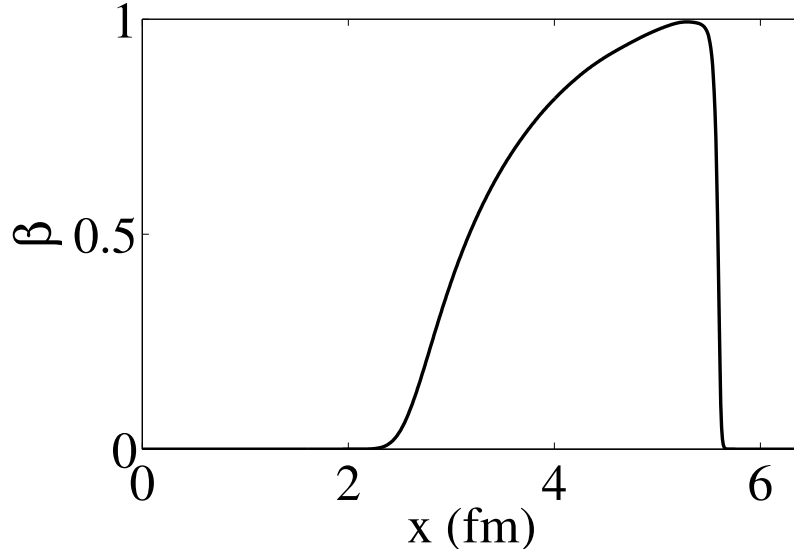


(a)

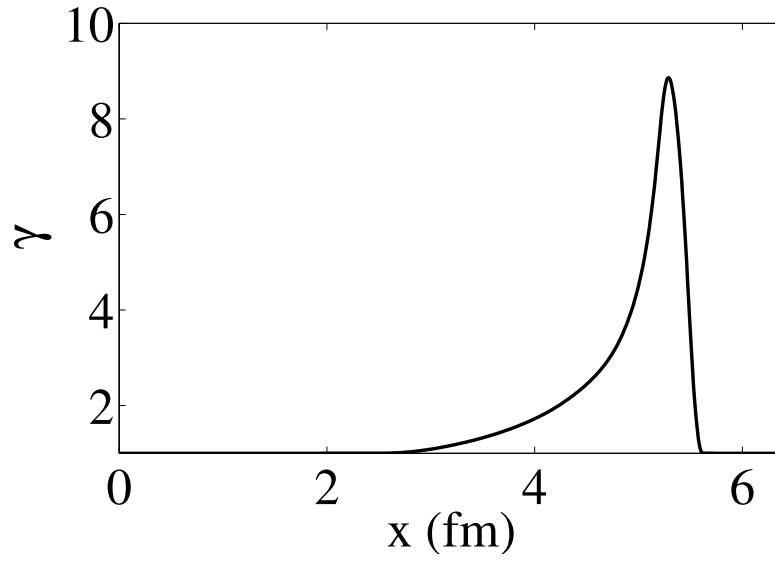


(b)

Fig. 2.9: Comparison of the results for the nearly-inviscid case and different η/s , for (a) the pressure and (b) velocity profiles in the highly relativistic regime.



(a)



(b)

Fig. 2.10: Results of the simulation for (a) the velocity profile and (b) Lorentz's factor in the ultra-high relativistic regime.

noring the viscous effects. It is worth mentioning that, in the classical lattice Boltzmann method, the numerical solution becomes unstable as one tries to set the shear viscosity to zero ($\tau = 1/2$). This is also the case for our basic model. However, in the extended model we can solve the Euler equation by changing the collision step, such that instead of implementing the regular collision, we simply set the discretized distribution functions to their corresponding equilibrium values. This is similar to the procedure used in Ref. [86] to solve the Euler equation in the non-relativistic case. As one can notice from the Boltzmann equation, this corresponds to ignore the non-equilibrium part of the distribution function which contains the information about the dissipation. Therefore, we can reasonably neglect the viscous effects in the macroscopic equations.

The results of our nearly-inviscid simulation are compared to the analytical results in Fig. 2.8. To drive the shock at velocity $\beta \sim 0.9$ (highly relativistic regime), the applied pressure is set to $p_0 = 5.43 \text{ GeV}/\text{fm}^3$ and $p_1 = 5.43 \text{ MeV}/\text{fm}^3$, which corresponds to 2.495×10^{-7} and 2.495×10^{-10} in numerical units, respectively. The results are shown at $t = 2.0 \text{ fm}/c$ and very good agreement is found. The small discrepancies between our simulation and the analytical curve are related to the fact that a small value of dissipation due to the bulk viscosity inevitably remains in our simulation, which is needed to increase the stability of the model.

The fact that we can model properly the nearly-inviscid flows at very high velocities opens the possibility of using our model in astrophysical applications, where velocities are usually high and viscous effects are negligible. Fig. 2.9 shows the same result at $\beta \sim 0.9$ for different viscosities, compared to the nearly-inviscid case at $t = 2.0 \text{ fm}/c$. The same conditions as mentioned above are considered again. The effects of increasing η/s at this velocity are similar to the cases of lower velocities.

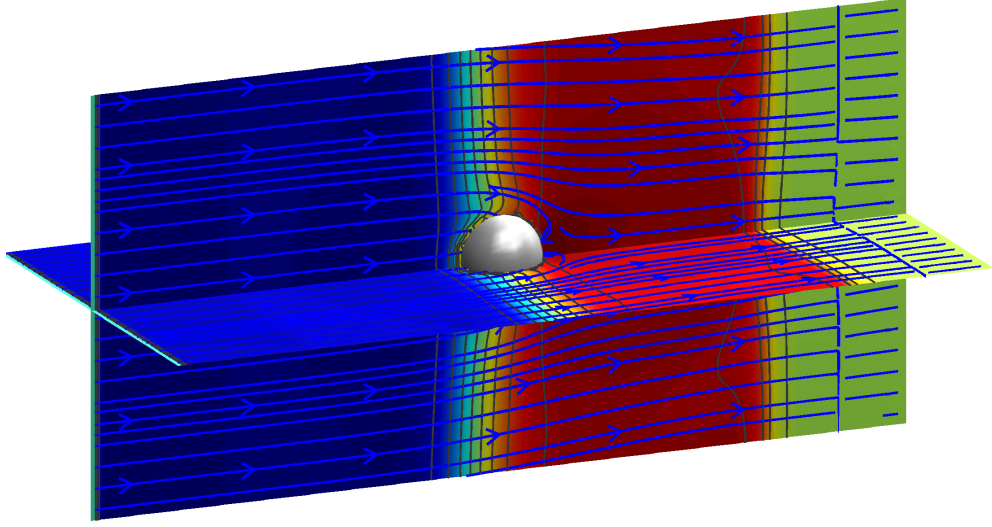
In order to demonstrate the ability of the model to simulate ultra-high velocities, we consider the case where the initial pressures $p_0 = 5.43 \text{ GeV}/\text{fm}^3$ and $p_1 = 0.0543 \text{ MeV}/\text{fm}^3$ are considered, which corresponds to 2.495×10^{-7} and 2.495×10^{-12} in numerical units, respectively. We set $\delta t/\delta x = 0.25$, $\alpha = 0.2$, and $\eta/s = 0.01$. The results for the velocity profile and local Lorentz's factor

at $t = 2.0fm/c$ are presented in Fig. 2.10, which shows that for this case $\beta \sim 0.99$ and $\gamma(u) \sim 9$. This indicates that our model is numerically stable for simulating relativistic fluids with ultra-high velocities.

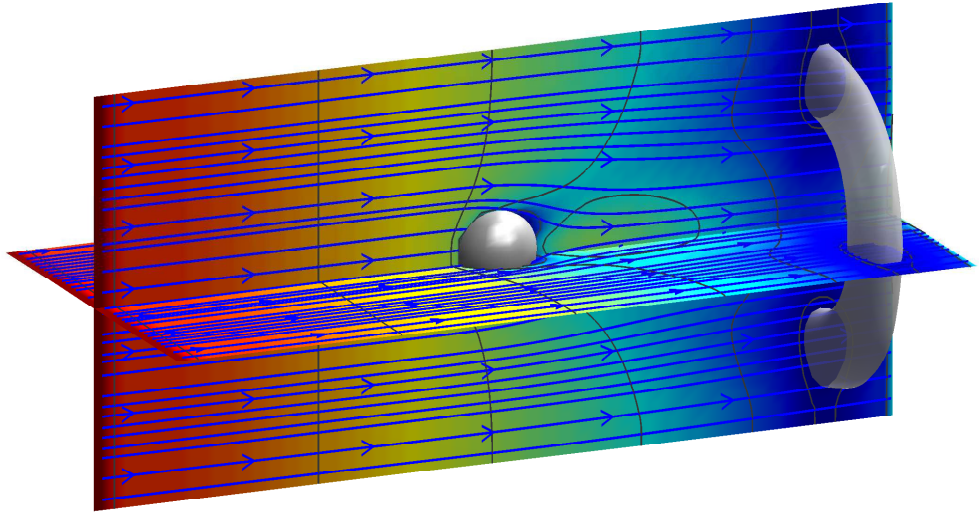
2.5.1 Astrophysical application

As an astrophysical example, we simulate a relativistic shock wave, generated by, say, a supernova explosion, colliding with a massive interstellar cloud, e.g. molecular gas [70]. The ejecta from the explosion of such supernovae are known to sweep the interstellar material up to relativistic velocities along the way (relativistic outflows) [69]. We perform a three-dimensional simulation of a shock wave passing through a cold spherical cloud in a lattice of $200 \times 100 \times 100$ cells. As mentioned earlier, in order to solve the equation of conservation of particle density, an extra distribution function is used, Eq. (2.100). As initial condition, the region is divided in two zones by the plane $x = 65$; at the right hand side ($x > 65$), the density is set to $n_1 = 0.6cm^{-3}$ and the temperature to $T_1 = 10^4K$ (with $\delta x = \delta y = \delta z = 3 \times 10^{14}$ Km). The massive cloud is modelled as a sphere with radius of 10 cells and centered at the location $(100, 50, 50)$, where we neglect the drag force acting on the cloud due to the flow (the sphere will remain at the same position during the whole simulation). Open boundary conditions are applied to all the external boundaries, except the left one, where an inlet boundary condition is applied by fixing the distribution function with the equilibrium distribution calculated at the initial condition. For the boundary condition of the cloud, on its surface, the cells evolve to the equilibrium distribution function evaluated at the constant values of $n = n_1$, $T = T_1$ and $\vec{u} = 0$. It should be mentioned that, at each cell, the pressure can be calculated using the relation $p = nT$.

By changing the initial condition at the left hand side of the dividing plane ($x \leq 65$), we are able to tune the velocity of the shock wave. Two different velocities are considered here. For the first case, we consider a shock wave at weakly relativistic regime ($\beta = 0.2$), setting $T_0 = 2.71T_1$ and $n_0 = 0.9n_1$. For the second case, highly relativistic regime ($\beta = 0.9$), these values are



(a)



(b)

Fig. 2.11: Snapshots of the three-dimensional simulation of a relativistic shock wave colliding with a massive interstellar cloud. Here, the density field is plotted in logarithmic color level in (a) the weakly relativistic regime and (b) highly relativistic regime at time $t = 1000$. Streamlines represent the velocity field and the iso-surface in (b) illustrates a region of low density ($\log(n/n_0) \sim -2.5$).

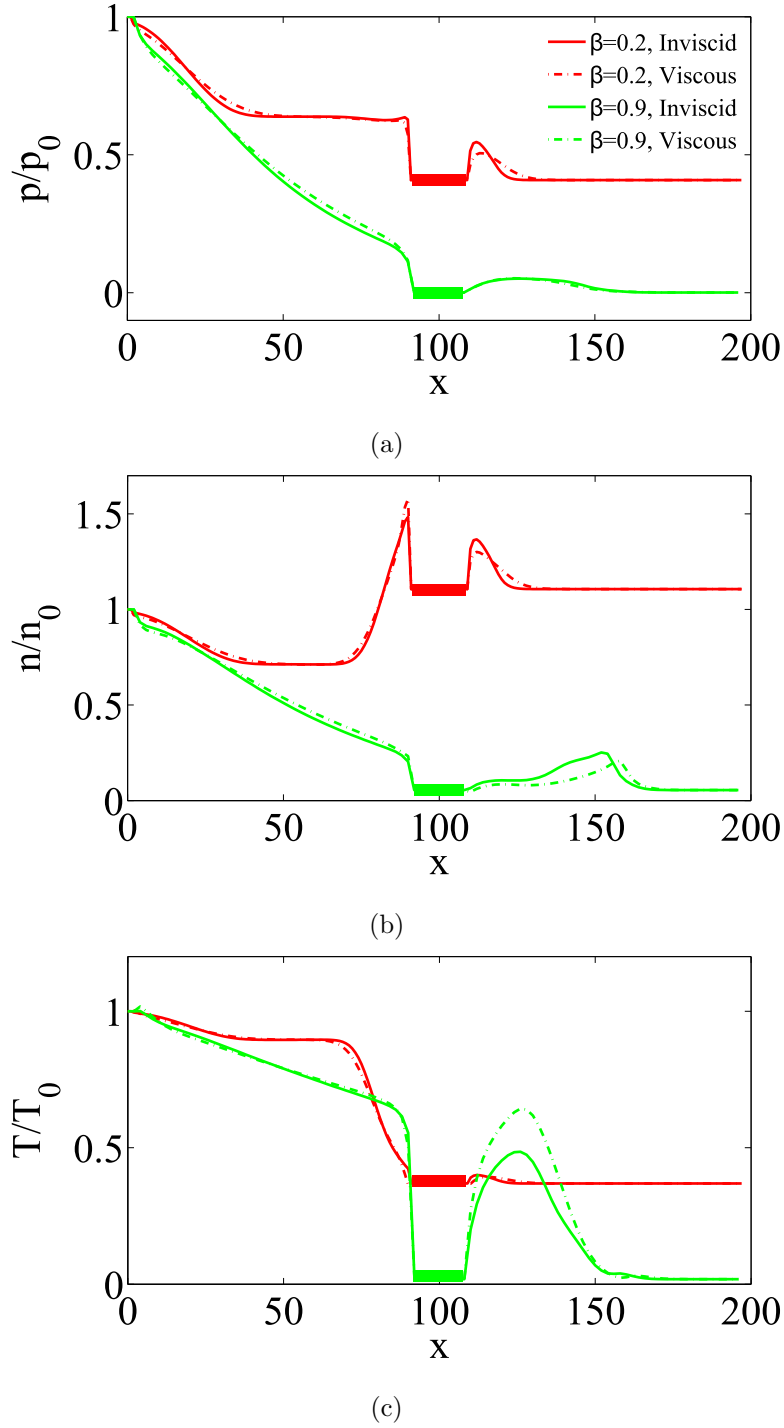


Fig. 2.12: (a) Pressure, (b) density and (c) temperature profiles in the weakly and highly relativistic regimes, for the nearly-inviscid and viscous cases. The results are shown along the x axis at $y = z = 50$ at $t = 600$ time steps. The thicker lines denote the regions where the interstellar cloud is located.

$T_0 = 54.77T_1$ and $n_0 = 10.95n_1$. Fig. 2.11 shows the results of the 3D simulation of the shock wave, after colliding with the massive interstellar cloud for the density field for both cases. The simulations are performed in the nearly-inviscid case, where $\alpha = 0.2$ and $\delta t/\delta x = 0.15$. The density field is plotted in logarithmic scale at $t = 1000$ time step, where red and blue denote high and low values, respectively, and streamlines represent the velocity field. In this figure, for the case of low velocity, we observe an increase in the density in the shock front, due to the compression. For the case of high velocity, the shock wave has already passed the domain at the considered time, and one can see that a ring-shape region of low density is generated downstream of the collision (see isosurface in Fig. 2.11).

In order to study the viscous effects, the same simulations are performed by introducing the dissipation and taking $\tau = 1$. Fig. 2.12 shows the pressure, density and temperature profiles at weakly and highly relativistic regimes for both, nearly-inviscid and viscous cases. The results are shown along the x axis at $y = z = 50$ and at $t = 600$ time steps. Note that since p_0 , n_0 , and T_0 take very different values for the weakly and highly relativistic regimes, in order to make a clear comparison of the results, we have normalized p , n , and T with p_0 , n_0 , and T_0 , respectively. As it can be appreciated, the viscous effects become relatively more important downstream of the cloud. Furthermore, it causes a pressure drop and decreases the density, while inducing a corresponding increment of temperature in the gas. Note, that the effects on the temperature are more significant at highly relativistic regime than the pressure drop, while an opposite behavior is found at weakly relativistic regime.

2.6 Summary

In this chapter, we have introduced a relativistic lattice Boltzmann model that is able to handle relativistic fluid dynamics at very high velocities. For this purpose, we have first expanded the Maxwell Jüttner distribution in orthogonal polynomials, by assuming as weight function the equilibrium dis-

tribution at the local rest frame. A discretization procedure has been applied in order to adjust the expansion to the D3Q19 cell configuration, which, in order to avoid a multi-time evolution of the Boltzmann equation, leads to the problem of recovering only the conservation of the momentum-energy tensor. However, in the ultrarelativistic regime ($\epsilon = 3p$) the entire dynamics of the system is governed by this equation and the first order moment is not required. To extend the model to high velocities ($\beta \sim 1$), we have used a flux limiter scheme and introduce a bulk viscosity term into the Boltzmann equation, to increase the numerical stability in presence of discontinuities. In order to validate our model, we have compared the numerical results for shock waves in viscous quark-gluon plasmas with the results of other existing models, and found very good agreement. In addition, to the best of our knowledge, we have for the first time successfully simulated shock waves in relativistic viscous flow for $\beta > 0.6$. We have also suggested a way to simulate nearly-inviscid flows (Euler equation) using the extended model by modifying the collision step. For this case, we have compared the results with the analytical solution, finding again very satisfactory agreement. This offers a promising strategy to study astrophysical flows at very high speeds and negligible viscous effects. Additionally, we have shown that our model is capable of simulating the Riemann problem at ultra-high relativistic flows ($\gamma \sim 10$). Finally, we have studied the collision of a shock wave colliding with a massive interstellar cloud in weakly and highly relativistic regimes, for both inviscid and viscous cases.

Chapter 3

Relativistic Richtmyer-Meshkov Instability

After discussing the relativistic lattice Boltzmann model, as an application for the numerical model, we study the relativistic effects on the Richtmyer-Meshkov (RM) instability (see Ch. 1). The chapter is organised as follows: in Sec. 3.1, the required extensions of the relativistic lattice Boltzmann model to handle the ideal gas equation of state is explained; in Sec. 3.2, the numerical results along with the linear stability analysis for the relativistic RM instability are presented and discussed in detail; in Sec. 3.3, the cooling effect of the RM instability, in particular when it is resulted from the interaction of two Mach cones in a relativistic fluid, is studied; and finally in Sec. 3.4, as a conclusion, an overall discussion of the chapter is provided.

3.1 Extensions to the relativistic lattice Boltzmann

To perform the numerical study of the RM instability, we use the relativistic LB method which is described in Ch. 2. As mentioned, this model is proposed for the equation of state in the ultrarelativistic limit, i.e., $\epsilon = 3p$. However, for this case, the equation for the conservation of energy and momentum is not affected by the density field, and the two conservation equations become

decoupled. This effect inhibits the RM instability, where both equations must be coupled. Therefore, we are interested in a more general form of the EoS, thus, further extensions are required to adapt the model to the simulation of flows obeying an ideal gas equation of state, given as [101],

$$p = (\Gamma - 1)(\epsilon - \rho c^2), \quad (3.1)$$

where $\Gamma = c_p/c_v$ and c_p and c_v are specific heats at constant pressure and volume, respectively, and $\rho = nm$ is the mass density. At low temperatures, i.e., $\frac{mc^2}{k_B T} \gg 1$, $\Gamma = 5/3$ while for high temperatures, i.e., $\frac{mc^2}{k_B T} \ll 1$, $\Gamma = 4/3$. The ultrarelativistic equation of state, $\epsilon = 3p$, is recovered by setting $\Gamma = 4/3$ and considering the limit $\rho c^2 \ll \epsilon$.

Note that throughout this chapter, in order to provide a more general study, we use the mass density (ρ) instead of the number density (n), such that the results can be also applicable for the fluids with different atomic masses.

As discussed in the previous chapter, in the relativistic LB method based on the model of Marle for the collision operator, the macroscopic variables can be calculated by solving a system of equations, corresponding to the moments of the equilibrium distribution. However, for the case of the ideal gas equation of state, this system of equations cannot be solved due to the fact that the first and the second order moments are coupled. This problem can be solved by using the model of Anderson-Witting [1] for the collision operator, see Eq. 2.33. The model of Anderson-Witting is based on the Landau-Lifshitz decomposition [14]. Hence, the macroscopic variables can be calculated using the following relation [61]

$$U_\alpha T^{\alpha\beta} = \epsilon U^\beta. \quad (3.2)$$

Which means that ϵ and U^β are the largest eigenvalue and corresponding eigenvector of T_α^β , respectively.

The largest eigenvalue and the corresponding eigenvector can be calculated numerically using the power iteration method. Power iteration algorithm starts with an approximation for the biggest eigenvector \hat{U}_0^β , which should have a nonzero component in the direction of an eigenvector associated with

the biggest eigenvalue, and the iteration is proceed as follows:

$$\dot{U}_{k+1}^\alpha = T_\beta^\alpha \dot{U}_k^\beta, \quad (3.3)$$

and the velocity is defined by normalizing \dot{U}_{k+1}^β :

$$U_{k+1}^\beta = \frac{c^2 \dot{U}_{k+1}^\beta}{\dot{U}_{k+1}^\beta \dot{U}_{\beta,k+1}}. \quad (3.4)$$

The eigenvalue is calculated using Eq. 3.2, where the iteration is considered to be converged when $|(\epsilon_{k+1} - \epsilon_k)/\epsilon_k| < 10^{-8}$.

Knowing the values of the energy density and velocity from the above-mentioned procedure, the density would be evaluated using the first order moment and the pressure using the equation of state.

Additionally, in order to adapt the model to an ideal gas equation of state, discretized distribution function should be modified as follows:

$$\begin{aligned} f_i^{\text{eq}} = & \frac{3}{4}(\epsilon + p) \frac{c_0^2}{c_t^2} w_i \left\{ 1 + \frac{3(\Gamma - 1)(\epsilon - \rho c^2) - \epsilon}{(\Gamma - 1)(\epsilon - \rho c^2) + \epsilon} \right. \\ & + \frac{52^2[\epsilon - (\Gamma - 1)(\epsilon - \rho c^2)]}{33 \times 7^2[(\Gamma - 1)(\epsilon - \rho c^2) - \epsilon]} \delta_{i0} + c_a^x c_a^y \chi^x \chi^y \\ & + c_a^x c_a^z \chi^x \chi^z + c_a^y c_a^z \chi^y \chi^z + \left(\frac{c_t \chi^0}{2c_0^2} - \frac{\chi^0}{\nu c_0} \right) (\vec{c}_a \cdot \vec{\chi}) \\ & \left. + \frac{4}{15} [(c_a^x)^2 (\chi^x)^2 + (c_a^y)^2 (\chi^y)^2 + (c_a^z)^2 (\chi^z)^2 - \frac{4}{\nu^2} (\vec{\chi} \cdot \vec{\chi})] \right\}, \end{aligned} \quad (3.5)$$

where δ_{i0} is the Kronecker delta function. The second and third terms in the big curly bracket represent the deviation from the ultrarelativistic EoS and, as expected, in the ultrarelativistic limit, they go to zero.

The discretized form of the Boltzmann equation using the model of Anderson-Witting has the following form:

$$\begin{aligned} f_i(\vec{x}, t + \delta t) - f_i(\vec{x}, t) + \frac{c_0}{c_t} \frac{\delta t}{\delta x} [h_i^a(\vec{x} + \delta x \vec{e}_a) - h_i^a(\vec{x})] = \\ - \frac{c_0 \nu \delta t (\xi_\mu \chi^\mu / \nu^2)}{\tau c_t} [f_i(\vec{x}, t + \delta t) - f_i^{\text{eq}}(\vec{x}, t)] + \frac{c_0 \nu \delta t}{c_t} \lambda_i \sum \partial_a^2 f_i(\vec{x}, t). \end{aligned} \quad (3.6)$$

Like before, the evolution of the density also follows the dynamics of the Boltzmann equation given by Eq. (3.6), without the λ_i coefficient term and

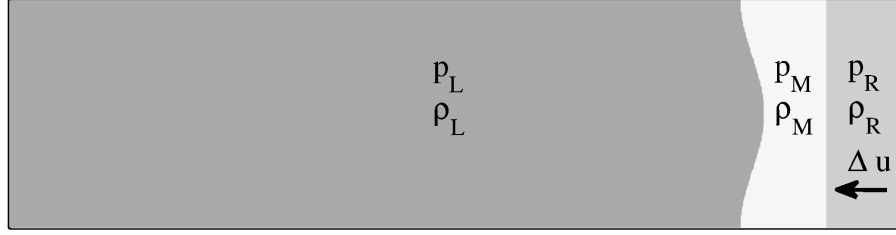


Fig. 3.1: Schematic of the initial condition of the two-dimensional shock tube RM instability. The arrow shows the post-shock velocity on the right hand side of the shock.

by replacing $(\xi_\mu \chi^\mu / \nu^2)$ by unity. The discretized distribution function for the first moment is the same as Eq. (2.100), replacing n by ρ .

For the Anderson-Witting model the shear viscosity can be calculated as:

$$\eta = \frac{4}{5}(\epsilon + p)\left(\tau - \frac{1}{2}\right). \quad (3.7)$$

We know that using the relativistic Boltzmann model leads to viscous hydrodynamics. However, it has been shown that viscosity has a negligible effect on the perturbation amplitude in the non-relativistic shock tube RM instability [13], and we can expect the same behavior in relativistic hydrodynamics. We will show later that our numerical results confirm the negligible effect of viscosity on the growth rate of the instability for the relativistic case, at least in the range of viscosities considered here.

3.2 Results and discussions

3.2.1 Numerical Simulation

For the two-dimensional simulation of the shock tube RM instability, a domain of 200×1200 lattice cells is considered. Periodic boundary conditions are considered at top and bottom boundaries of the domain, while inlet boundary condition is applied to the right boundary by setting the distribution functions to the equilibrium distributions and for the left boundary

outlet boundary conditions is considered by copying the distributions from the neighbouring cells. For all simulations, the value of $\delta t/\delta x = 0.15$ and $\alpha = 0.25$, and we take $\Gamma = 5/3$. We refer to numerical units throughout this chapter. For all the simulations considered here, a shock wave with the velocity $\beta = 0.94$, travelling from right to left (see Fig. 3.1), is passing through a sinusoidal perturbation in the density located at $x_p = 1000$ cells. The initial position of the shock wave is at $x_s = 1100$ cells. The single mode sinusoidal perturbation at the interface is: $x = x_p + a \sin(\frac{\pi}{2} + \frac{2\pi}{\lambda}y)$, where a is the pre-shock amplitude of the interface and λ is the width of the domain. Note that, hereafter the subscripts R , M , and L refer to the right hand side of the shock, the region between the shock and the initial perturbation, and the left hand side of the perturbation, respectively (see Fig. 3.1). The densities at the two sides of the perturbation are different, and the initial pressure is forced to be constant across the perturbation, i.e., $p_L = p_M$. The simulations are performed assuming the equation of state of an ideal gas for various pre-shock density ratios ρ_L/ρ_M and various values of the relativistic Mach number of the shock wave, $Ma_r = u_s \gamma(u_s)/c_{so} \gamma(c_{so})$, where the velocity of the shock u_s and the sound velocity c_{so} can be computed as [98, 101]:

$$\frac{u_s^2}{c^2} = \frac{(p_R - p_M)(\epsilon_R + p_M)}{(\epsilon_M + p_R)(\epsilon_R - \epsilon_M)}, \quad \frac{c_{so}^2}{c^2} = \frac{\Gamma(\Gamma - 1) \frac{p_M}{n_M}}{\Gamma \frac{p_M}{n_M} + \Gamma - 1}. \quad (3.8)$$

The values of the pre and post-shock pressures are calculated in such a way as to obtain the desired value Ma_r , while $\rho_R = 1$ and $\rho_M = 0.5$ and the velocity of the shock is fixed. Also, to fulfil the shock condition, on the right hand side of the shock, the corresponding velocity jump (post-shock velocity) due to the shock wave should be applied which can be calculated as following: the relative velocity between pre and post-shock velocities, u_{12} , for a standing shock can be calculated as [61]:

$$\frac{u_{12}^2}{c^2} = \frac{(p_R - p_M)(\epsilon_R - \epsilon_M)}{(\epsilon_M + p_R)(\epsilon_R + p_M)}. \quad (3.9)$$

For a moving shock where the pre-shock velocity is zero this relation gives the relative velocity between the shock and the post-shock velocity. Therefore, the post-shock velocity, Δu , can be computed by using the relativistic

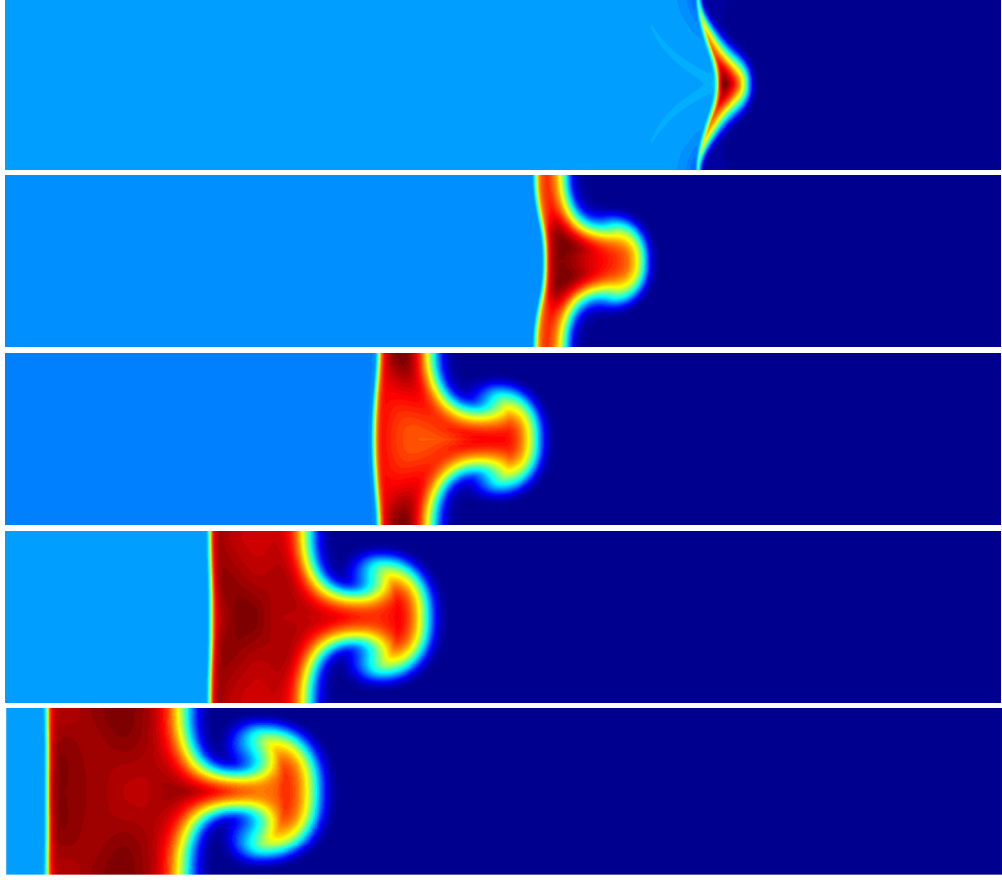


Fig. 3.2: Snapshots of the density field in the shock tube RM instability for $\rho_L/\rho_M = 28$ and $Ma_r = 2.4$ at different times. From the top to the bottom, snapshots correspond to the time $t = 180$, $t = 450$, $t = 720$, $t = 990$ and $t = 1260$, respectively. Blue to red denote low and high densities, respectively.

expression of the relative velocity, namely:

$$u_{12} = \frac{u_s - \Delta u}{1 - u_s \Delta u / c^2}. \quad (3.10)$$

The schematic design of the initial conditions is shown in Fig. 3.1.

In the RM instability, the light fluid penetrates the heavy one generating bubbles and the heavy fluid penetrates the light one giving rise to spikes. Fig. 3.2 shows the density field and the evolution of the bubble and the spike for the case $\rho_L/\rho_M = 28$, $Ma_r = 2.4$ and $a = 32$ (spatial numerical units) at

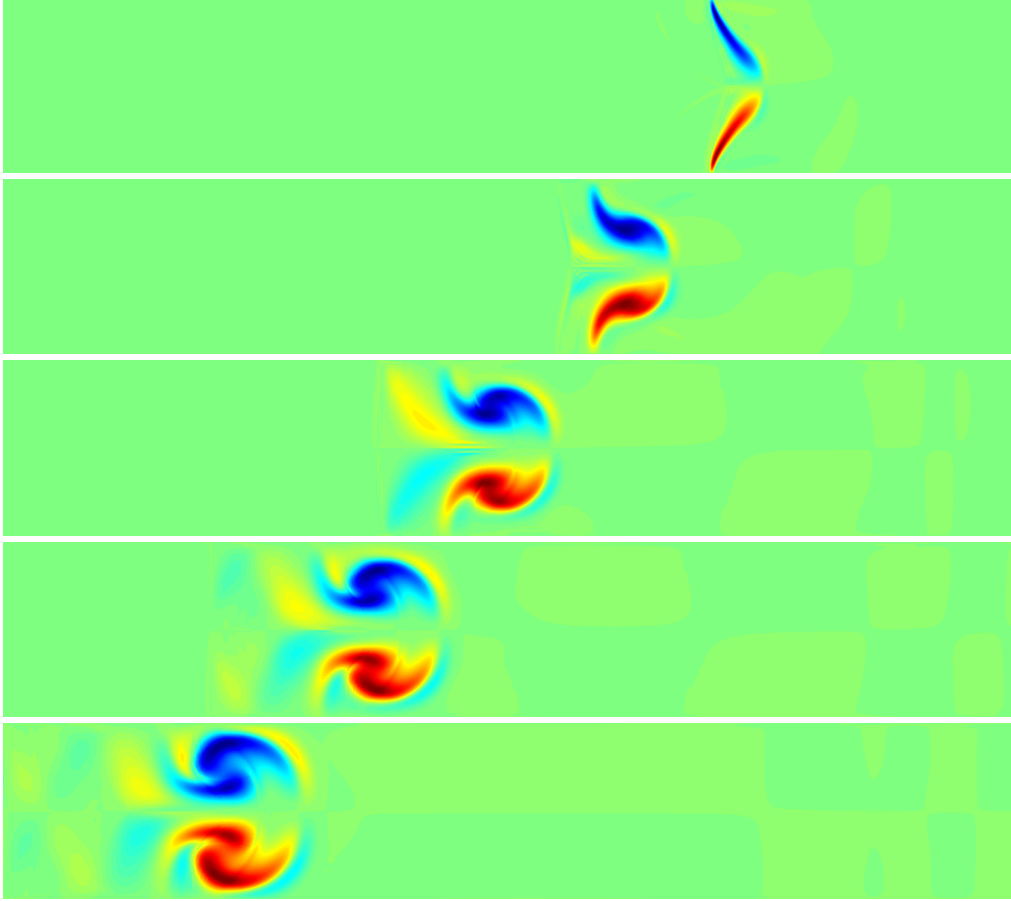


Fig. 3.3: Snapshots of the vorticity field in the shock tube RM instability for $\rho_R/\rho_L = 14$ and $Ma_r = 2.4$ at different times. From the top to the bottom, snapshots correspond to the time $t = 180$, $t = 450$, $t = 720$, $t = 990$ and $t = 1260$, respectively. Blue and red denote highest positive (counter-clockwise) and highest negative (clockwise) vorticity, respectively.

different times, after the shock wave passed through the initial perturbation. The amplitude of the perturbation grows in time and finally, the spike forms the characteristic mushroom shape of the instability. It is worth mentioning that the passage of the shock wave through the heavy fluid causes an increase in its density, due to the compression, which is well visible in Fig. 3.2.

The mechanism producing the instability can be described using the dynamics of the vorticity field. Vorticity is deposited on the perturbed interface by the misalignment of the pressure gradient of the shock wave and the density gradient at the fluid interface and is maximum near the points of minimum deflection and decays to zero at points of maximum deflection. For a single mode sinusoidal initial perturbation this results in two counter-rotating vortices as shown in Fig. 3.3. The distribution and evolution of these vortices would then result in increasing the amplitude of the perturbation in time, as well as the formation of the mushroom structure.

For the purpose of comparison, we have also performed a numerical simulation of the non-relativistic RM at the same density ratio and Mach number as in Fig. 3.4(a), i.e., $\rho_L/\rho_M = 28$ and $Ma = 2.4$. The initial condition is constructed the same way as for the relativistic case and the corresponding results are presented in Fig. 3.4(b). Here, in order to draw a proper comparison between the two cases, and given that we are simulating viscous hydrodynamics, the Reynolds number is also the same for both cases.

Thus, following Ref. [85], we define the relativistic Reynolds number for the shock tube relativistic RM instability as $Re_r = (\epsilon + p)u_s\gamma(u_s)\lambda/\eta$, where η is the shear viscosity. For the non-relativistic numerical simulations, we have used the lattice Boltzmann model proposed in Ref. [62], where a coupled double distribution function thermal LB method with flexible specific heat ratio is presented for the compressible Navier-Stokes equations. In this LB method, a distribution function based on a multispeed lattice is used to recover the compressible continuity and momentum equations, while the compressible energy equation is recovered by another distribution function. The second distribution function is then coupled to the density distribution function via the thermal equation of state and in order to obtain an adjustable specific heat ratio, a constant related to the specific heat ratio is

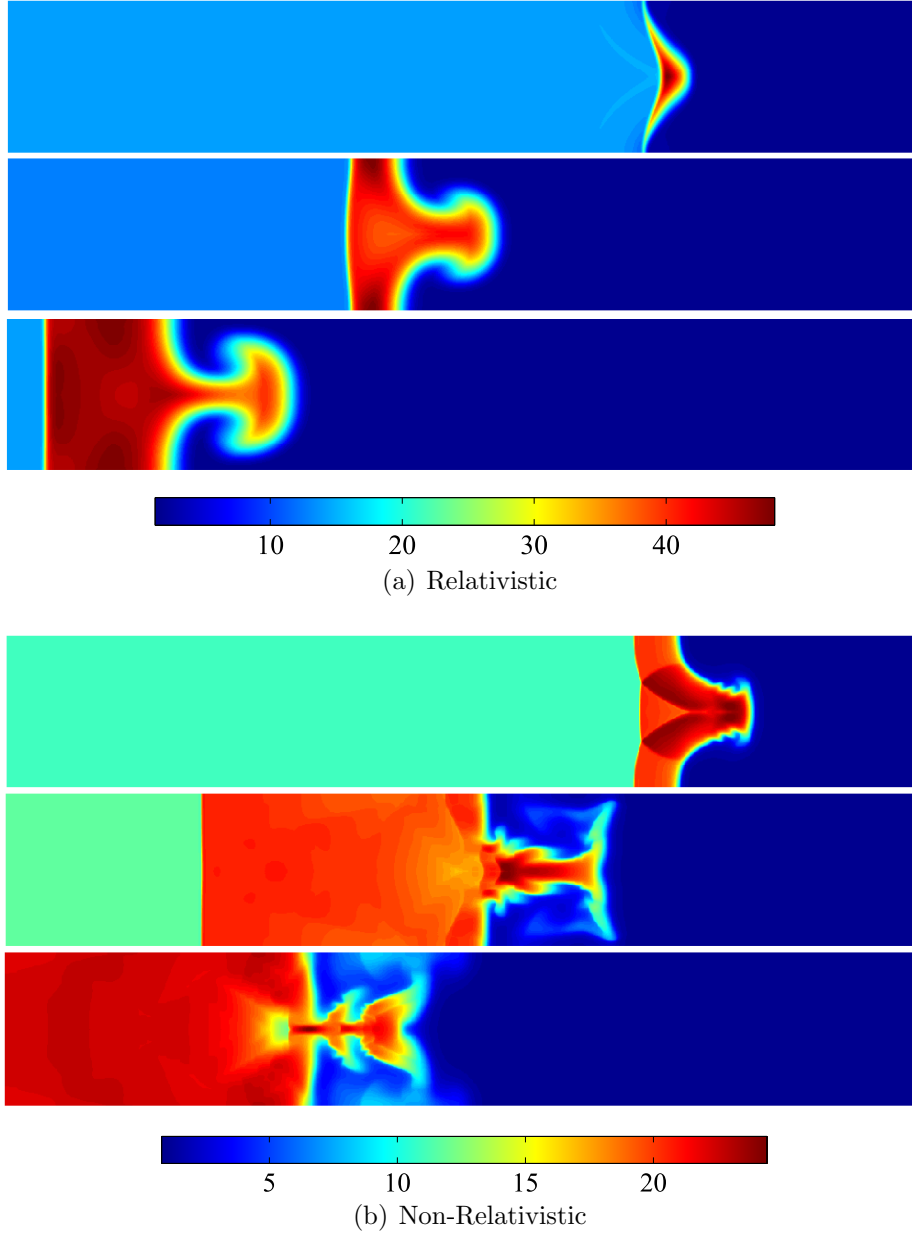


Fig. 3.4: Comparison of the density field in the 2D shock tube RM instability for (a) relativistic case and (b) non-relativistic case when $\rho_L/\rho_M = 28$ and $Ma_r = Ma = 2.4$ at different times. For both cases, from the top to the bottom, snapshots corresponds to the times $t = 180$, $t = 720$, and $t = 1260$, respectively and blue to red denote low to high densities, respectively.

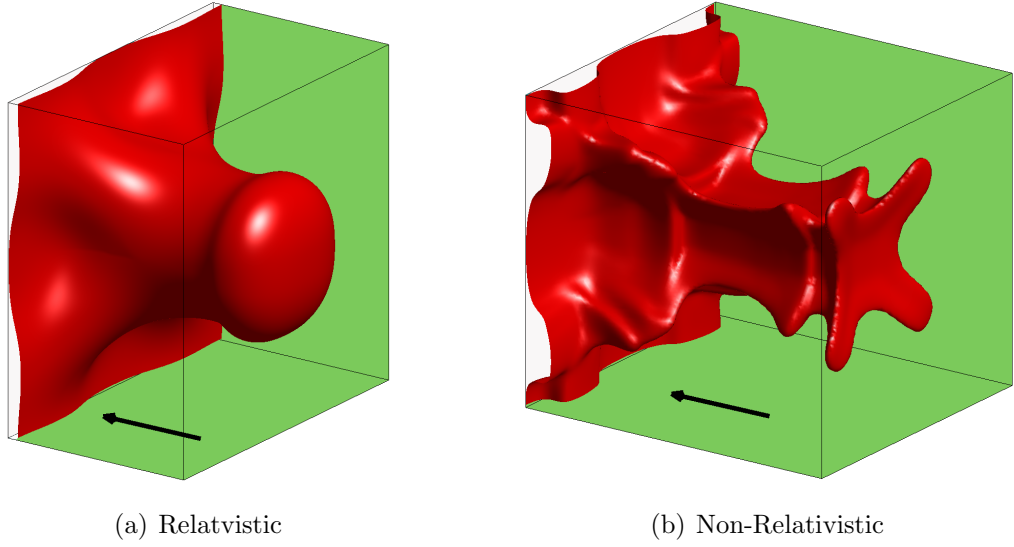


Fig. 3.5: Snapshots of the spikes in the 3D shock tube RM instability with square cross section when the pre-shock density ratio is 28 and the Mach number is 2.4 at time $t = 570$ for (a) relativistic and (b) non-relativistic case. Arrows show the direction of the shock wave.

introduced into the equilibrium distribution function [62].

Fig. 3.4(b) shows that, in the non-relativistic RM, the amplitude of the perturbation grows much faster at early times, which leads to faster development and more complex structures of the instability at later times. We shall further discuss this matter later. Note that the density jump across the shock wave is higher in the relativistic case than in the non-relativistic case.

The same behaviour can be also seen in Fig. 3.5, where the results for the simulation of the 3D shock tube RM instability with square cross section is presented, with $\rho_L/\rho_M = 28$ and $Ma_r = Ma = 2.4$. The 3D simulation was performed with the same parameters as before and using a lattice size of $1200 \times 200 \times 200$ cells in x , y and z direction, respectively. The initial condition for the perturbed surface is supposed to be $x = x_p + a \sin(\frac{\pi}{2} + \frac{2\pi}{\lambda(\theta)} r)$ with $a = 32$. Here, giving that y and z are zero at the center of the yz plane, $r = \sqrt{y^2 + z^2}$, $\theta = \tan^{-1}(y/z)$ and $\lambda(\theta)$ is chosen as the length of the center-passing line from one boundary to the opposite one. Like in the 2D case, the results show the faster growth of the instability and a more complex structure

of the spike for the non-relativistic case.

3.2.2 Linear stability analysis

To gain a deeper understanding on the relativistic RM instability, we perform a linear stability analysis. To this end, we begin by considering the growth of irregularities - in particular sinusoidal corrugations - at the interface between two fluids when a relativistic shock wave passes through the interface. In analogy with the non-relativistic case [97], we first approach the problem by studying the Rayleigh-Taylor instability, which takes place at the interface between two fluids at different densities, whenever one of the two fluids accelerates into the other. Subsequently, we replace the constant acceleration by an impulsive one approximating the shock wave.

The conservation equations of relativistic fluid dynamics (in the inviscid case) in the covariant form are $\partial_\alpha T^{\alpha\beta} = G^\beta$ and $\partial_\alpha N^\alpha = 0$, where $N^\alpha = \rho U^\alpha$ and G^β is the force density. The relativistic force density can be defined as

$$(G^\alpha) = \left(\frac{\vec{F} \cdot \vec{u} \gamma(u)}{c}, \vec{F} \gamma(u) \right), \quad (3.11)$$

where \vec{F} is the three-dimensional force density vector [14]. For the sake of simplicity, natural units i.e., $c = k_B = 1$ are assumed hereafter. For the Rayleigh-Taylor instability, we consider $\vec{F} = (\epsilon + p)\vec{g}$, where \vec{g} is the acceleration (gravity).

By inserting the corresponding relation for the moments in the relativistic conservation equations, and performing some simple algebra we get the relativistic continuity and motion equation in the inviscid case and in the presence of an external force as following:

$$\frac{\partial(\rho\gamma)}{\partial t} + \vec{\nabla} \cdot (\rho\gamma\vec{u}) = 0, \quad (3.12)$$

$$(\epsilon + p)\gamma^2 \left(\frac{\partial\vec{u}}{\partial t} + \vec{u} \cdot \vec{\nabla}\vec{u} \right) + \vec{u} \frac{\partial p}{\partial t} + \vec{\nabla} p = \gamma \left(\vec{u}(\vec{F} \cdot \vec{u}) - \vec{F} \right). \quad (3.13)$$

To calculate the amplitude growth rate of the disturbance at the interface, and without loss of generality, we deal with this problem in two dimensions. Thus, small perturbations are assumed for the velocity along

x and y directions, i.e., δu and δv , and the physical variables such as the density and pressure, i.e., δp and $\delta \rho$. For the disturbance, we write $A(x, y, t) = A_k(x) \exp(iky + \omega t)$, where A can be replaced by δu , δv , δp and $\delta \rho$, as well as the amplitude of the perturbation $h(t)$. Here $k = 2\pi/\lambda$ is the wave number, λ is the initial perturbation wavelength and ω is the wave frequency of the perturbations.

We suppose that at $t = 0$ the interface is located at $x = 0$, and the only non-zero component of \vec{g} is in x direction, i.e., g . Assuming that pressure and density are only functions of x , we substitute the perturbed quantities in the conservation equations. Note that, in our relativistic shock tube configuration, since the post-shock velocity Δu remains constant, thus giving a constant value for γ , we can expect that when the shock wave is far enough from the interface, the conservation equation for density will be reduced to $\vec{\nabla} \cdot \vec{u} = 0$, i.e., incompressibility condition. Dropping the nonlinear terms and considering initial equilibrium in the interface, i.e., $\partial p / \partial t = 0$, we obtain a system of linear differential equations. Solving these equations, and considering $\omega / kc^2 \ll 1$ (in the limit of full dispersion relation), we find the relation between ω and k , known as dispersion relation:

$$\omega^2 = \frac{(\rho_2 - \rho_1)gk}{\gamma(2p + \epsilon_1 + \epsilon_2)}, \quad (3.14)$$

where ϵ_1 (ρ_1) and ϵ_2 (ρ_2) are the energy (density) at both sides of the interface. Hence, the amplitude of the perturbed interface grows according to

$$\frac{\partial^2 h(t)}{\partial t^2} = \omega^2 h(t). \quad (3.15)$$

In order to find a relation for the relativistic RM instability, as mentioned, we replace the constant acceleration by an impulsive acceleration mimicking the shock wave. Let Δu be the increment of velocity due to this impulsive acceleration, we have $g(t) = \Delta u \delta(t)$, where $\delta(t)$ is the Dirac delta function. Integrating Eq. (3.15) and using the fact that $\int g(t) dt = \Delta u$, we obtain the asymptotic relation for the growth rate of the perturbation amplitude in the linear regime of the relativistic RM instability:

$$v_f = \frac{\partial h(t)}{\partial t} = \frac{(\rho_2 - \rho_1)kh_0\Delta u}{\gamma(2p + \epsilon_2 + \epsilon_1)}. \quad (3.16)$$

Here, h_0 is the initial amplitude of the perturbation. Note that the linear assumption is well justified only as long as the interface amplitude is small, i.e., $h/\lambda \lesssim 0.1$ [11] and nonlinear effects become important when the amplitude becomes larger. Additionally we expect this relation to overestimate the growth rate at the early times of the linear regime, when shock wave is still close to the interface and the compressibility effects are important, therefore, the condition $\vec{\nabla} \cdot \vec{u} = 0$ is not fulfilled any more. However, when the shock wave is far enough from the interface, this condition is fulfilled and the relation should give a good estimate for the asymptotic growth rate in the linear regime given that post-shock values of the parameters are used. This means that in Eq. 3.16, post-shock values of ρ_1 , ρ_2 and h_0 are used and Δu and p are the velocity jump and pressure at the interface.

Moreover, Eq. (3.16), is a general expression and does not depend on the equation of the state. Thus, ϵ can be replaced by the corresponding function of density and pressure according to the equation of state. In the non-relativistic limit when $\gamma \rightarrow 1$, using the equation of state of an ideal gas [101], i.e., $\epsilon + p = (\frac{1}{\gamma-1} + 1)p + \rho$, and considering $k_B T \ll mc^2$ (such that the pressure can be ignored with respect to the rest mass density), we get the well known linear growth rate of the non-relativistic RM instability, i.e., $v_f = Akh_0\Delta u$, where $A = (\rho_2 - \rho_1)/(\rho_2 + \rho_1)$ is the Atwood number [97]. Likewise, we can introduce the relativistic Atwood number A_r , using the ideal gas equation of state, obtaining:

$$A_r = \frac{\rho_2 - \rho_1}{\rho_2 + \rho_1 + 2(\frac{1}{\gamma-1} + 1)p}. \quad (3.17)$$

Clearly, for the same value of the density ratio, ρ_2/ρ_1 , we always have $A_r < A$, due to the contribution of the pressure to the inertia of the relativistic fluid. Thus we can write Eq. (3.16) as $v_f = (A_r/A)Akh_0\Delta u/\gamma$. The fact that $A_r < A$ for the same value of the density ratio, relevant at high temperatures, decreases the amplitude growth rate compared to the non-relativistic RM instability. Moreover, relativistic effects decrease the amplitude growth rate, due to the Lorentz's factor, γ . These arguments are in line with previous observations in graphene flow [75], which shows that relativistic effects delay the onset of turbulence and also agrees with our numerical results. In Fig. 3.6,

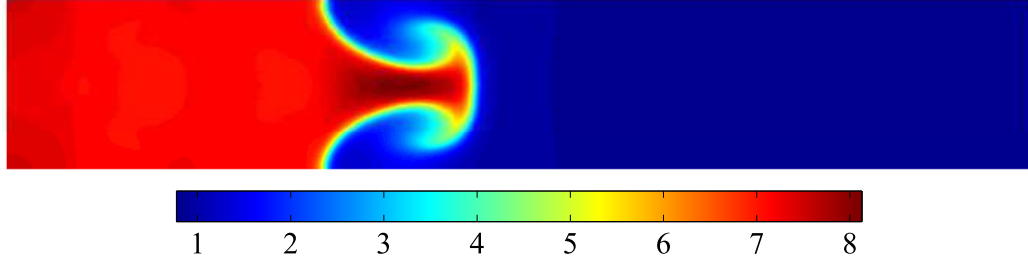


Fig. 3.6: Snapshots of the density field in the 2D shock tube non-relativistic RM instability with $\rho_L/\rho_M = 8$ and $Ma = 2.4$ at time $t = 1260$. Blue to red denote low to high densities, respectively.

we report the results for the non-relativistic RM instability with a lower density ratio, $\rho_L/\rho_M = 8$, than for the one used in Fig. 3.4(b). From this, we can conclude that by lowering the density ratio, hence the Atwood number, only a simple-structured instability grows at late times, which is qualitatively similar to the relativistic case in Fig. 3.4(a). This shows that the qualitative difference between the relativistic and non-relativistic case in Figs. 3.4 and 3.5, is due to the fact that A is high for the non-relativistic case while A_r has a low value for the relativistic case, for the same density ratio.

3.2.3 Linear and nonlinear perturbation amplitude

In the RM instability, the perturbation amplitude, $h(t)$, is calculated by measuring the distance between the tips of the spike and the bubble divided by two. Note that this definition of the perturbation amplitude is well-posed if the spike and bubble are symmetric. For the range of the parameters considered here, since $A_r \ll 1$, the growth of bubble and spike are symmetric and therefore this condition is indeed fulfilled.

As previously mentioned, Eq. (3.16) is expected to be accurate enough to describe the linear growth rate of the instability, except for early times. In the sequel, we investigate the validity of this assumption.

For a fixed value for the adiabatic index and wave number, we consider different values of density ratios and relativistic Mach numbers, i.e., $8 \leq$

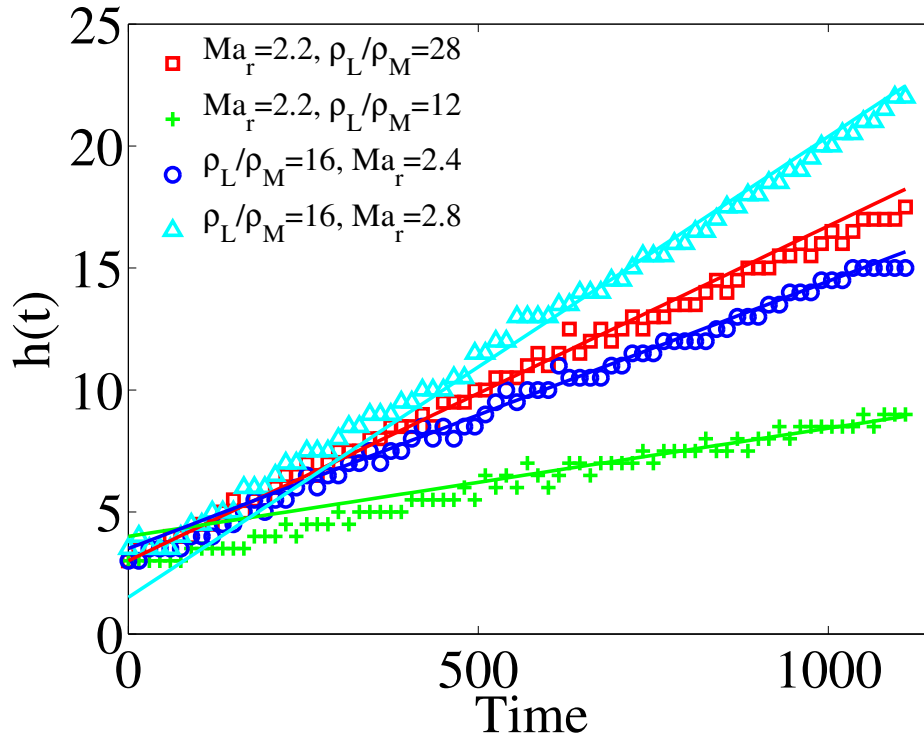


Fig. 3.7: Results of the numerical simulation $h(t)$ versus time for different Ma_r and density ratios in the linear regime with $a = 8$. Solid lines show the theoretical growth rate, Eq.(3.16).

$\rho_L/\rho_M \leq 28$ and $2 \leq Ma_r \leq 3$. Fig. 3.7 shows the results of $h(t)$ for some of the considered cases for different values of Ma_r and density ratios in the linear regime when $a = 8$. By increasing Ma_r , as well as the density ratio, the amplitude grows faster. The results are compared with the analytical relation, Eq. (3.16), from which we can observe a good agreement between the numerical and theoretical results. However, for early times, where $\vec{\nabla} \cdot \vec{u} \neq 0$, the growth rate is smaller than the analytical expression. Note that $t = 0$ is defined as the time when the shock wave has just passed the interface, thus the post-shock values of the initial amplitude are smaller than the pre-shock initial amplitude, because of the compression due to the shock wave.

Fig. 3.8 shows the numerical results for $h(t)$ in the nonlinear regime with $a = 16$. Since we are interested in a general relation for the relativistic RM instability, v_f can be taken as an approximation for the initial growth rate of the nonlinear regime. In order to describe the effect of the nonlinearity on the growth rate, we propose the following relation, ensuring its decrease in time, $\partial h(t)/\partial t = v_f/(1 + bt)$.

This implies that the amplitude behaves like $h(t) - h(0) = (v_f/b) \ln(1 + bt)$, where b should be a function of ρ_L/ρ_M and Ma_r .

By fitting all numerical results for different density ratios and Ma_r , we obtain the following expression for the nonlinear regime (see Fig. 3.8)

$$\frac{\partial h(t)}{\partial t} = \frac{v_f}{1 + a_1 \left(\frac{\rho_L}{\rho_M}\right)^{1/2} Ma_r t}, \quad (3.18)$$

where $a_1 = 9.033 \times 10^{-5}$ is a constant value independent of the Mach number and the density ratio.

The fact that nonlinear growth is roughly proportional to t^{-1} at late times has also been observed in the non-relativistic case [11]. In addition, in the inset of Fig. 3.8 the effect of viscosity on $h(t)$ is presented for two cases, $a = 8$ and $a = 16$. In both cases it can be observed that the viscosity, in the range considered here, has negligible effects on the growth rate.

In order to explore the consequences of relativistic effects, we plot the asymptotic linear growth rate of the instability, Eq. (3.16) as a function of the temperature, for different equations of state (see Fig. 3.9). Here, we compare the

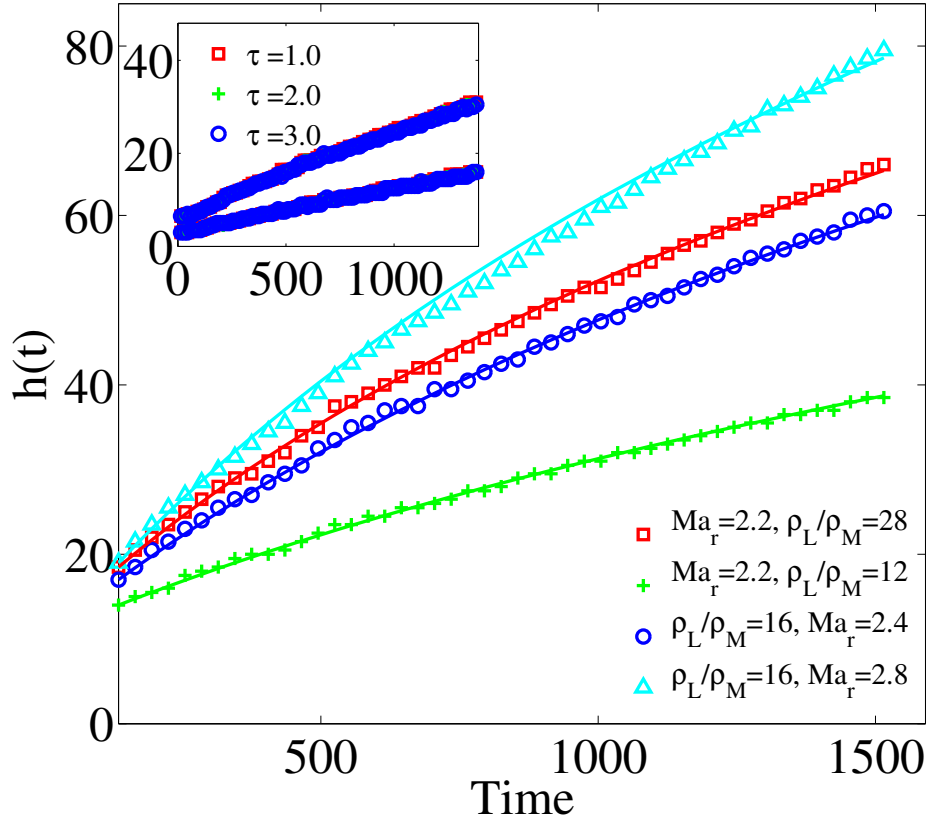


Fig. 3.8: Results of the numerical simulation $h(t)$ versus time for different Ma_r and density ratios in the nonlinear regime. Solid lines are the resulting $h(t)$, using the proposed relation, Eq.(3.18). In the inset, $h(t)$ versus time for different values of viscosities (relaxation time τ in the relativistic LB model) are presented for $Ma_r = 2.2$, $\rho_L/\rho_M = 20$ and for the cases $a = 8$ (lower curve) and $a = 16$ (upper curve).

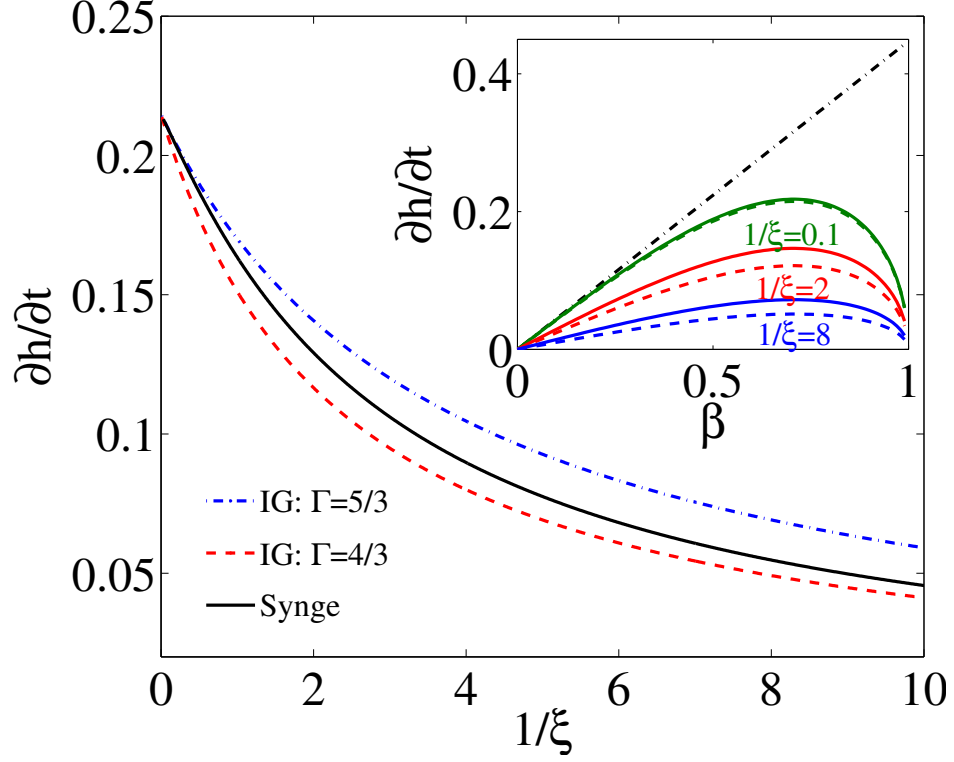


Fig. 3.9: Perturbation growth rate in the linear regime calculated from Eq.(3.16) as a function of temperature for different equations of state. The blue dashed-dotted line and red dashed line are for the ideal gas equation of state (Eq. (3.1)) for $\Gamma = 5/3$ and $\Gamma = 4/3$, respectively, and the solid black line is for the Synge equation of state, Ref. [114]. In the inset, the effect of increasing $\beta = \Delta u/c$ on the perturbation growth rate in the linear regime (using the ideal gas equation of state: solid lines for $\Gamma = 5/3$ and dashed lines for $\Gamma = 4/3$), for different temperatures, comparing with the non-relativistic RM instability (dashed-dotted line) is shown.

ideal gas equation of state, Eq.(3.1), for two values of $\Gamma = 5/3$ and $\Gamma = 4/3$, with the equation of state for an ideal relativistic gas developed by Synge [114].

We have defined the dimensionless parameter $\xi = mc^2/k_B T$ (inverse temperature) and the following parameters are considered: $h_0 = 20$, $k = 0.025$, $\Delta u = 0.6$, and the post-shock density ratio is 18. Fig. 3.9 shows that the perturbation growth rate depends on the equation of state and decreases with increasing temperature, i.e., increases with relativistic effects. It is worth noting that the Synge equation of state behaves like the ideal gas equation of state with $\Gamma = 5/3$ at low temperatures, while it goes to the one with $\Gamma = 4/3$ in the limit of high temperatures.

In the inset of Fig. 3.9, the linear growth rate of the amplitude versus the velocity, $\beta = \Delta u/c$, for the ideal gas equation of state, is compared with the respective relation for the non-relativistic RM instability, for different temperatures. Note that for low velocities and low temperatures, both relations agree, but by further increasing β and/or temperature, the perturbation amplitude decreases as compared to the non-relativistic case. Additionally, each relativistic result in the inset of Fig. 3.9 is presented for two cases, $\Gamma = 5/3$ and $\Gamma = 4/3$, and, as expected, the results of $\Gamma = 5/3$ are closer to the non-relativistic ones.

3.3 Cooling effect of Richtmyer-Meshkov instability

Here we study a non-trivial system where the RM instability can appear, and in particular we are interested in the thermal effects of the instability. We investigate the interaction of two relativistic Mach shocks, generated by traveling of particles in a relativistic fluid, and the resulting RM instability. In the presence of disturbance traveling in a relativistic fluid, the energy-momentum conservation can be expressed as $\partial_\mu T^{\mu\nu} = S^\nu$, where the source term S^ν is the energy deposited by the disturbance and can be written in

the form [9, 5]:

$$S^\nu = \frac{1}{(\sqrt{2\pi}\sigma)^2} \exp \left\{ -\frac{[\vec{x} - \vec{x}_{jet}]^2}{2\sigma^2} \right\} \left(\frac{dE}{dx}, \vec{0} \right), \quad (3.19)$$

where the momentum deposition is ignored and the disturbance is assumed to travel with the velocity of light. Here \vec{x}_{jet} is the location of the disturbance, where $\sigma = 0.04$ and $dE/dx = 7.5$ are considered.

Additionally, to include the external force, S^ν , into the relativistic LB model, we need to calculate the discretized forcing term which will be added to the discretized Boltzmann equation. Assuming the external force as $(S^\nu) = (S^0, \vec{S})$, the discretized forcing term which should be added to the discretized Boltzmann equation, Eq. (3.6), becomes:

$$S_i = \frac{2\nu^2 c_0^3}{3c_t^3} (1 + I) \frac{\delta t}{\delta x} w_i (\Gamma e - (\Gamma - 1)\rho) \left[\frac{c_t S^0}{c_0 e} + \frac{\vec{\xi} \cdot \vec{S}}{p} \right], \quad (3.20)$$

where I is the contribution of the ideal gas equation of state defined as:

$$I = \frac{3(\Gamma - 1)(\epsilon - \rho c^2) - \epsilon}{(\Gamma - 1)(\epsilon - \rho c^2) + \epsilon} + \frac{52^2[\epsilon - (\Gamma - 1)(\epsilon - \rho c^2)]}{33 \times 7^2[(\Gamma - 1)(\epsilon - \rho c^2) - \epsilon]} \delta_{i0}. \quad (3.21)$$

For the numerical simulation of the interaction between two Mach cones, two domains with 500×500 and 250×250 cells are considered. All boundaries are taken as free outlets and the ideal gas equation of state is assumed with $\Gamma = 4/3$. The initial position of the disturbance moving along the x direction is $(L/3, L/2)$, while the disturbance moving along the y direction starts at $(L/2, 5L/6)$, L being the length of the domain. We take $\delta t/\delta x = 0.15$ and $\alpha = 0.25$.

In Fig. 3.10, we show that, after the interaction of two Mach cones, when the shock front of a Mach cone passes through the density variation which is caused by the other Mach cone, the RM instability starts to grow in the direction of the advancing shock front. In this figure, we also show that downstream the moving disturbance and due to the sweeping effect of the shock wave, the density decreases locally. It is worth mentioning that the current simulation shows only one particular case of the interaction of the Mach cones. Nevertheless, what causes the instability is the interaction of

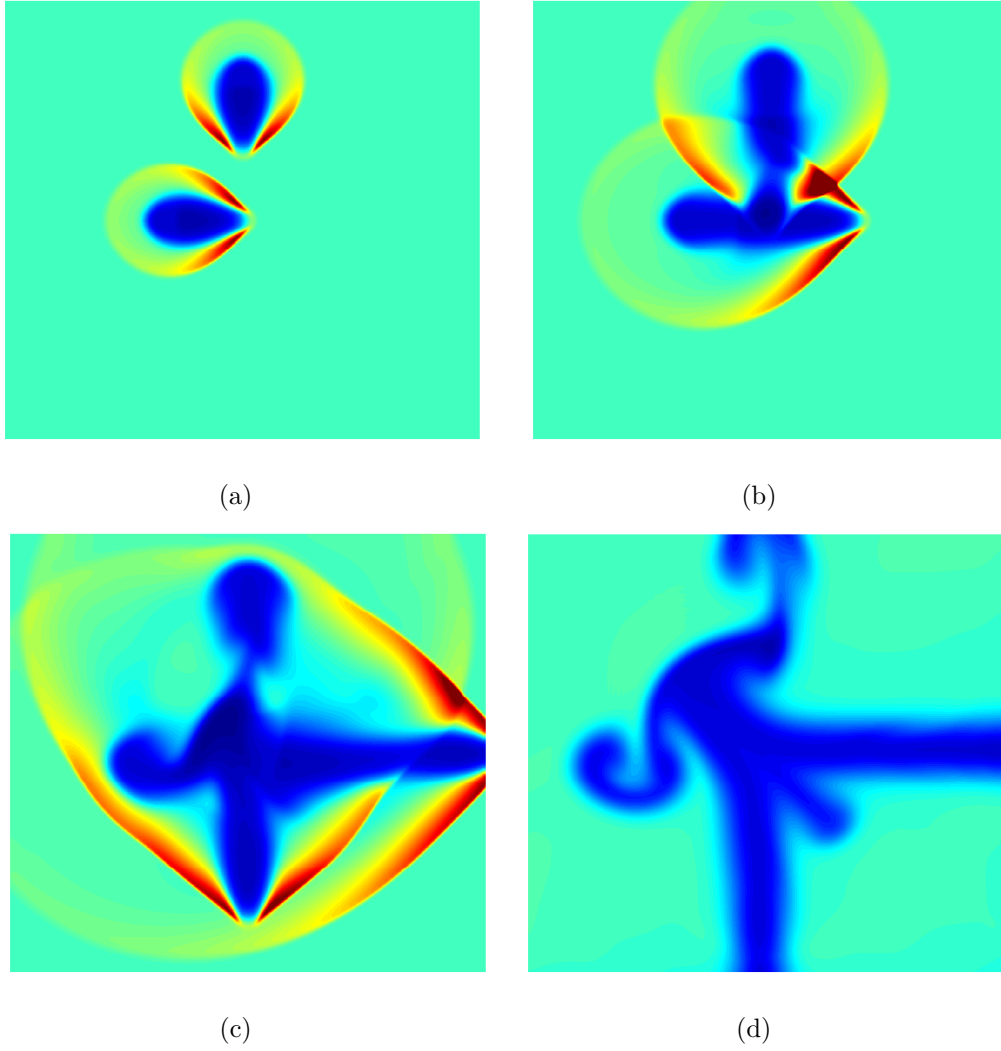


Fig. 3.10: Snapshots of the density profiles for two interacting Mach cones in a relativistic fluid at times (a) $t = 180$ (b) $t = 360$ (c) $t = 720$ (d) $t = 1200$. Here $T_{med} = 0.3$ and the domain is 500×500 . The red and blue colors denote high and low values of the density, respectively.

one Mach cone with the density fluctuation due to the passage of another Mach cone at earlier times.

Regarding the thermal behaviour of the fluid during this phenomenon, as expected, the passing disturbance in the medium increases the average temperature, since it deposits energy to the fluid according to Eq. (3.19). Here,

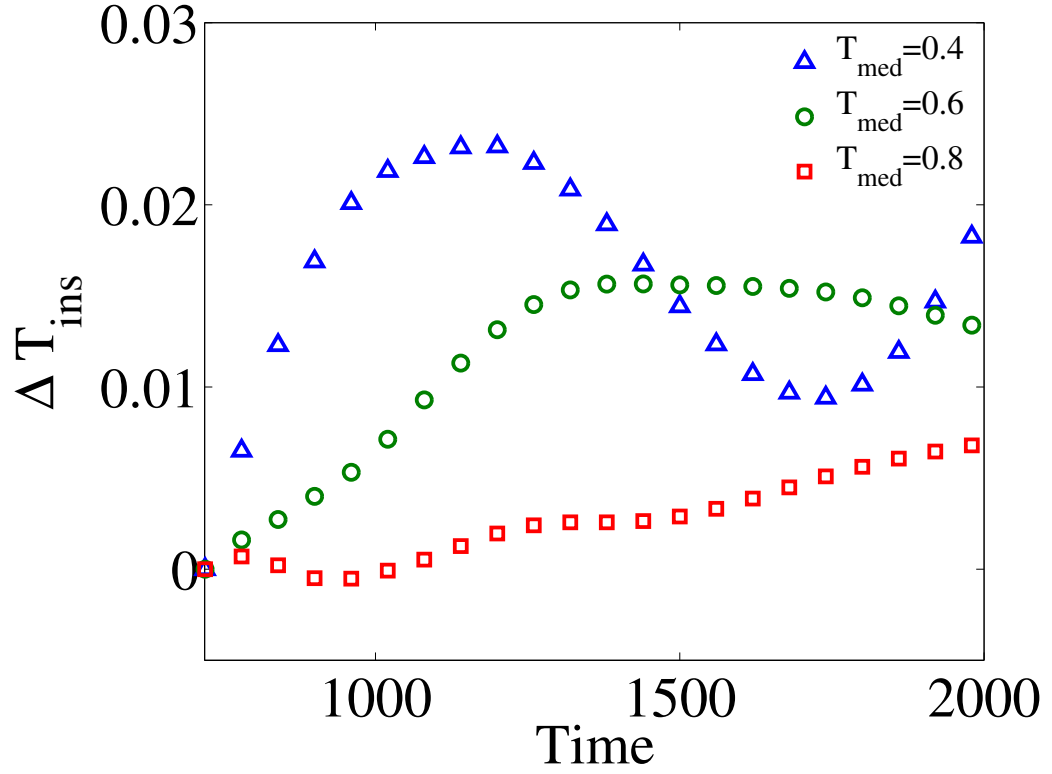


Fig. 3.11: Decrease in the average temperature of a relativistic fluid due to the RM instability developed as a result of the interaction of two Mach cones, for different initial temperatures, T_{med} . Here $\Delta T_{ins} = T_0 - T'_{med}$, with T'_{med} being the average temperature and T_0 the average temperature right after the disturbances have left the simulation zone. Thus, ΔT_{ins} denotes the decrease in temperature of the media compared with the time when the disturbances and shock waves had left the domain. Here the domain of simulation is 250×250 .

we are interested in the effects of the aforementioned RM instability on the average temperature. Thus, we compute the average temperature of the medium and compare it to the average temperature when the disturbances and shock waves have left the domain completely. In the absence of the instability, the temperature should remain constant because of the steady state condition. However, we see that, due to the presence of the instability, the temperature starts to decrease, see Fig. 3.11. The simulation is performed for different initial domain temperatures and we also observe that the decrease in the initial temperature enhances the cooling effect. This can be explained by realizing that relativistic effects, which are more dominant at higher temperatures, weaken the RM instability, as explained before. In fact, Eq. (3.16) suggests that the growth rate of the relativistic RM instability decreases as the temperature increases, i.e. the denominator increases in Eq. (3.16). This is in agreement with the results in Fig. 3.11, where we show that a higher initial temperature leads to a smaller decrease in the average temperature due to the RM instability, since the instability is weaker at higher temperatures. At this point, we have shown that the RM instability can appear during the interaction of Mach cones in a relativistic fluid, and that it contributes to the cooling of the medium. In order to single out the instability and to confirm its cooling effect, we consider a simplified configuration, namely the shock tube RM instability. The reason for considering a simple shock tube geometry is twofold; first, this is a standard geometry to study the RM instability, second, it is straightforward to compare the cases with and without the instability. For comparison, the cases without the instability are also simulated by simply setting $a = 0$ (unperturbed interface), while other parameters are the same as the ones for the case with the instability. The snapshots of the density and temperature profiles, for the perturbed case with the density ratio $\rho_L/\rho_M = 28$ and relativistic Mach number $Ma_r = 2.4$ at a late time of the instability, are presented in Fig. 3.12. By measuring the average temperature of the fluid on both cases, with (perturbed interface) and without (unperturbed interface) instability, the decrease in temperature due to the instability can be computed.

In Fig. 3.13, one can notice that in the case of a perturbed interface, the

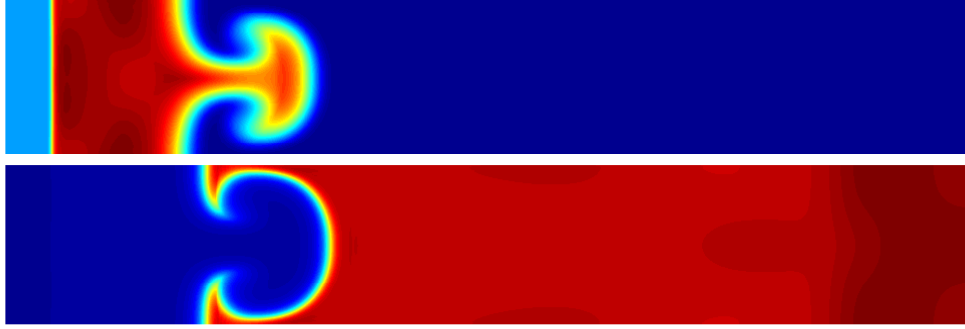


Fig. 3.12: Snapshots of the density (top) and temperature field (bottom) at $t = 1260$ in the shock tube RM instability with perturbed interface. Here, we consider the high density ratio $\rho_L/\rho_M = 28$ and $Ma_r = 2.4$. Blue and red colors denote low and high values, respectively.

average temperature is lower, where the cooling effect of the instability increases in time. This is in agreement with the results shown in Fig. 3.11. The results for different density ratios in Fig. 3.13 show that, as the density ratio increases, the decrease in the average temperature is enhanced. This is because at higher density ratios the instability grows faster, as predicted by Eq. (3.16).

Back to our original problem of Mach cone interaction, we explore the possible experimental observable consequences of the existence of this kind of interactions. To this purpose, we suggest to study the two-particle correlation (TPC) function [5, 6]. Our hydrodynamical calculations provide macroscopic quantities such as temperature and velocity fields. Thus, to compare the hydrodynamical results with experimentally measured observables (e.g. in quark-gluon plasma), a description of the conversion of the fluid into particles is needed. This can be achieved by the Cooper-Frye freeze-out approach, where the particle emission pattern is given by (see Ref. [21]):

$$\frac{dN}{p_T dp_T d\phi dy} = \int_{\Sigma} d\Sigma_{\mu} p^{\mu} \frac{A}{(2\pi)^2} \exp\left(-\frac{U^{\mu} p_{\mu}}{T}\right), \quad (3.22)$$

where $p_T = \sqrt{p_x^2 + p_y^2}$ is the transversal component of the momentum of a particle, ϕ is the azimuthal angle, A is the pre-factor for the Maxwell-

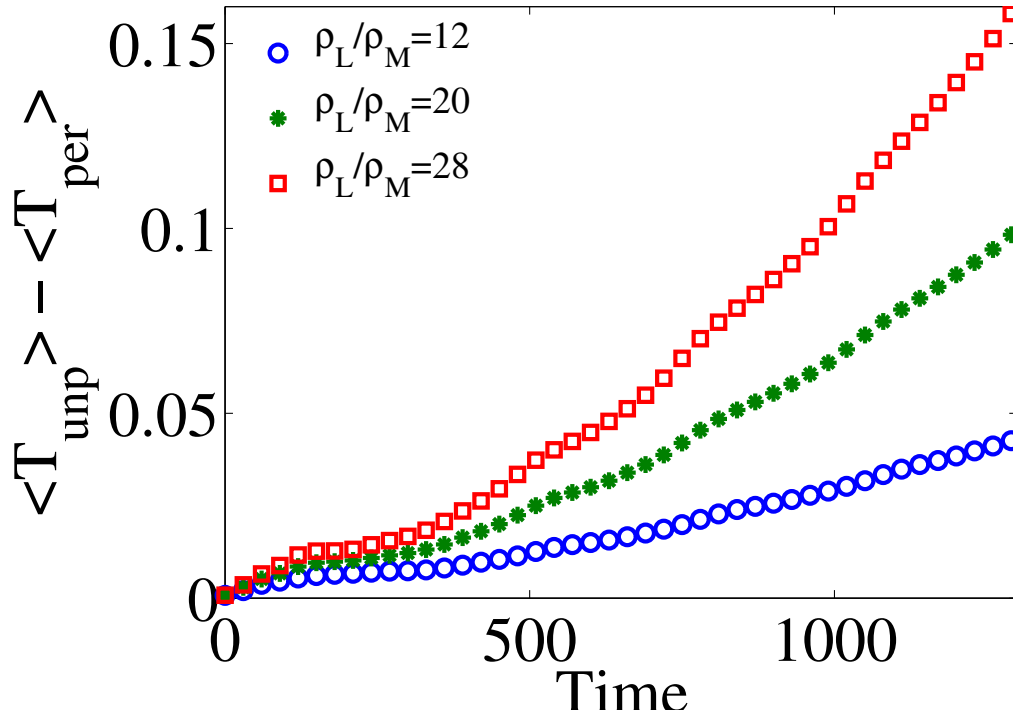
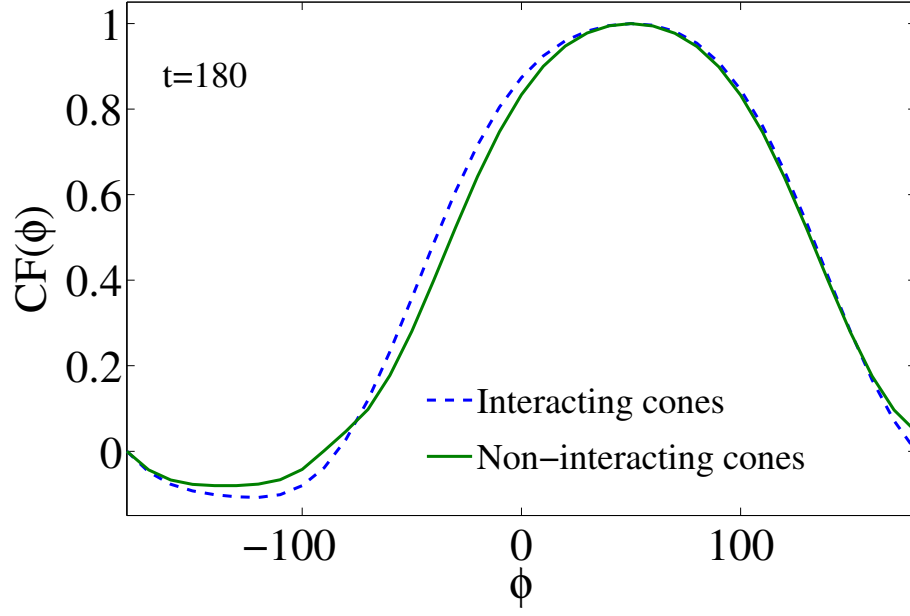
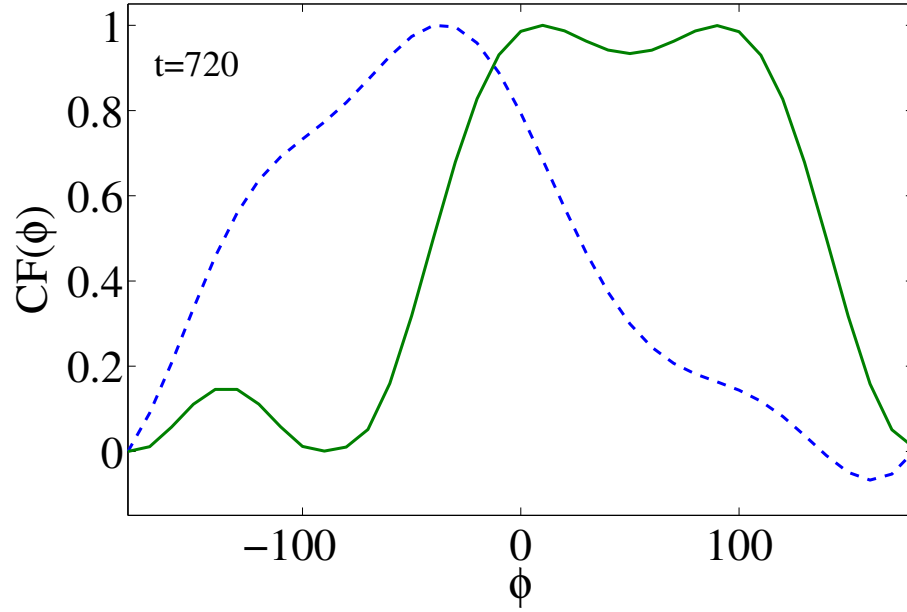


Fig. 3.13: Decrease of the average temperature due to the RM instability in a shock tube numerical experiment, for different density ratios. Here $\langle T_{\text{unp}} \rangle$ and $\langle T_{\text{per}} \rangle$ denote the average temperature when the RM instability is (perturbed interface) and is not (unperturbed interface) present, respectively. We have set $Ma_r = 2.4$.



(a)



(b)

Fig. 3.14: Two particle correlation (TPC) function for interacting and non-interacting Mach cones for the case $T_{med} = 0.3$ in a domain of 500×500 at time, (a) $t = 180$ (before the interaction), and (b) $t = 720$ (after the interaction).

Jüttner distribution function, $y = 1/2 \ln \frac{E+p_z}{E-p_z}$ is called rapidity and $d\Sigma_\mu$ is the integral surface in space-time. Using isochronous freeze-out hypersurface, $d\Sigma_\mu = (1, \vec{0})d^2\vec{x}$, we have [5]:

$$\frac{dN}{p_T dp_T d\phi dy} = \frac{A}{(2\pi)^2} \int d^2\vec{x} m_T \cosh y \times \exp\left\{-\frac{\gamma}{T}[m_T \cosh y - p_T u_x \cos \phi - p_T u_y \sin \phi]\right\} \quad (3.23)$$

where $m_T = E/\cosh y$.

Upon defining:

$$\frac{dN_{ass}}{p_T dp_T d\phi dy} = \int_\Sigma d\Sigma_\mu p^\mu \left[\frac{A}{(2\pi)^2} \exp\left(-\frac{U^\mu p_\mu}{T}\right) - f_0 \right], \quad (3.24)$$

with f_0 the Maxwell Jüttner distribution function at $T = T_{med}$ and $\vec{u} = \vec{0}$, the correlation function at mid-rapidity ($y = 0$) is given by [5]:

$$CF(\phi) = \frac{1}{N_{max}} \left(\frac{dN_{ass}(\phi)}{p_T dp_T d\phi dy} - \frac{dN_{ass}(0)}{p_T dp_T d\phi dy} \right) \Big|_{y=0}, \quad (3.25)$$

where N_{max} normalizes the correlation. In this study the value of $p_T = 1$ is considered.

We propose that by measuring the TPC function, one can investigate the existence of the Mach cone interaction. Hence, using our numerical data, the TPC function for two interacting Mach cones is compared to its non-interacting counterpart (see Fig. 3.14). The TPC function for non-interacting Mach cones is calculated by summing up the TPC function of each Mach cone in the absence of the other one. Fig. 3.14a shows that prior to the interaction, both curves are in good agreement, while after the interaction (see Fig. 3.14b), the TPC function for the case of interacting Mach cones differs significantly from the non-interacting case. This shows that if the Mach cones shock waves do not interact with each other, the TPC functions for the non-interacting and interacting cases should remain the same, while, due to the interaction, the functions deviate from each other.

3.4 Summary

Summarizing, in this chapter we have shown that relativistic effects weaken the RM instability. We have developed a linear stability analysis to predict the asymptotic amplitude growth rate of the interface in the linear regime. Based on these results, we have introduced the relativistic Atwood number, A_r , which is typically smaller than the non-relativistic one, A , for the same value of the density ratio. We have also proposed a nonlinear relation for the evolution of the interface amplitude for different values of density ratio and relativistic Mach number.

The numerical model used for the study of the relativistic RM instability is an extension of the relativistic LB model proposed in Ch. 2, capable of handling the ideal gas EoS.

Additionally, we have investigated Mach cone interactions and the resulting RM instability in a relativistic fluid. Our results show that the interaction of two Mach cone shock waves, and in particular the interaction of a shock front of a Mach cone with the density variations generated by the other one, leads to the growth of the RM instability in the direction of the advancing shock front. Regarding the thermal behaviour of this phenomenon, we have shown that the average temperature of the media decreases because of the instability.

To single out the effect of the instability on this cooling process, we have considered shock tube RM instability simulations, which confirm that the instability causes a decrease in the average temperature. Several simulations have been performed for different initial temperatures and density ratios, which demonstrate that decreasing the initial temperature and/or increasing the density ratio, enhances the cooling. This is in line with the analytical relation for the linear growth rate of the relativistic RM instability, Eq. (3.16), since decreasing the temperature and/or increasing the density ratio, enhances the instability.

We have also shown that the interaction of Mach cones significantly affects the TPC. Therefore, comparing the observed TPC with the measured TPC of non-interacting Mach cones, may provide a suitable tool to experimentally

identify the Mach cone interaction.

The results of this chapter may be relevant to phenomena characterised by the presence of RM instability and/or Mach cones in astrophysics, high energy physics, and plasma physics, where relativistic effects play a major role.

Furthermore, in the context of high energy physics, since quark-gluon plasma can be described by hydrodynamic models of nearly perfect fluids [64, 125], our results might also have some interest for the study of transport phenomena and EoS in quark-gluon plasmas, particularly in the regimes where such plasmas support shock-waves [45, 44].

Chapter 4

LB Model for Relativistic Magnetohydrodynamics

In this chapter we describe the derivation of an LB model for relativistic magnetohydrodynamics (see Ch. 1). The chapter is organised as follows: in Sec. 4.1 the principles of magnetohydrodynamics and the governing equations in the non-relativistic case are discussed in Sec. 4.2, the basic equations for resistive relativistic MHD are presented; in Sec. 4.3, the development of a lattice Boltzmann model for solving the governing equations is elaborated; in Sec. 4.4, validation tests for the model in the ideal and resistive regimes as well as several applications of the model in the context of relativistic magnetic reconnection are presented; and finally in Sec. 4.5, as a summary, an overall discussion of the model and the results are provided.

4.1 Magnetohydrodynamics

Magnetohydrodynamics is the study of the dynamics of the electrically conductive fluids in the presence of the electromagnetic fields. Electrical conductive materials are able to conduct an electric current and electrical conductivity is an intrinsic property that quantifies how strongly a given material conducts the current and is commonly represented by the Greek letter σ . Among others, one can mention plasmas, liquid metals, electrolytes and salt water as electrical conductive fluids.

The fundamental concept behind MHD is that magnetic fields can induce currents in a moving conductive fluid, which in turn creates forces on the fluid and also changes the magnetic field itself. The set of governing equations that describe MHD are a combination of the equations of fluid dynamics and Maxwell's equations of electromagnetism and because of the coupling between these differential equations, they should be solved simultaneously. Before discussing the relativistic MHD equations in the next section, let us have a look at the non-relativistic MHD. For the non-relativistic case the fluid's governing equations are the Navier-Stokes equations. For simplicity, we consider here the incompressible isothermal assumptions, meaning that the energy equation is irrelevant and the continuity equation for the fluid reduces to $\vec{\nabla} \cdot \vec{u} = 0$. The momentum equation has the form

$$\rho(\partial_t \vec{u} + \vec{u} \cdot \vec{\nabla} \vec{u}) = -\vec{\nabla} p + \mu \nabla^2 \vec{u} + \vec{J} \times \vec{B}, \quad (4.1)$$

where ρ is the density of the fluid, μ is the shear viscosity which is assumed to be constant, \vec{B} is the magnetic field vector and \vec{J} is the electrical current. The last term on the right hand side, $(\vec{J} \times \vec{B})$, is the so-called Lorentz force and represents the effect of the magnetic field on the fluid.

The governing equations for the electromagnetic fields are the Maxwell equations:

$$\vec{\nabla} \cdot \vec{E} = \frac{1}{\epsilon_0} \rho_c, \quad (4.2)$$

$$\vec{\nabla} \cdot \vec{B} = 0, \quad (4.3)$$

$$\frac{1}{c^2} \partial_t \vec{E} - \vec{\nabla} \times \vec{B} = -\mu_0 \vec{J}, \quad (4.4)$$

$$\partial_t \vec{B} + \vec{\nabla} \times \vec{E} = 0. \quad (4.5)$$

Here, \vec{E} is the electric field, ρ_c is the charge density, and ϵ_0 is the permittivity of free space which relates to the permeability of the free space, μ_0 , through the relation $c^2 \epsilon_0 \mu_0 = 1$.

The displacement current in the Ampère's law, i.e., $\frac{1}{c^2} \partial_t \vec{E}$ can be neglected in the non-relativistic case (see Ref. [42] and the references therein), thus we have

$$\vec{\nabla} \times \vec{B} = \mu_0 \vec{J}, \quad (4.6)$$

which results in a great simplification of the equations as we will describe in the following. First, the Lorentz force in the momentum equation can be simplified using Eq. (4.6) and the identity

$$\frac{1}{2}\vec{\nabla}(\vec{B} \cdot \vec{B}) = (\vec{B} \cdot \vec{\nabla})\vec{B} + \vec{B} \times (\vec{\nabla} \times \vec{B}). \quad (4.7)$$

Thus, we can write the Lorentz force only as a function of the magnetic field as

$$\vec{J} \times \vec{B} = \frac{(\vec{B} \cdot \vec{\nabla})\vec{B}}{\mu_0} - \vec{\nabla}\left(\frac{B^2}{2\mu_0}\right). \quad (4.8)$$

Therefore, the momentum equation will be

$$\rho(\partial_t \vec{u} + \vec{u} \cdot \vec{\nabla} \vec{u}) = -\vec{\nabla} p + \mu \nabla^2 \vec{u} + \frac{(\vec{B} \cdot \vec{\nabla})\vec{B}}{\mu_0} - \vec{\nabla}\left(\frac{B^2}{2\mu_0}\right), \quad (4.9)$$

Furthermore, Ohm's law couples the fluid's and Maxwell equations, which in the resistive non-relativistic case has the form:

$$\vec{J} = \sigma(\vec{E} + \vec{u} \times \vec{B}), \quad (4.10)$$

where σ is the conductivity of the plasma. Therefore, by replacing the current, \vec{J} , in the Ohm's law by Eq. (4.6) we can find the electric field, \vec{E} as a function of \vec{u} , \vec{B} and σ . Now by substituting this relation for the electric field in the Faraday's law, Eq. (4.5), we get

$$\partial_t \vec{B} = \vec{\nabla} \times (\vec{u} \times \vec{B} - \frac{1}{\mu_0 \sigma} \vec{\nabla} \times \vec{B}), \quad (4.11)$$

which describes the time evolution of the magnetic field. Note that in the non-relativistic case, because we could neglect the displacement current in the Ampère's law, it is possible to eliminate the electric field from the Maxwell equations. As expected, this will simplify the governing equations and the corresponding numerical methods to solve these equations. As we will discuss in the next section this is not the case for the resistive relativistic MHD, since the displacement current can not be ignored there.

Summarizing, for the non-relativistic, incompressible and isothermal case we only need to solve Eq. (4.9) and Eq. (4.11) with the following constraints

$$\vec{\nabla} \cdot \vec{u} = 0, \quad \vec{\nabla} \cdot \vec{B} = 0. \quad (4.12)$$

Note that because of the $\vec{u} \times \vec{B}$ term in Eq. (4.11), the value of \vec{u} should be known to solve this equation which means that Eq. (4.11) is coupled to Eq. (4.9) and they should be solved simultaneously.

Another approximation that further simplifies the MHD equations is the ideal MHD approximation, which holds when the conductivity is very high ($\sigma \rightarrow \infty$). As mentioned in Ch. 1, this approximation can be reasonably accurate in many MHD applications. In fact, ideal MHD is applicable if the fluid (plasma) is strongly collisional, so that the time scale of collisions is shorter than the other characteristic times in the system, and the resistivity ($\eta = 1/\sigma$) due to these collisions is small. In particular, the typical magnetic diffusion times over any scale length present in the system must be longer than any time scale of the system. In the ideal MHD limit the Ohm's law have the form

$$\vec{E} = -\vec{u} \times \vec{B}, \quad (4.13)$$

and the evolution equation for the magnetic field will be

$$\partial_t \vec{B} = \vec{\nabla} \times (\vec{u} \times \vec{B}). \quad (4.14)$$

As we will show later, like in the non-relativistic case, in the relativistic MHD the ideal approximation will also simplify the governing equations. For further information about the non-relativistic MHD see Ref. [23].

4.2 The resistive relativistic MHD equations

For resistive relativistic MHD, the hydrodynamics conservation equations can be written in the covariant form as

$$\partial_\mu N^\mu = 0, \quad \partial_\mu T_{\text{Total}}^{\mu\nu} = 0, \quad (4.15)$$

where N^μ is defined in Eq. (2.37) and $T_{\text{Total}}^{\mu\nu}$ is the total energy-momentum tensor defined as the sum of fluid energy-momentum tensor, Eq. (2.36), and the contribution of the electromagnetic fields, i.e.,

$$T_{\text{Total}}^{\mu\nu} = T_{\text{Fluid}}^{\mu\nu} + T_{\text{EM}}^{\mu\nu}, \quad (4.16)$$

with

$$T_{\text{EM}}^{\mu\nu} = \epsilon_0 (F^{\mu\rho} F_{\rho}^{\nu} + \frac{1}{4} F^{\rho\sigma} F_{\rho\sigma} \eta^{\mu\nu}), \quad (4.17)$$

where $F^{\mu\nu}$ is the Maxwell electromagnetic tensor defined as

$$(F^{\mu\nu}) = \begin{pmatrix} 0 & -E^x & -E^y & -E^z \\ E^x & 0 & -cB^z & cB^y \\ E^y & cB^z & 0 & -cB^x \\ E^z & -cB^y & cB^x & 0 \end{pmatrix}. \quad (4.18)$$

In addition to the mentioned hydrodynamics conservation equations, the governing equations for the electromagnetic fields, i.e., Maxwell equations, also need to be considered, which in the covariant form read as

$$\partial_{\nu} F^{\mu\nu} = -\mu_0 c I^{\mu}, \quad (4.19)$$

and

$$\partial_{\nu} F^{*\mu\nu} = 0, \quad (4.20)$$

where $(I^{\mu}) = (c\rho_c, \vec{J})$ is the four-vector of electric current where $F^{*\mu\nu}$ is the Faraday tensor defined as

$$F^{*\mu\nu} = \frac{1}{2} \epsilon^{\mu\nu\lambda\kappa} F_{\lambda\kappa}, \quad (4.21)$$

with $\epsilon^{\mu\nu\lambda\kappa}$ the Levi-Civita tensor.

By choosing an appropriate decomposition of the Maxwell tensor, one can show that Eqs. (4.19) and (4.20) yield the familiar Maxwell equations [14], i.e., Eqs. (4.2), (4.3), (4.4), (4.5). The equation for conservation of current

$$\partial_t \rho_c + \vec{\nabla} \cdot \vec{J} = 0, \quad (4.22)$$

can be obtained by taking the divergence of Eq. (4.4) by considering Eq. (4.2) and Eq. (4.3) as constraints.

Like in the non-relativistic case, the coupling between the fluid equations and Maxwell equations is expressed by Ohm's law. In general, the explicit form of the current four-vector I^{μ} depends on the properties of the electromagnetic

fields as well as the fluid variables. Here we use Ohm's law for a resistive isotropic plasma as [58]

$$\vec{J} = \sigma \gamma \left[\vec{E} + \vec{u} \times \vec{B} - \frac{(\vec{E} \cdot \vec{u})\vec{u}}{c^2} \right] + \rho_c \vec{u}. \quad (4.23)$$

It is worth mentioning that in the fluid rest frame Ohm's law becomes

$$\vec{J} = \sigma \vec{E}, \quad (4.24)$$

and in the limit of $\sigma \rightarrow \infty$ one can obtain the well-known result for ideal MHD, i.e., Eq. (4.13).

The major difference between the numerical models for ideal and resistive MHD originates from the fact that, in the ideal case, one can substitute the electric field \vec{E} in all the equations, using a simple algebraic relation, i.e., Eq. (4.13), and thus one can define the electromagnetic induction four-vector $F^{*\mu\nu}U_\nu$ [96]. This leads to a considerably simpler and less expensive numerical algorithm, compared with the resistive MHD.

To summarize the governing equations, and by replacing Eq. (4.23) into Eqs. (4.4) and (4.22), we have 12 equations, i.e., Eqs. (4.15), (4.4), (4.5) and (4.22) and 13 unknowns, i.e., \vec{u} , \vec{B} , \vec{E} , ϵ , p , n and ρ_c . This system of equations will be complete by including the equation of state. Here again, we consider the ideal gas equation of state [101]

$$p = (\Gamma - 1)(\epsilon - nc^2). \quad (4.25)$$

4.3 Lattice Boltzmann model for resistive relativistic MHD

In this section we describe our lattice Boltzmann model to solve the aforementioned governing equations.

4.3.1 Relativistic fluid equations

The LB model to solve the equations of motion of the fluid, i.e., Eq. (4.15), is an extension of the model introduced in Chs. 2 and 3, where the relativis-

tic Boltzmann equation, based on the Anderson-Witting collision operator is used. To include the contribution of electromagnetic fields in the total energy-momentum tensor, the distribution function is extended by adding the corresponding terms as will be discussed shortly.

For this model, the D3Q19 lattice configuration, described in Eq. (2.70) is used with its corresponding discretized weight functions, Eqs. (2.72),(2.73),(2.74), and lattice constants, Eq. (2.78). Also, the discretized form of the relativistic Boltzmann equation is the same as Eq. (3.6).

The discretized equilibrium distribution function to recover $T_{\text{Fluid}}^{\mu\nu}$ has been presented before in Eq. (3.5). Now, to include the electromagnetic contribution to the energy-momentum tensor, $T_{\text{EM}}^{\mu\nu}$, additional terms need to be added to this discretized distribution function. Let us elaborate the contribution of electromagnetic fields in the energy-momentum tensor by providing the components of $T_{\text{EM}}^{\mu\nu}$ using Eqs. (4.17) and (4.18). Thus, we have

$$T_{EM}^{00} = \frac{\epsilon_0}{2}(E^2 + c^2 B^2), \quad (4.26)$$

$$T_{EM}^{0i} = \frac{1}{\mu_0 c}(\vec{E} \times \vec{B})^i, \quad (4.27)$$

$$T_{EM}^{ij} = \epsilon_0 \left[-E^i E^j - c^2 B^i B^j + \frac{1}{2}(E^2 + c^2 B^2)\delta^{ij} \right], \quad (4.28)$$

where E^2 and B^2 are the magnitude of the electric and magnetic fields, respectively, and δ^{ij} is the Kronecker delta. Note that, adding these terms to the total energy-momentum tensor corresponds to adding the Lorentz force and Joule heating to the macroscopic equations. The following expression shows the complete discretized equilibrium distribution function which recov-

ers the total energy-momentum tensor with the ideal gas equation of state

$$\begin{aligned}
f_i^{\text{eq}} = & \frac{3}{4}(\epsilon + p) \frac{c_0^2}{c_t^2} w_i \left\{ 1 + \frac{3(\Gamma - 1)(\epsilon - nc^2) - \epsilon}{(\Gamma - 1)(\epsilon - nc^2) + \epsilon} \right. \\
& + \frac{361[\epsilon - (\Gamma - 1)(\epsilon - nc^2)]}{33[(\Gamma - 1)(\epsilon - nc^2) - \epsilon]} \delta_{i0} + c_a^x c_a^y \chi^x \chi^y \\
& + c_a^x c_a^z \chi^x \chi^z + c_a^y c_a^z \chi^y \chi^z + \left(\frac{c_t \chi^0}{2c_0^2} - \frac{\chi^0}{\nu c_0} \right) (\vec{c}_a \cdot \vec{\chi}) \\
& + \frac{4}{15} [(c_a^x)^2 (\chi^x)^2 + (c_a^y)^2 (\chi^y)^2 + (c_a^z)^2 (\chi^z)^2 \\
& - \frac{4}{\nu^2} (\vec{\chi} \cdot \vec{\chi})] \left. \right\} + \frac{c_0^2}{c_t^2} \epsilon_0 w_i \left\{ \frac{3}{2} (c^2 B^2 + E^2) \right. \\
& + \frac{4}{5} [c^2 (\vec{B} \cdot \vec{B}) + \vec{E} \cdot \vec{E}] - \frac{\nu}{\sqrt{3}} [(\vec{B} \times \vec{E}) \cdot \vec{c}_a] \\
& + \frac{\nu^2}{5} [c^2 (\vec{B} \cdot \vec{c}_a)^2 + (\vec{E} \cdot \vec{c}_a)^2] - \frac{7\nu^2}{20} [c_a^x c_a^y E^x E^y \\
& + c_a^x c_a^z E^x E^z + c_a^y c_a^z E^y E^z] + c^2 (c_a^x c_a^y B^x B^y \\
& + c_a^x c_a^z B^x B^z + c_a^y c_a^z B^y B^z) \left. \right\}, \tag{4.29}
\end{aligned}$$

where the second curly bracket is the contribution of the electromagnetic fields.

Now, as we did before, to solve the equation for the conservation of number of particles, a separate distribution function, g_i , is considered. The equilibrium distribution function, g_i^{eq} , can be found in Eq. (2.100) and the discretized weight functions for the current cell configurations can be calculated as:

$$w'_0 = \frac{1}{10}, \quad w'_i = \frac{3}{10} - \frac{1}{6c_a^2}, \tag{4.30}$$

for $1 \leq i \leq 6$,

$$w'_i = \frac{1}{12c_a^2} - \frac{3}{40}, \tag{4.31}$$

for $7 \leq i \leq 18$. Note that computing the macroscopic variables for the fluid, is not any more straightforward. We shall elaborate this issue later on.

4.3.2 Maxwell equations

Now that the LB model for solving the fluid equations is discussed, let us explain our LB model for solving the governing equations of electromagnetic

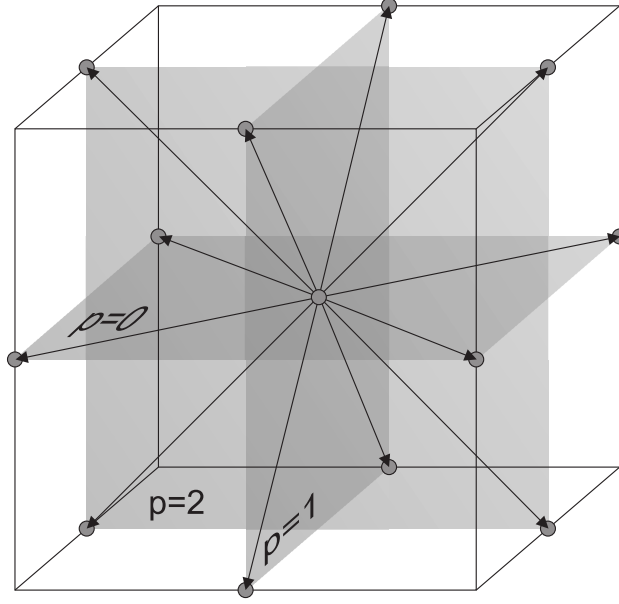


Fig. 4.1: The D3Q13 lattice configuration for the LB model to solve the Maxwell equations.

fields, i.e., Eqs. (4.4), (4.5), and (4.22), with (4.23) as Ohm's law. Our scheme is based on a 3D LB model for solving the Maxwell equations proposed in Ref. [78], where several modifications are required to couple it to our solver of the fluid equations (mainly by modifying the distribution functions) as well as to use it for relativistic MHD (by using the relativistic Ohm's law). For this purpose, we use a cubic regular grid with 13 velocity vectors (D3Q13), where four auxiliary vectors are assigned to each of the vectors (two for the electric field and two for the magnetic field) for calculating the magnetic and electric fields. A simple streaming-collision evolution for the distribution function is considered as

$$h_{ij}^p(\vec{x} + \vec{v}_i^p \delta t, t + \delta t) - h_{ij}^p(\vec{x}, t) = -\frac{1}{\tau_h} [h_{ij}^p(\vec{x}, t) - h_{ij}^{p(\text{eq})}(\vec{x}, t)], \quad (4.32)$$

and

$$h_0^p(\vec{x}, t + \delta t) - h_0^p(\vec{x}, t) = -\frac{1}{\tau_h} [h_0^p(\vec{x}, t) - h_0^{p(\text{eq})}(\vec{x}, t)], \quad (4.33)$$

where $h_{ij}^{p(\text{eq})}(\vec{x}, t)$ and $h_0^{p(\text{eq})}(\vec{x}, t)$ are the equilibrium distributions to be defined later. Here $i = 0, 1, 2, 3$ indicates the direction of the vectors, $p = 0, 1, 2$

shows the plane where the vectors lie, and $j = 0, 1$ shows each of the two auxiliary vectors for the electric or magnetic field. Thus, there are four directions on three planes which gives 12 vectors, and including the rest vector, in total we have 13 vectors. The vectors lie on the diagonals of each plane so we can write the components as

$$\vec{v}_i^0 = 2c \{ \cos(2i+1)\pi/4, \sin(2i+1)\pi/4, 0 \}, \quad (4.34)$$

$$\vec{v}_i^1 = 2c \{ \cos(2i+1)\pi/4, 0, \sin(2i+1)\pi/4 \}, \quad (4.35)$$

$$\vec{v}_i^2 = 2c \{ 0, \cos(2i+1)\pi/4, \sin(2i+1)\pi/4 \}, \quad (4.36)$$

in addition to the rest vector, i.e., $\vec{v}_0 = (0, 0, 0)$ (see Fig. 4.1). The distribution functions propagate with these vectors from cell to cell.

Moreover, in order to solve the Maxwell equations by the LB model we can write Ampère's law (Faraday's law) as time derivative of electric (magnetic) field plus the divergence of an antisymmetric tensor, i.e., Faraday's law can be written as

$$\frac{\partial \vec{B}}{\partial t} + \vec{\nabla} \cdot \Lambda = 0 \quad (4.37)$$

where,

$$\Lambda = \begin{pmatrix} 0 & -E^z & E^y \\ E^z & 0 & -E^x \\ -E^y & E^x & 0 \end{pmatrix}, \quad (4.38)$$

and Ampère's law

$$\frac{1}{c^2} \frac{\partial \vec{E}}{\partial t} - \vec{\nabla} \cdot \Phi + \mu_0 \vec{J} = 0 \quad (4.39)$$

with

$$\Phi = \begin{pmatrix} 0 & B^z & -B^y \\ -B^z & 0 & B^x \\ B^y & -B^x & 0 \end{pmatrix}. \quad (4.40)$$

These equations are conservation equations with antisymmetric tensors, i.e., Λ and Φ (unlike the fluid's equation, where the flux tensor is symmetric) and special treatments are required to solve these equations using LB models. Therefore, associated to each velocity vector \vec{v}_i^p we consider two electric auxiliary vectors \vec{e}_{ij}^p and two magnetic auxiliary vectors \vec{b}_{ij}^p , which are used to

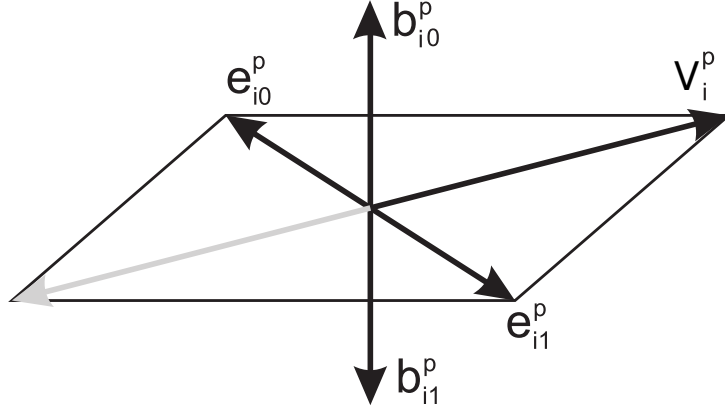


Fig. 4.2: The configuration of the auxiliary vectors for the LB model to solve the Maxwell equations.

compute the electromagnetic fields. These vectors are perpendicular to \vec{v}_i^p . However, \vec{e}_{ij}^p lies on the same plane as \vec{v}_i^p , while \vec{b}_{ij}^p lies perpendicular to this plane. More accurately, we define them as (see Fig. 4.2)

$$\vec{e}_{i0}^p = \frac{1}{2}\vec{v}_{[(i+3)\bmod 4]}^p, \quad \vec{e}_{i1}^p = \frac{1}{2}\vec{v}_{[(i+1)\bmod 4]}^p, \quad (4.41)$$

and

$$\vec{b}_{ij}^p = \frac{1}{2c^2}\vec{v}_i^p \times \vec{e}_{ij}^p, \quad (4.42)$$

where $(i)\bmod 4$ is a function that gives the remainder on the division of i by 4. To these vectors we shall add the null vectors, i.e., $\vec{e}_0 = (0,0,0)$ and $\vec{b}_0 = (0,0,0)$. This means that there are 13 different electric vectors and 7 different magnetic vectors. The computed tensors using these auxiliary vectors become antisymmetric because this procedure builds up the Levi-Civita tensor [78].

We also consider the term $(-\mu_0\vec{J})$ in Ampère's law as an external force. Therefore, the macroscopic fields can be computed as

$$\vec{E}' = \sum_{i=0}^3 \sum_{p=0}^2 \sum_{j=0}^1 h_{ij}^p \vec{e}_{ij}^p, \quad (4.43)$$

$$\vec{B} = \sum_{i=0}^3 \sum_{p=0}^2 \sum_{j=0}^1 h_{ij}^p \vec{b}_{ij}^p, \quad (4.44)$$

and

$$\rho_c = h_0 + \sum_{i=0}^3 \sum_{p=0}^2 \sum_{j=0}^1 h_{ij}^p. \quad (4.45)$$

Note that the effect of the external force still needs to be considered to get the correct electric field and \vec{E}' is the electric field before considering the external force.

It can be shown that to recover the Maxwell equations, for the current model, $\tau_h = \frac{1}{2}$ should be considered. Unlike the LB models for fluid dynamics, this value for the relaxation time does not lead to numerical instabilities because one can define an energy like quantity like

$$E_{\text{energy}} = h_o^2 + \sum_{i=0}^3 \sum_{p=0}^2 \sum_{j=0}^1 (h_{ij}^p)^2 \quad (4.46)$$

which is conserved during the collision step and guarantees that the distribution functions do not converge. This is the same as the LB schemes for the wave propagations [19, 20]. In addition, it is known that the configuration D3Q13, when used for the fluid's equations, has problems to reproduce the local momentum conservation during collision due to lack of symmetry. Nevertheless, because we are using $\tau_h = 1/2$, there are not viscous terms like in the fluid case, and D3Q13 is the lattice with the smallest number of vectors which can handle the symmetries we need for the Maxwell equations, as shown below.

For the case of $\tau_h = \frac{1}{2}$ the external force in Ampère's law can be included in a rather simple way, and \vec{E} becomes

$$\vec{E} = \vec{E}' - \frac{\delta t}{2} \mu_0 c^2 \vec{J}, \quad (4.47)$$

where, according to the Ohm's law, Eq. (4.23), \vec{J} is a function of \vec{E} . By replacing Ohm's law in Eq. (4.47) we obtain a system of three equations and three unknowns (E^x , E^y and E^z), which can be solved analytically. Having the values of each component of the electric field, \vec{J} can be calculated using Ohm's law, consequently. More discussion about computing the macroscopic variables shall be provided later.

The discretized equilibrium distribution functions to recover the correct Maxwell equations read as follows

$$h_{ij}^{p(\text{eq})}(\vec{x}, t) = \frac{1}{16} \vec{v}_i^p \cdot \vec{J} + \frac{1}{8c^2} \vec{E} \cdot \vec{e}_{ij}^p + \frac{1}{8} \vec{B} \cdot \vec{b}_{ij}^p, \quad (4.48)$$

and

$$h_0^{\text{eq}}(\vec{x}, t) = \rho_c. \quad (4.49)$$

A Chapman-Enskog expansion shows that the current model recovers Ampère's law, Faraday's law and current conservation, Eq. (4.22) [78]. The latter follows from the evolution of h_0 .

The divergence free condition for the magnetic field, Eq. (4.3), can be treated as a constraint on the initial condition, since by taking the divergence of Faraday's law one can show that the time derivative of $\vec{\nabla} \cdot \vec{B}$ is always zero. Therefore, if $\vec{\nabla} \cdot \vec{B} = 0$ is set for the initial condition it will hold for later times as well. The same is true for the Gauss law, Eq. (4.2), using Eqs. (4.4) and (4.22).

4.3.3 Coupling between fluid and electromagnetic fields

Having explained the appropriate solvers for fluid equations and Maxwell equations, we next discuss how to compute the macroscopic variables. As mentioned, the model of Anderson-Witting is used for the collision term in the solver for the equation of conservation of energy-momentum. Here again, the macroscopic variables can be calculated by solving an eigenvalue problem resulting from multiplying the relation for the energy-momentum tensor by the covariant four-vector velocity. Using the definition of the total energy-momentum tensor, Eqs. (4.16), (2.36) and (4.17) with the help of the relation $F^{\alpha\beta} F_{\alpha\beta} = 2(c^2 B^2 - E^2)$ we get

$$U_\mu [T^{\mu\nu} - \epsilon_0 F^{\mu\rho} F_\rho^\nu] = \left[\epsilon + \frac{\epsilon_0}{2} (c^2 B^2 - E^2) \right] U^\nu, \quad (4.50)$$

Here, $\left[\epsilon + \frac{\epsilon_0}{2} (c^2 B^2 - E^2) \right]$ and U^ν are the largest eigenvalue and corresponding eigenvector of the tensor $[T_\nu^\mu - \epsilon_0 F^{\mu\rho} F_{\nu\rho}]$, respectively. The total energy

-momentum tensor can be calculated using the relation $T^{\mu\nu} = \sum_{i=1}^{19} p_i^\mu p_i^\nu f_i$. On the other hand, the tensor $F^{\mu\rho} F_{\nu\rho}$ depends on \vec{E} and \vec{B} . As mentioned, for calculating \vec{E} the value of the external force, which depends on the velocity, is required. However, the value of the velocity is not yet computed. To solve this problem, we use the value of the electromagnetic fields from the previous time step to calculate the tensor $[T_\nu^\mu - \epsilon_0 F^{\mu\rho} F_{\nu\rho}]$. The largest eigenvalue and corresponding eigenvector (velocity) can be calculated numerically using the power method. Knowing the velocity, one can calculate the density using the first order moment relation, i.e., $N^\mu = nU^\mu = \sum_{i=1}^{19} p_i^\mu g_i$. After that, \vec{B} is calculated using Eq. (4.44). Having the velocity and magnetic field, \vec{E} can be computed using Eq. (4.43) and including the external force as described before. Thus, it is easy to compute \vec{J} using Ohm's law. Considering the eigenvalue $[\epsilon + \frac{\epsilon_0}{2}(c^2 B^2 - E^2)]$, it is possible to compute ϵ and through the equation of state Eq. (4.25) one can compute p . Finally, ρ_c can be calculated directly from Eq. (4.45). All the 13 unknown variables for each cell can be computed in this way. Note that using the values of electromagnetic fields from the previous time step to calculate the tensor, leads to an error which goes to zero as the time step (δt) decreases. In fact, in the next section our numerical results show that the error is ignorable.

Another point is to make the two solvers consistent in time evolution, which means that both solvers evolve in time simultaneously. In the electromagnetic LB model the relation $\delta x / \delta t = \sqrt{2}c$ holds. Thus, after choosing the value of $\delta x / \delta t$ in the fluid LB model, the velocity of light, c , in both models is adjusted such that δt and δx are equal.

4.4 Test simulations and applications

In this section, we present some numerical tests in order to validate our numerical model along with some applications for the resistive relativistic MHD (see Ref. [78] for the validation of the electromagnetic LB model). More specifically, test simulations for the propagation of Alfvén waves and the evolution of a self-similar current sheet are considered, and as applications for

the resistive relativistic MHD LB model, we study the magnetic reconnection driven by the Kelvin-Helmholtz instability and present the results of a 3D simulation of magnetic reconnection in a stellar flare due to the shear velocity in the photosphere. The purpose of the first test simulation (Alfvén wave), is to validate the numerical method in the limit of ideal MHD, while the second test is to validate the model recovering the correct dynamics in the resistive regime. In the following simulations numerical units are used and $\mu_0 = 1$ is considered.

4.4.1 Propagation of Alfvén wave

This test deals with the propagation of an Alfvén wave along a uniform background field in the limit of ideal MHD (when the electrical resistivity is negligible). The initial condition is the same as in Ref. [58]. We set $n = 1.0$, $p = 1.0$, $B^x = B_0 = 1.0$ and $B^y = 0.1$ and we consider a one dimensional domain defined in the range of $-1 \leq x \leq 1$, where the initial wave is located at $x_0 < x < x_1$, with $x_0 = -0.8$ and $x_1 = 0$. Outside the region of the initial wave it is assumed that $\vec{u} = \vec{0}$ and $B^z = 0$. Inside the region of initial wave we have

$$B^z = \eta_A B_0 \sin [2\pi(3x_*^2 - 2x_*^3)], \quad x_* = \frac{x - x_0}{x_1 - x_0}, \quad (4.51)$$

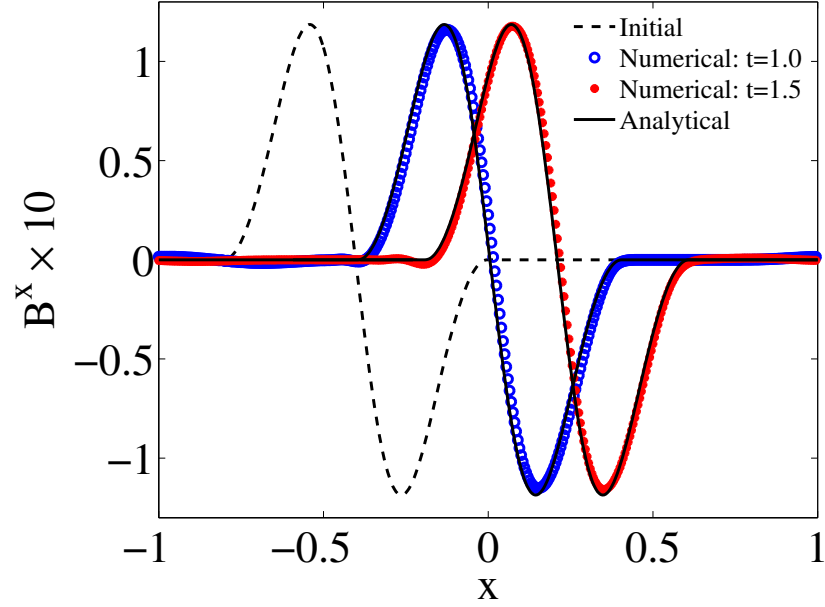
and

$$u^z = -\frac{v_A}{B_0} B^z, \quad u^x = u^y = 0, \quad (4.52)$$

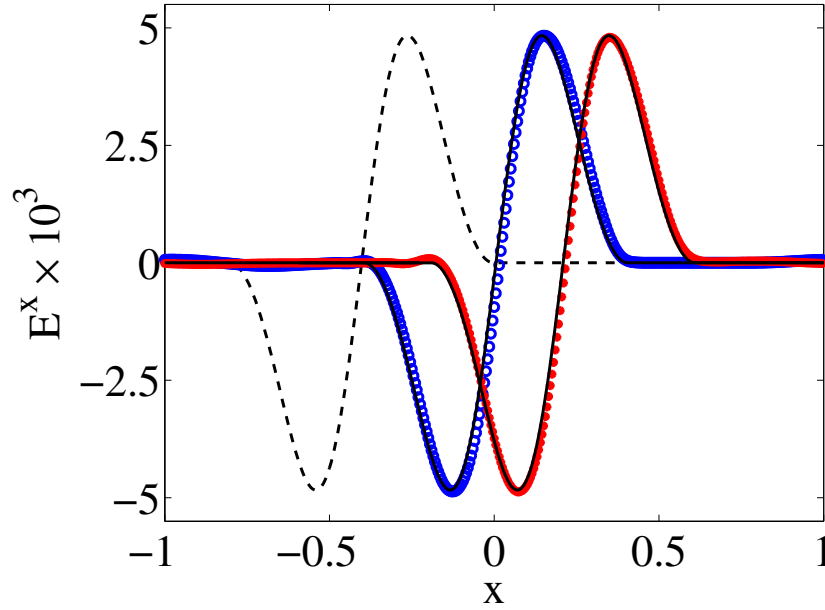
where the Alfvén velocity is defined as

$$v_A^2 = \frac{2B_0^2 c^2}{\epsilon + p + B_0^2(1 + \eta_A^2)} \times \left[1 + \sqrt{1 - \left(\frac{2\eta_A B_0^2}{\epsilon + p + B_0^2(1 + \eta_A^2)} \right)^2} \right]^{-1}. \quad (4.53)$$

Here we use the value of $\eta_A = 0.118591$ which gives $v_A = 0.40785$. Ohm's law for ideal MHD, i.e. Eq. (4.13) is used to calculate the initial electric field and Eq. (4.2) to measure the initial value of ρ_c . To achieve the ideal regime a very high conductivity ($\sigma = 10^5$ in numerical units) is considered.



(a)



(b)

Fig. 4.3: Results of the numerical test for the propagation of Alfvén waves in the limit of ideal MHD ($\sigma = 10^5$) for (a) magnetic field in z -direction and (b) electric field in x -direction. For both plots, the numerical results are shown at $t = 1$ (blue symbols) and at $t = 1.5$ (red symbols). The dashed black line shows the initial condition and solid black lines are the exact analytical solutions at the corresponding time.

The equation of state, Eq. (4.25), with $\Gamma = 4/3$ is used. The domain is discretized using 400 cells and we set $\delta x/\delta t = \sqrt{2}$, which gives $c = 1$. The value of τ for the fluid LB model is set to 1 and $\alpha = 0.1$. Open boundary conditions are considered at the left and right boundaries.

The simulation runs until $t = 1.5$ and the results are presented in Fig. 4.3. In the limit of ideal MHD the generated wave should travel with the Alfvén velocity without any distortion. Here we have compared our numerical results with the exact analytical solution of the ideal MHD at two different times, i.e., $t = 1.0$ and $t = 1.5$. The results are presented for the magnetic field in z -direction (Fig. 4.3(a)) and the electric field in x -direction (Fig. 4.3(b)). Fig. 4.3 shows that at each of the considered times and for both B^z and E^x , very good agreement is observed between the numerical and analytical results. Using the same optimization as before our relativistic MHD model achieve 0.5 Msup/s on a single core of an Intel CPU with 2.40 GHz clock speed. Note that, the analytical results are obtained by simply shifting the initial wave by the Alfvén velocity. Apart from validating the numerical method, this test shows the ability of the model to deal with high conductivity (low resistivity) regimes, recovering the ideal MHD limit.

4.4.2 Evolution of self-similar current sheets

After validating the model for the ideal MHD case, we consider here a test problem in the resistive case for which the evolution of a current sheet is investigated. We assume that the magnetic pressure ($B^2/2$) is much smaller than the plasma pressure (p), so that the fluid is not affected by the evolution of the current sheet and changes in the magnetic field. We know that when the magnetic field changes its sign within a thin layer a current sheet forms. Thus, for our case, we assume that the magnetic field has only a tangential component $\vec{B} = (0, B^y, 0)$, where $B^y = B(x, t)$ changes sign within a thin current sheet of width Δl . If the fluid is set initially to equilibrium, by considering a constant pressure in the domain, the evolution of the current sheet becomes a diffusion process. By assuming that the diffusion time-scale is much longer than the light propagating time-scale, we can neglect the

displacement current ($\partial_t \vec{E}$) in Ampère's law. In the rest frame, by inserting the relation $\vec{J} = \sigma \vec{E}$ in Ampère's law, using Faraday's law, and plugging in the mentioned one-dimensional magnetic field of the current sheet, one gets

$$\partial_t B^y - \frac{1}{\sigma} \partial_x^2 B^y = 0. \quad (4.54)$$

As the diffusion process continues and the width of the current sheet becomes much larger than the initial width (Δl), the expansion becomes self-similar and the exact solution has the form

$$B(x, t) = B_0 \operatorname{erf} \left(\frac{1}{2} \sqrt{\sigma \zeta} \right), \quad \zeta = \frac{x^2}{t}, \quad (4.55)$$

where B_0 is the magnetic field outside of the current sheet and erf is the error function.

For the numerical test a domain of $-1.5 \leq x \leq 1.5$ is discretized using 100 cells, where open boundary conditions are considered for the left and right boundaries. The initial values $p = 50$, $n = 1$, $\vec{u} = \vec{E} = \vec{0}$ and $B^x = B^z = 0$, are considered, and the initial B^y is computed using Eq. (4.55) at $t = 1$ with $B_0 = 1$. In the numerical model $\Gamma = 4/3$, $\delta_x/\delta t = \sqrt{2}$, $\tau = 1$ and $\alpha = 0.1$ are considered. The simulation runs until $t = 8$ and the results are compared to the analytical results at $t = 9$ (since the initial condition is assumed to be at $t = 1$). Two values of uniform conductivity, $\sigma = 100$ and $\sigma = 50$, are considered and the results of the comparison with the analytical solution for both cases along with the initial conditions are presented in Fig. 4.4. One can see that the numerical and analytical results are almost indistinguishable and that the current sheet in a domain with $\sigma = 50$ diffuses faster than the domain with $\sigma = 100$ due to the higher resistivity. This test validates the resistive part of the numerical model and shows the capability of the model for simulating resistive problems far from the ideal MHD limit.

To check the convergence of the model, we implement the same current sheet simulation with $\sigma = 100$ for different grid resolutions. Fig. 4.5 reports the error versus the number of cells in a log-log plot, and the slope of the fitted line (blue solid line) shows that the model is nearly second order as we expect

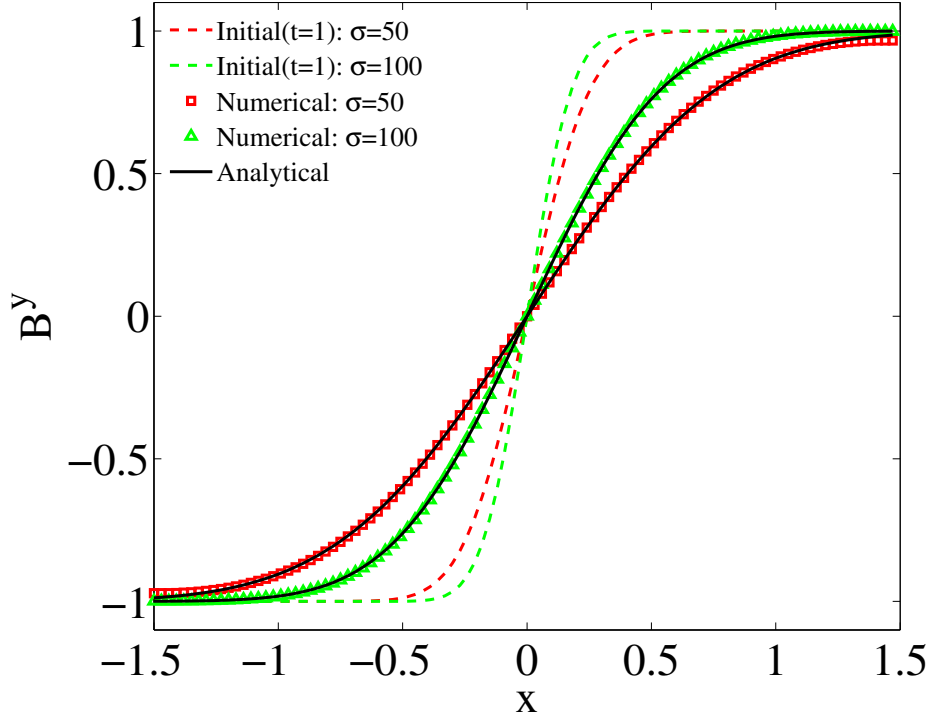


Fig. 4.4: Results of the numerical test for the evolution of a current sheet in the resistive regime. The test is performed for two values of the conductivity, i.e. $\sigma = 100$ and $\sigma = 50$. Dashed lines show the initial condition of the current sheet, which corresponds to the analytical solution, Eq. (4.55), at $t = 1$. The symbols show the result of the numerical solution at $t = 9$, and solid black lines show the exact analytical solution at this time.

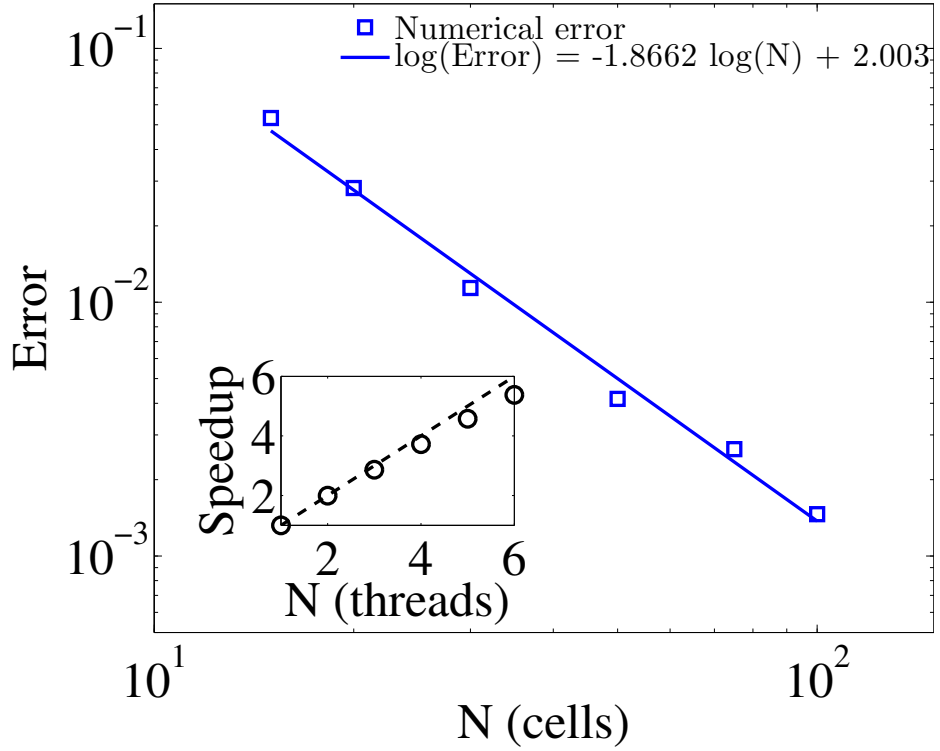


Fig. 4.5: Results of the convergence test for the simulation of the evolution of a current sheet in the resistive regime with $\sigma = 100$ in a log-log plot. Symbols show the numerical error and the solid blue line is the fitted line with slope -1.8662 , which shows a nearly second order convergence. In the inset the speedup obtained by using the openMP parallelizing method is reported versus the number of threads. The dashed line shows the ideal speedup.

for a lattice Boltzmann scheme. The error is calculated by the relation

$$E_N = \left(\frac{1}{N} \sum_{i=1}^N (B_{\text{num}}^y - B_{\text{anal}}^y)^2 \right)^{1/2}, \quad (4.56)$$

with N being the number of the cells, B_{num}^y and B_{anal}^y the numerical and analytical results, respectively. Additionally, as explained in the introduction, one of the advantages of using lattice Boltzmann methods is its simplicity and efficiency on parallel computers. To show that this also holds for our model, we use a simple openMP parallelizing method and simulate the 3D extension of the aforementioned current sheet problem with $150 \times 150 \times 150$ cells and $\sigma = 100$, until 5 time steps. The preliminary resulting speedup for a few number of threads is shown in the inset of Fig. 4.5, where one can see that even for a straight forward parallelizing method, a satisfactory level of efficiency is achieved. However, for a thorough study of the parallelizing efficiency, a much larger number of threads and more advanced parallelizing methods should be experimented.

4.4.3 Magnetic reconnection driven by Kelvin-Helmholtz instability

After validating the numerical model, we now study the magnetic reconnection process driven by the Kelvin-Helmholtz (KH) instability. As mentioned before, the magnetic reconnection is a process where magnetic lines change their topology. At the place where the magnetic lines reconnect, usually a null point forms where the magnetic field vanishes. There are several theoretical descriptions for the magnetic reconnection including the well known Sweet-Parker [113, 93] and Petschek [94] models.

The Sweet-Parker model is based on the discussion of pressure balance in the reconnection region, where the reconnection region is assumed to be dominated by diffusion while the outside region is assumed to be ideal. Due to the magnetic diffusion, the plasma is driven into the current sheet (inflow) with velocity v_{in} in the direction perpendicular to the length of the current sheet. The conversion of magnetic energy within the current sheet thrusts

the plasma out with the velocity v_{out} in the direction of the length of the current sheet. It is shown that the reconnection rate R , which is defined as the ratio between v_{in} and v_{out} is proportional to $S^{-\frac{1}{2}}$, where $S = \mu_o L v_A \sigma$ is the Lundquist number (magnetic Reynolds number), with L as characteristic length. The reconnection rate in this model is usually small due to the high aspect ratio of the reconnection region (which is proportional to the inflow and outflow velocities assuming the incompressibility condition).

In the Petschek model, it is assumed that the magnetic energy can be liberated not only in the current sheet but also as pairs of slow shocks which stem from the edge of the sheet. Therefore, the reconnection region can be smaller than the one for the Sweet-Parker model, which can lead to higher reconnection rate. In this model R is proportional to $(\ln S)^{-1}$.

As discussed, magnetic reconnection is believed to have prominent effects in many high energy astrophysical events and therefore it should be strongly influenced by relativistic effects. Although the mechanism of relativistic reconnection is not well understood, recent theoretical and numerical studies of the relativistic Sweet-Parker and Petschek models show the same proportionality relation between R and S [65, 115]. In the numerical simulations, it is important how one triggers the reconnection process. If a local increase in the conductivity is used to trigger the reconnection, Petschek type reconnection is observed with “x-type” null point, while when a perturbation in the magnetic potential is applied, Sweet-Parker type reconnection is observed with “y-type” null point [128]. This is similar to the non-relativistic numerical results. Here instead of using either of the mentioned ways, we use a hydrodynamic instability to trigger the reconnection. In particular, the KH instability is chosen because of its wide range of applications in astrophysical events as discussed in Ch. 1. Therefore, two dimensional simulations of the KH instability in a Harris like current sheet are performed for different values of shear velocity, density ratio and conductivity. A domain of $-0.5 \leq x \leq 0.5$ by $-0.5 \leq y \leq 0.5$ is discretized using 512×512 cells. The following initial conditions are considered:

$$u_x = \frac{U_0}{2} \tanh\left(\frac{y}{a}\right), \quad n = n_0 + \frac{\Delta n}{2} \tanh\left(\frac{y}{a}\right), \quad (4.57)$$

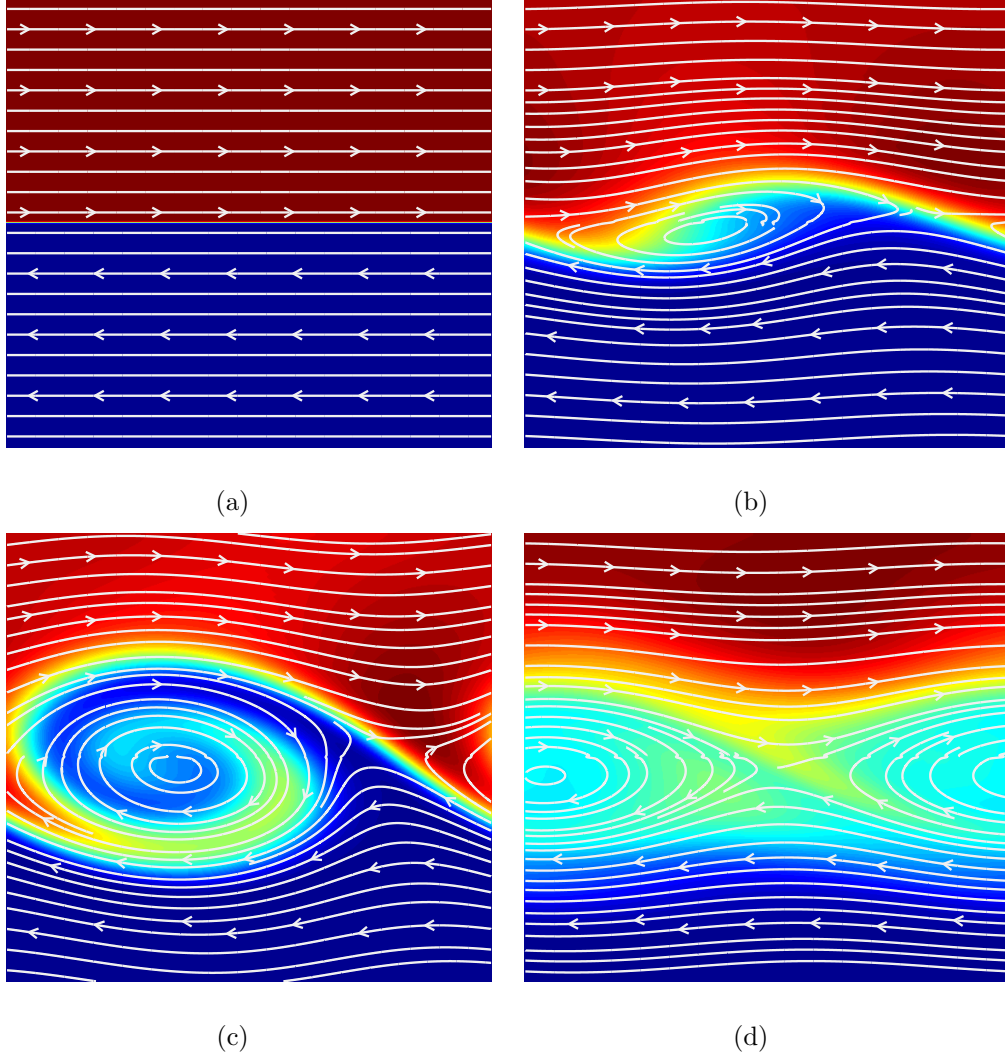


Fig. 4.6: Snapshots of the density for the KH instability at times (a) $t = 0.0$ (initial condition) (b) $t = 3.31$ (c) $t = 6.62$ (d) $t = 15.47$, for the case with $\sigma = 100$, $\Delta n = 1.8$, $U_0 = 0.6c$, where the color red to blue denotes high to low values, respectively. The white lines show the magnetic field lines.

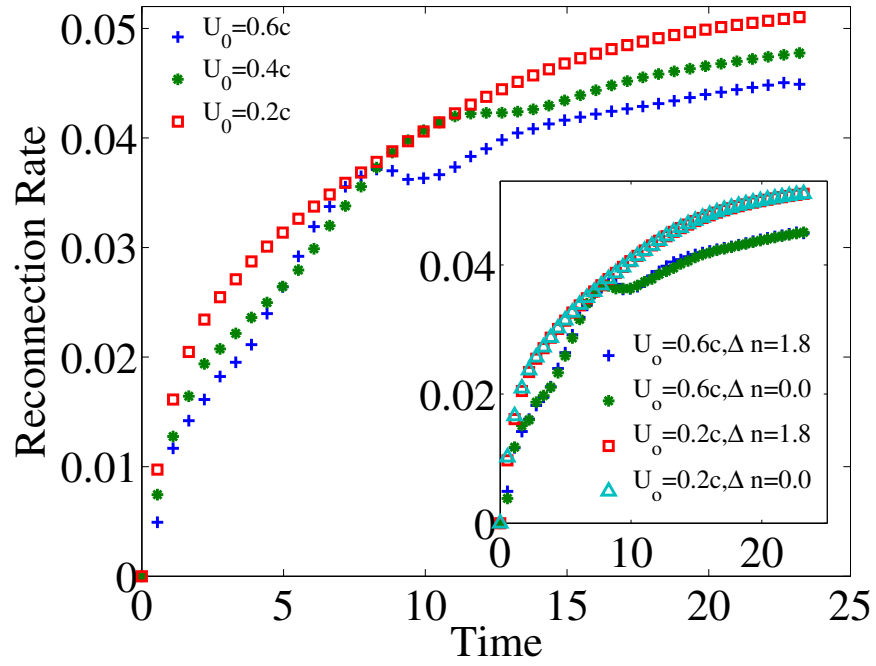


Fig. 4.7: Reconnection rate versus time for the case $\sigma = 100$, $\Delta n = 1.8$ for different values of U_0 . In the inset the results are shown for two different values of $\Delta n = 1.8$ and $\Delta n = 0$ for $\sigma = 100$.

where U_0 defines the shear velocity, $\Delta n = (n_{\text{up}} - n_{\text{down}})$ is the density difference between the upper ($y > 0$) and lower ($y < 0$) part of the domain, $n_0 = 1$, $p = 1$ and $a = \delta x$ is considered. Furthermore,

$$B^x = B_0 \tanh\left(\frac{y}{a}\right), \quad (4.58)$$

while $B^y = B^z = 0$ and $B_0 = 0.06$ is considered. The KH instability is triggered by a perturbation in the velocity in y -direction, namely

$$u_y = u_{\text{pert}} \sin(kx) \exp\left(-\frac{y^2}{b^2}\right), \quad (4.59)$$

with $u_{\text{pert}} = 0.01$ as the perturbation amplitude, $k = 2\pi$ for a single mode perturbation, and $b = 10\delta x$. For the left and right boundaries ($x = \pm 0.5$) periodic boundary conditions are considered while for the upper and lower boundaries ($y = \pm 0.5$) open boundary conditions are implemented. The simulation is performed for different values of $U_0 = 0.6c, 0.4c, 0.2c$ and $\sigma = 100, 80, 60, 40, 20$ for two values of $\Delta n = 0, 1.8$ and $\Delta n = 0$ where the latter corresponds to the case with initial uniform density. For the numerical simulation $\Gamma = 4/3$, $\delta x/\delta t = 2.5\sqrt{2}$, $\tau = 1$ and $\alpha = 0.1$ are considered. The initial electric field can be simply computed using Faraday's law (dropping the time derivative term because of the stationary state) and Ohm's law, knowing the fact that the initial velocity and magnetic fields are in the same plane. Additionally, for the open boundary condition, and to ensure the divergence free condition of the magnetic field, the normal component of the magnetic field is adjusted in order to have $\vec{\nabla} \cdot \vec{B} = 0$ at the boundaries.

The snapshots of the density for the case with $\sigma = 100$, $\Delta n = 1.8$ and $U_0 = 0.6c$ are presented in Fig. 4.6 for different time steps. One can see the evolution of the instability in time where after an initial linear growth, a nonlinear stage takes place which leads to the penetration and mixing of the lighter and heavier fluids, where the characteristic structure of the KH instability forms. The reconnection is triggered by the instability and occurs in the initial current sheet, where the magnetic field changes sign. As the instability evolves, the location of the reconnection null point changes. Since no external force is implemented, the instability finally smoothens out due to the dissipation in the system.

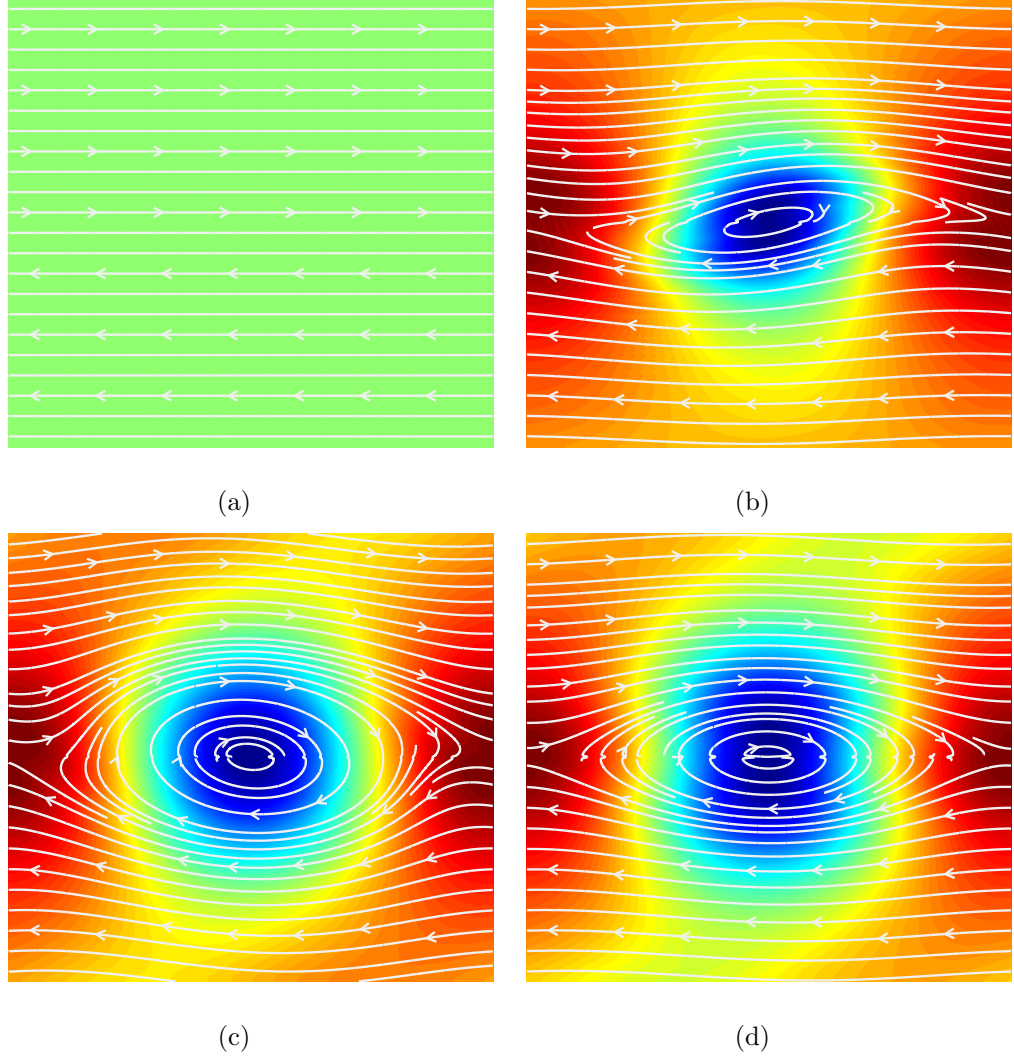


Fig. 4.8: Snapshots of the density for the KH instability at times (a) $t = 0.0$ (initial condition) (b) $t = 3.31$ (c) $t = 6.62$ (d) $t = 15.47$, for the case with $\sigma = 100$, $\Delta n = 0$, $U_0 = 0.6c$, where the color red and blue denotes high and low values, respectively. The white lines show the magnetic field lines.

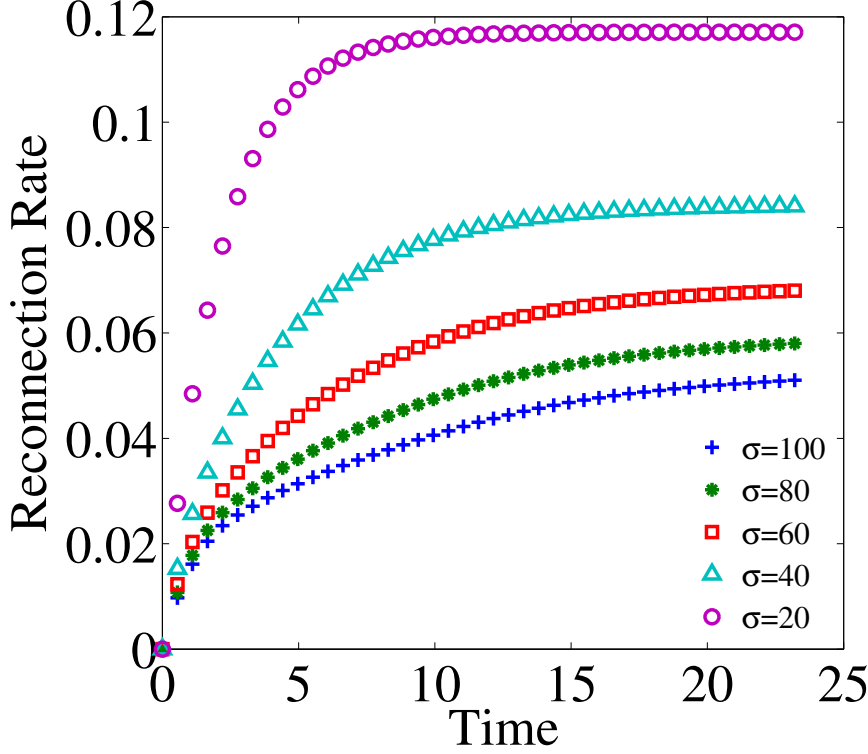


Fig. 4.9: Reconnection rate versus time for the case $\Delta n = 1.8$ and $U_0 = 0.2c$ for different values of σ .

We are interested in the reconnection rates of the considered cases. Since the initial condition is not in the rest frame, it is not practical to find the reconnection rate based on the definition mentioned before (ratio between inflow and outflow velocities). Instead we use [127]

$$R(t) = \left(\frac{\Delta E^z}{B_0} \right)_{\text{null}}, \quad (4.60)$$

i.e., the generated out-of-plane component of the electric field ($\Delta E^z = E^z - E_0^z$, E_0^z being the initial out-of-plane electric field) normalized by B_0 at the null point, which shows the rate at which the magnetic flux is convected to this point (see Ref. [53]). Here we investigate the effects of different parameters on the reconnection rate. First we study the effects of the parameters related to the KH instability, namely U_0 and Δn . Fig. 4.7 shows the results

for the reconnection rate versus time for different values of U_0 , when $\sigma = 100$ and $\Delta n = 1.8$. It is shown that an increase in the magnitude of the shear velocity reduces the reconnection rate. This is due to the stabilizing effects of the shearing velocity on the tearing instability [17], an MHD instability that appears in connection with sheared magnetic field. Also note that the bumps that appear in the reconnection rate at high shear velocities is due to the transition of the instability into its stationary state, where one can appreciate that, for higher shear velocities, this transition occurs at earlier times.

Additionally, in the inset of Fig. 4.7, for the case with $\sigma = 100$, the effects of different values of Δn is shown. One can notice that changing the value of Δn from 1.8 to 0 (initially uniform density) has negligible effects on the reconnection rate, for different magnitudes of the shear velocity. This is despite the fact that the hydrodynamics of the system for the initially uniform density is quite different from the case with inhomogeneous densities. Fig. 4.8 shows the snapshots of the density for the case $\Delta n = 0$, $\sigma = 100$ and $U_0 = 0.6c$, where the well known “cat’s eye” structure of KH instability for the case with initially uniform density can be recognised. Comparison between Fig. 4.6 and Fig. 4.8 shows that, for the case with the initially uniform density, the results are symmetric and because of the form of the initial perturbation, the location of the null point is always at the boundary, unlike the previous case, where the location of the null point changes with time.

Another parameter that we are interested in studying is the conductivity σ . Fig. 4.9 shows the results of the reconnection rate versus time for the case with $U_0 = 0.2c$ and $\Delta n = 1.8$ for different values of the conductivity. As shown, the reconnection rate increases faster in time and reaches a higher value for lower conductivities (higher resistivity). The fact that the reconnection rate increases by increasing the resistivity is also expressed in the models of Sweet-Parker and Petschek. The interesting point is to inspect the exact relation between the reconnection rate and the resistivity. As mentioned before, in the Sweet-Parker model, R is proportional to $\sigma^{-\frac{1}{2}}$ (assuming constant Alfvén velocity) and in the Petschek model R is proportional to $(\ln \sigma)^{-1}$. To compute this proportionality relation for our results,

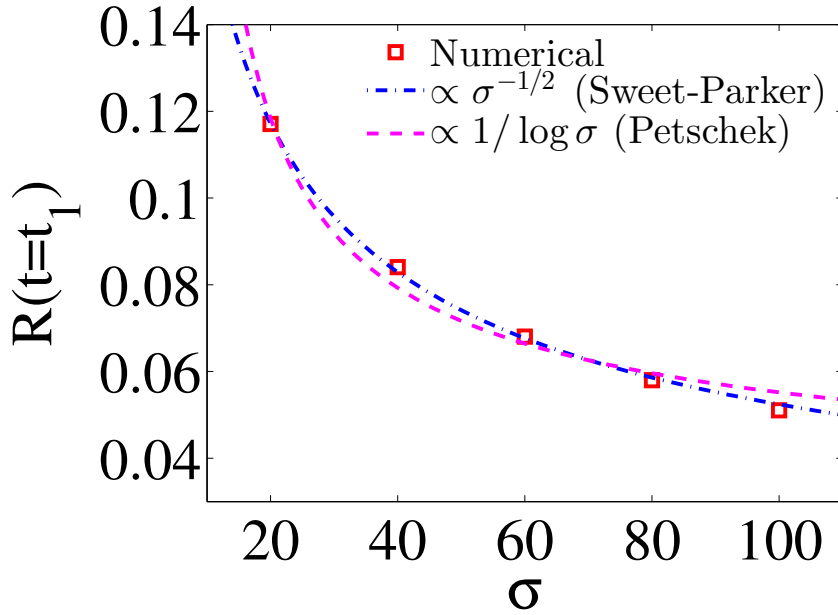


Fig. 4.10: $R(t)$ at time $t = 23.2$ for different values of σ based on the numerical results (red symbols). Best fitting curves using the proportionality relation for the Sweet-Parker (dashed-dotted blue) and Petschek (dashed red) models are shown.

the reconnection rates $R(t = t_1)$ at the final time $t_1 = 23.2$ are used. The results are shown in Fig. 4.10, where, as expected, R_0 decreases with increasing σ . The blue dashed line, and the red dashed-dotted line in Fig. 4.10 are the best fitting curves for the data using the proportionality relations suggested by Sweet-Parker and Petschek models, respectively. One can see that the results clearly do not follow the Petschek scaling law while match the Sweet-Parker scaling law very closely.

4.4.4 Three-dimensional magnetic reconnection in a stellar flare

In this section, we show the results of the 3D numerical simulation of magnetic reconnection in a stellar flare, which is driven by a shear velocity on its photosphere. Thus, a domain of $-3 \leq x \leq 3$ by $-3 \leq y \leq 3$ by $0 \leq z \leq 6$ is

discretized by $256 \times 256 \times 256$ cells. The configuration of the initial condition is chosen to mimic the arcade and the flux rope of a stellar flare [16]. The total potential field is defined as

$$\psi = \psi_b + \psi_l + \psi_i. \quad (4.61)$$

This configuration consists of a background magnetic field that is produced by four line currents (just below the photosphere), which determines ψ_b and an image current (below the photosphere), which determines ψ_i . This background magnetic field yields a null point above the photosphere. Additionally, a line current contained within the flux rope with finite radius, which determines ψ_l , is added to the null point. Note that if we do not consider the flux rope, the magnetic field configuration is a potential quadrupole field.

The potential fields generated by these currents are defined as follows:

$$\psi_b = c_b \log \frac{[(x + 0.3)^2 + (z + 0.3)^2][(x - 0.3)^2 + (z + 0.3)^2]}{[(x + 1.5)^2 + (z + 0.3)^2][(x - 1.5)^2 + (z + 0.3)^2]}, \quad (4.62)$$

$$\psi_i = -\frac{r_0}{2} \log [x^2 + (z + h)^2], \quad (4.63)$$

$$\psi_l = \begin{cases} \frac{r^2}{2r_0}, & r \leq r_0, \\ \frac{r_0}{2} - r_0 \log r_0 + r_0 \log r, & r > r_0, \end{cases} \quad (4.64)$$

where $r = [x^2 + (z - h)^2]^{1/2}$ is the distance from the center of the flux rope, h is the height of the flux rope, which is set to 2.0, r_0 is the radius of the flux rope, which is set to 0.5, and $(\pm 1.5, -0.3)$ and $(\pm 0.3, -0.3)$ are the (x, z) positions of the four line currents. Here, c_b represents the strength of the background magnetic field, which is set to 0.2534 [16]. The resulting magnetic field is calculated by taking the curl of the total potential field, i.e., $\vec{B}^* = \vec{\nabla} \times \psi \hat{e}_y$, and in order to adjust the magnitude of the magnetic field, each component of the magnetic field is multiplied by (B_0/B_{\max}^*) , where B_{\max}^* is the maximum of the computed magnetic field in the domain and $B_0 = 0.06$ is considered. To satisfy the force balance inside the flux rope, a magnetic component should be added in the direction perpendicular to the magnetic

field, i.e., y -direction, which has the following form:

$$B^y = \begin{cases} (B_0/B_{\max}^*)\sqrt{2\left(1 - \frac{r^2}{r_0^2}\right)}, & r \leq r_0, \\ 0, & r > r_0. \end{cases} \quad (4.65)$$

The initial velocity is set to zero, and the initial density and pressure are considered to be uniform and equal to 1.0 everywhere in the domain. In order to compute the initial values for the electric field and current density, the numerical code is used in an iterative process, fixing the value of magnetic field and velocity at each time-step. Open boundary conditions are considered for all the boundaries, and as mentioned before, the normal component of the magnetic field is adjusted on each boundary to satisfy the divergence free condition of the magnetic field.

To set-up a shear velocity in the photosphere, two adjacent vortices rotating in the same direction are produced by applying proper external forces. Therefore, an external force is applied to both sub-domains of $-3 \leq x < 0$ by $-3 \leq y \leq 3$ by $0 \leq z \leq 0.2343$ as well as $0 \leq x \leq 3$ by $-3 \leq y \leq 3$ by $0 \leq z \leq 0.2343$, with the following form:

$$F^x = F_0 \sin(\pi x^*/(3)) \cos(\pi y/6), \quad (4.66)$$

$$F^y = F_0 \cos(\pi x^*/(3)) \sin(\pi y/6), \quad (4.67)$$

where F^x and F^y are the components of the external force in the x and y directions, respectively, F_0 is the magnitude of the applied force, which is set to 0.05 and $x^* = x$ for the sub-domain $-3 \leq x < 0$ and $x^* = x - 3$ for the sub-domain $0 \leq x \leq 3$. Note that, to limit the magnitude of the velocity, the external force is non-zero only when the maximum velocity in the domain is smaller than $0.3c$. For the numerical simulation $\sigma = 100$, $\Gamma = 4/3$, $\delta x/\delta t = 2.5\sqrt{2}$, $\tau = 1.0$ and $\alpha = 0.1$ are considered.

The results of the 3D simulation are shown in Fig. 4.11. One can see the initial condition of the magnetic field lines in Fig. 4.11(a). The colors on the outer domain boundaries indicate the value of the vorticity, which is zero

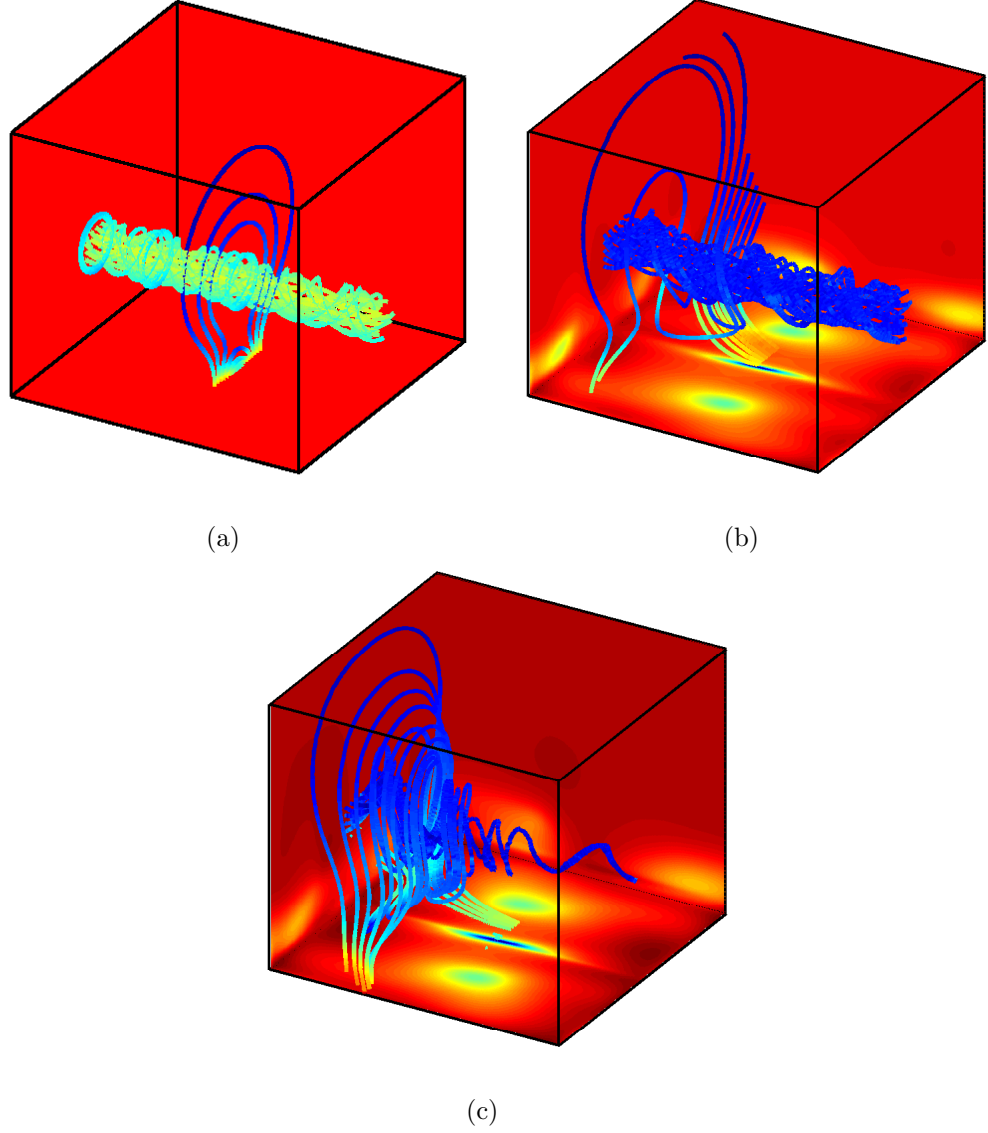


Fig. 4.11: Snapshots of the 3D magnetic reconnection in a stellar flare due to the shear flow at times (a) $t = 0$ (initial condition), (b) $t = 19.86$ and (c) $t = 43.02$. The colors of the magnetic lines show the magnitude of the magnetic field, where blue to red show low to high values. On the outer boundary surfaces of the domain the colors indicate the value of the vorticity, where red and blue denote negative and positive vorticity, respectively.

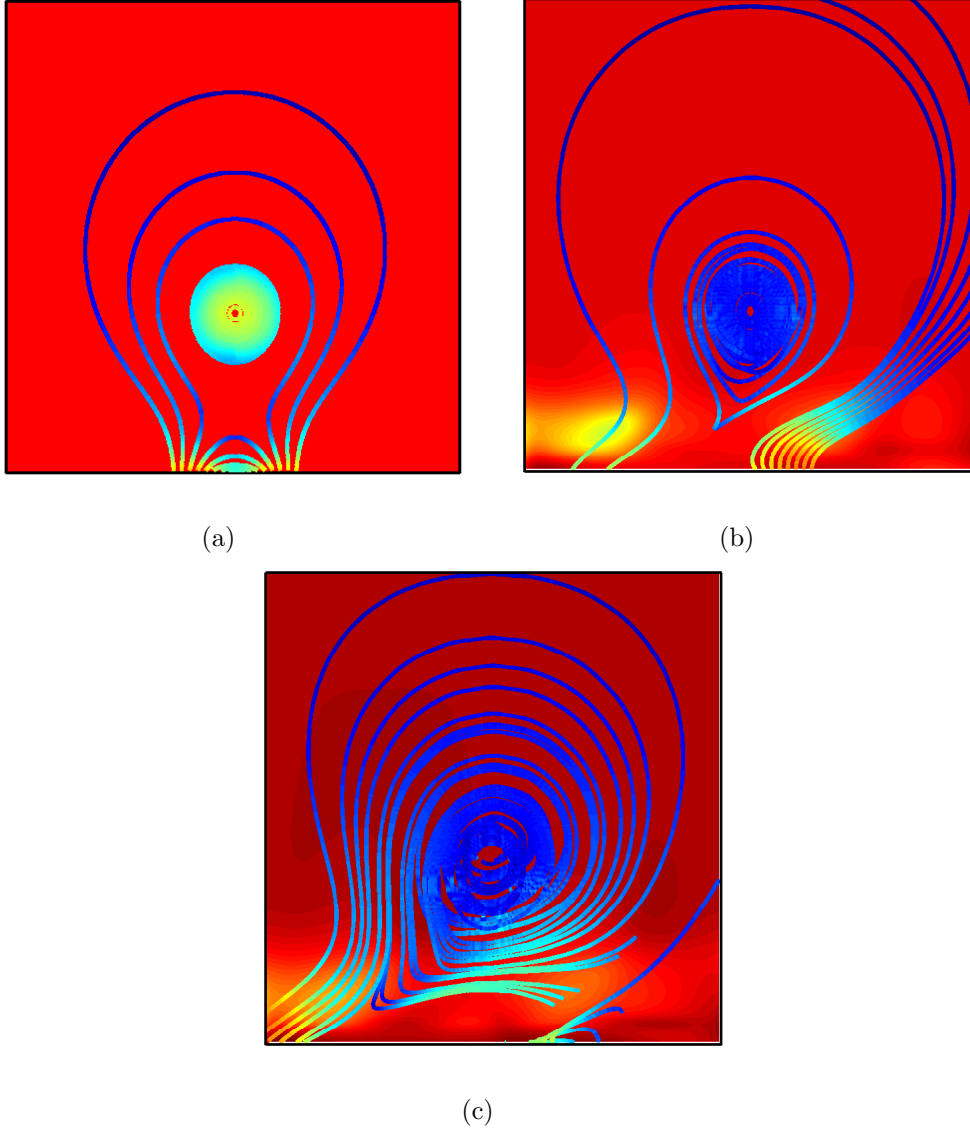


Fig. 4.12: Projection of the results presented in Fig. 4.11 onto the xz plane. Times and colors are the same as Fig. 4.11.

everywhere in the beginning. After applying the external force, two vortices form, which rotate in the same direction and therefore give rise to a shear velocity in the middle of the xy plane, i.e, the photosphere plane. This shear velocity finally results in a “cat’s eye” structure in the photosphere (see Fig. 4.11(c)) similar to the results of the 2D KH instability with uniform initial density in Fig. 4.8. The shear velocity starts to twist the foot of the background magnetic lines and later the upper parts of the background magnetic lines. As a result at some point, the twisted background magnetic lines and the flux rope magnetic lines take opposite directions. This is where the current sheet forms and the reconnection between these two sets of magnetic lines takes place (see Fig. 4.11(b)). At late times, Fig. 4.11(c), most of the flux rope magnetic lines reconnect with the background magnetic lines, and only a small part of the flux rope can reach the opposite surface. This process can be appreciated more clearly in the 2D projections on the xz plane, which are provided in Fig. 4.12. For instance, a starting configuration of the reconnection can be observed in Fig. 4.12(b), where one can see that the background magnetic lines reconnect to the flux rope lines and change their topology.

4.5 Summary

In this chapter, we have developed a relativistic MHD lattice Boltzmann model, capable of dealing with problems in the resistive and ideal regimes. The model is based on the relativistic LB model described in Chs. 2 and 3, to solve the hydrodynamics equations, and the model proposed in Ref. [78] to solve the Maxwell equations, where several modifications and extensions are implemented to couple the models and to use them in the relativistic MHD context. Thus, a D3Q19 lattice configuration is used for the hydrodynamic part and a D3Q13 lattice for the electromagnetic part.

The numerical method is validated for test simulations in two different regimes, namely propagation of an Alfvén wave in the ideal MHD limit (high conductivity), and evolution of a current sheet in a resistive regime (low con-

ductivity). The results are compared with the analytical ones and very good agreement is observed. Additionally, the magnetic reconnection driven by the relativistic KH instability is studied in detail and the effect of different parameters on the reconnection rate is investigated. It is concluded that, while the density ratio has negligible effects on the reconnection rate, an increase in the value of the shear velocity will decrease the reconnection rate. We have also found that, the reconnection rate is proportional to $\sigma^{-\frac{1}{2}}$, which agrees with the scaling law of Sweet-Parker model. Finally, we have presented the results of 3D simulation of the magnetic reconnection in a stellar flare, which is driven by shear velocity in the photosphere. We have shown that due to the shear velocity the reconnection happens between flux rope and background magnetic field lines.

It is worth mentioning that, as mentioned, the relativistic lattice Boltzmann models show nearly an order of magnitude faster performance than the corresponding hydrodynamic codes. Furthermore, the lattice Boltzmann model to solve the Maxwell equations also turns out to be very efficient, almost an order of magnitude faster than Yee's original FDTD method [78]. Thus, we expect our model to have a competitive performance comparing with current models for resistive relativistic MHD.

Chapter 5

Discussion and Outlook

In this work, we developed lattice Boltzmann models for relativistic hydrodynamics and magnetohydrodynamics. First, we proposed a lattice Boltzmann model, which is able to solve the relativistic hydrodynamics equations and is numerically stable for ultra-high velocities. We provided a detailed discussion of the construction of the equilibrium distribution function, emphasizing the common aspects with the standard lattice Boltzmann theory. For the construction of the distribution functions, we expanded the Maxwell Jüttner distribution in orthogonal polynomials, using the equilibrium distribution at the local rest frame as weight function. A discretization procedure applied to adjust the expansion to the D3Q19 cell configuration. We used a flux limiter scheme and introduced a bulk viscosity term into the Boltzmann equation, to increase the numerical stability at high velocities. We showed that the model is capable of simulating low viscous flows which is very promising for many astrophysical applications. Moreover, the model preserved the numerical stability for the simulation of the Riemann problem at ultra-high relativistic flows ($\gamma \sim 10$). As an example of relativistic hydrodynamics with non-trivial geometries, we also applied our scheme to an astrophysical system, namely the collision of a shock wave, produced by a supernova explosion, against a massive interstellar cloud in weakly and highly relativistic regimes, for both nearly-inviscid and viscous cases.

Several issues remain open for future research. Extensions of this model to include higher order lattices so as to recover more moments of the equilibrium

distribution, is one of them. Recently, for the case with negligible rest mass energy, a lattice Boltzmann model to reproduce up to the third order moment of the equilibrium distribution is derived in Ref. [76]. The model is based on a single distribution function and the lattice configuration is chosen such that the lattice points belong to the surface of a sphere. The model can reproduce the right velocity and pressure profiles for the Riemann problem in quark-gluon plasmas, for large values of η/s . However, to recover the third moment, and to provide enough symmetry, rather high number of velocity vectors (128) are required.

Additionally, the current relativistic LB deals with special relativistic flows and it is very desirable to develop a general relativistic lattice Boltzmann model. A non-relativistic LB on a constant space-curved background (campyloctic flow) was constructed recently in Ref. [75] to simulate fluid dynamics in general non-cartesian manifolds. Considering that we have already constructed the LB model for solving the energy-momentum equation of the relativistic fluid dynamics in flat time-space, in principle, these models could be extended/coupled to solve the general relativistic fluid dynamics. However, in general this task seems to involve a number of genuinely new challenges [111].

Another important question concerns the existence of a relativistic lattice H-theorem. Apart from the theoretical interest on its own, this could have major implications on the numerical stability of the scheme at high Reynolds number, i.e. for the simulation of relativistic turbulence [59].

Furthermore, we studied the relativistic Richtmyer-Meshkov instability and we showed that relativistic effects weaken the instability. Linear stability analysis was used to provide an asymptotic relation for the amplitude growth rate of the interface in the linear regime and based on the numerical results we also proposed a relation for the evolution of the interface amplitude in the nonlinear regime. Additionally, we investigated the thermal behaviour of the RM instability which results from Mach cone interactions in a relativistic fluid and we found that RM instability is responsible for the decrease in the average temperature of the media which was confirmed by considering shock tube RM instability. We also suggested an experimental tool to identify the

interaction of Mach cones using the two particle correlation function.

For the study of the relativistic RM instability, the numerical model is extended to include the ideal gas EoS as well as external forcing term.

The development of new theoretical analysis of relativistic RM instability for nonlinear regimes and including the compressibility effects, make interesting subjects for further research. In the numerical context, another interesting research direction is the simulation of relativistic flows with a non-ideal equations of state, which may find many applications in relativistic cosmology and high-energy theories of the early universe [99, 18].

Furthermore, we developed an LB model for relativistic magnetohydrodynamics. The numerical method was validated for test simulations in the ideal and resistive regimes. Additionally, the model was used to study the relativistic magnetic reconnection in different systems, namely 2D magnetic reconnection driven by the relativistic KH instability and 3D magnetic reconnection in a stellar flare, which is driven by shear velocity in the photosphere. For the 2D case, the effect of different parameters on the reconnection rate was studied in detail and it was found that the reconnection rate follows the scaling law of Sweet-Parker model.

It is known that due to the increased complexity of the topology in 3D magnetic reconnection, the reconnection rate for the general case of 3D is not as straight forward as in the case of 2D [48]. Therefore, studying the reconnection rate for the 3D simulation of magnetic reconnection, for instance, in stellar flares, seems to be a very interesting and challenging topic for further research.

Concerning the numerical aspects of the LB model for relativistic MHD, a more detailed study of the parallelizing efficiency using a more advanced parallelizing methods is an interesting topic for future research. Also, improving the numerical stability of the method to deal with higher values of the magnetic fields is very desirable.

These are just but a few of the many exciting developments and applications which may currently be envisaged for the lattice Boltzmann equation for relativistic hydrodynamics and magnetohydrodynamics presented in this work.

References

- [1] J.L. Anderson and H.R. Witting. A relativistic relaxation-time model for the Boltzmann equation. *Physica*, 74(3):466 – 488, 1974.
- [2] R. Antonucci. Unified models for active galactic nuclei and quasars. *Annu. Rev. Astron. Astrophys.*, 31:473–521, 1993.
- [3] D. Arnett. The role of mixing in astrophysics. *Astrophys. J. Supp. Ser.*, 127(2):213, 2000.
- [4] R. Benzi, S. Succi, and M. Vergassola. The lattice Boltzmann equation: theory and applications. *Phys. Rep.*, 222(3):145 – 197, 1992.
- [5] B. Betz. *Jet Propagation and Mach-Cone Formation in (3+1)-dimensional Ideal Hydrodynamics*. diploma thesis, Johann Wolfgang Goethe-University, 2009.
- [6] B. Betz, J. Noronha, G. Torrieri, M. Gyulassy, and D.H. Rischke. Universal flow-driven conical emission in ultrarelativistic heavy-ion collisions. *Phys. Rev. Lett.*, 105:222301, 2010.
- [7] P.L. Bhatnagar, E.P. Gross, and M. Krook. A model for collision processes in gases: I. small amplitude processes in charged and neutral one-component systems. *Phys. Rev.*, 94:511–525, 1954.
- [8] R.D. Blandford and M.J. Rees. A ‘twin-exhaust’ model for double radio sources. *Mon. Not. R. Astron. Soc.*, 169(1):395–415, 1974.

-
- [9] I. Bouras, A. El, O. Fochler, H. Niemi, Z. Xu, and C. Greiner. Transition from ideal to viscous mach cones in a kinetic transport approach. *Phys. Lett. B*, 710(4):641–646, 2012.
- [10] I. Bouras, E. Molnar, H. Niemi, Z. Xu, A. El, O. Fochler, C. Greiner, and D.H. Rischke. Relativistic shock waves in viscous gluon matter. *Phys. Rev. Lett.*, 103(3):032301, 2009.
- [11] M. Brouillette. The Richtmyer-Meshkov instability. *Annu. Rev. Fluid Mech.*, 34(1):445–468, 2002.
- [12] N.F. Camus, S.S. Komissarov, N. Bucciantini, and P.A. Hughes. Observations of wisps in magnetohydrodynamic simulations of the Crab Nebula. *Mon. Not. R. Astron. Soc.*, 400(3):1241–1246, 2009.
- [13] P. Carlès and S. Popinet. The effect of viscosity, surface tension and non-linearity on Richtmyer-Meshkov instability. *Eur. J. Mech. B-Fluid*, 21(5):511–526, 2002.
- [14] C. Cercignani and G.M. Kremer. *The Relativistic Boltzmann Equation: Theory and Applications*. Birkhauser, Boston; Basel; Berlin, 2002.
- [15] H. Chen, S. Chen, and W.H. Matthaeus. Recovery of the Navier-Stokes equations using a lattice-gas Boltzmann method. *Phys. Rev. A*, 45(8):5339–5342, 1992.
- [16] P.F. Chen and K. Shibata. An emerging flux trigger mechanism for coronal mass ejections. *Astrophys. J.*, 545(1):524, 2000.
- [17] Q. Chen, A. Otto, and L.C. Lee. Tearing instability, Kelvin-Helmholtz instability, and magnetic reconnection. *J. Geophys. Res. A: Space Phys.*, 102(A1):151–161, 1997.
- [18] M. Cheng, N.H. Christ, S. Datta, J. van der Heide, C. Jung, F. Karsch, O. Kaczmarek, E. Laermann, R.D. Mawhinney, C. Miao, P. Petreczky, K. Petrov, C. Schmidt, W. Soeldner, and T. Umeda. QCD equation of

- state with almost physical quark masses. *Phys. Rev. D*, 77(1):014511, 2008.
- [19] B. Chopard and M. Droz. *Cellular Automata*. Springer, 1998.
- [20] B. Chopard, A. Dupuis, A. Masselot, and P. Luthi. Cellular automata and lattice Boltzmann techniques: An approach to model and simulate complex systems. *Adv. Complex Syst.*, 5:103–246, 2002.
- [21] F. Cooper and G. Frye. Single-particle distribution in the hydrodynamic and statistical thermodynamic models of multiparticle production. *Phys. Rev. D*, 10(1):186, 1974.
- [22] D. Cubero, J. Casado-Pascual, J. Dunkel, P. Talkner, and P. Hänggi. Thermal equilibrium and statistical thermometers in special relativity. *Phys. Rev. Lett.*, 99:170601, 2007.
- [23] P.A. Davidson. *An introduction to magnetohydrodynamics*, volume 25. Cambridge university press, 2001.
- [24] P.J. Dellar. Bulk and shear viscosities in lattice Boltzmann equations. *Phys. Rev. E*, 64(3):031203, 2001.
- [25] M.R. Dubal. Numerical simulations of special relativistic, magnetic gas flows. *Comput. Phys. Commun.*, 64(2):221–234, 1991.
- [26] M.D. Duez, Y.T. Liu, S.L. Shapiro, and B.C. Stephens. Relativistic magnetohydrodynamics in dynamical spacetimes: Numerical methods and tests. *Phys. Rev. D*, 72(2):024028, 2005.
- [27] M. Dumbser and O. Zanotti. Very high order $P_N P_M$ schemes on unstructured meshes for the resistive relativistic MHD equations. *J. Comput. Phys.*, 228(18):6991–7006, 2009.
- [28] A.M. Soderberg *et al.* Relativistic ejecta from X-ray flash XRF 060218 and the rate of cosmic explosions. *Nature Letters*, 442:1014, 2006.

-
- [29] A. Adare *et al.* [PHENIX Collaboration]. Dihadron azimuthal correlations in Au+Au collisions at $\sqrt{s_{NN}} = 200$ GeV. *Phys. Rev. C*, 78:014901, 2008.
 - [30] A. Adare *et al.* [PHENIX Collaboration]. Suppression pattern of neutral pions at high transverse momentum in Au+Au collisions at $\sqrt{s_{NN}} = 200$ GeV and constraints on medium transport coefficients. *Phys. Rev. Lett.*, 101:232301, 2008.
 - [31] N.N. Ajitanand *et al.* [PHENIX Collaboration]. Extraction of jet topology using three particle correlations. *Nucl. Phys. A*, 783:519, 2007.
 - [32] F. Wang *et al.* [STAR Collaboration]. Measurement of jet modification at RHIC. *J. Phys. G*, 30:S1299, 2004.
 - [33] J. Adams *et al.* [STAR Collaboration]. Transverse-momentum and collision-energy dependence of high-pT hadron suppression in Au+Au collisions at ultrarelativistic energies. *Phys. Rev. Lett.*, 91:172302, 2003.
 - [34] J. Adams *et al.* [STAR Collaboration]. Distributions of charged hadrons associated with high transverse momentum particles in pp and Au+Au collisions at $\sqrt{s_{NN}} = 200$ GeV. *Phys. Rev. Lett.*, 95:152301, 2005.
 - [35] J.G. Ulery *et al.* [STAR Collaboration]. Two- and three-particle jet correlations from star. *Nucl. Phys. A*, 774:581, 2006.
 - [36] F. Eulerink and G. Mellema. General relativistic hydrodynamics with a ROE solver. *Astron. Astrophys. Suppl.*, 110:110, 1995.
 - [37] J.A. Faber and F.A. Rasio. Binary neutron star mergers. *Living Rev. Relat.*, 15(8), 2012.
 - [38] M. Faganello, F. Califano, F. Pegoraro, T. Andreussi, and S. Benkadda. Magnetic reconnection and Kelvin–Helmholtz instabilities at the earth’s magnetopause. *Plasma Phys. Contr. F.*, 54(12):124037, 2012.
 - [39] H. Falcke and P.L. Biermann. The jet-disk symbiosis: I. Radio to X-ray emission models for quasars. *Astron. Astrophys.*, 293:665–682, 1995.

-
- [40] B.D. Farris, T.K. Li, Y.T. Liu, and S. Shapiro. Relativistic radiation magnetohydrodynamics in dynamical spacetimes: Numerical methods and tests. *Phys. Rev. D*, 78(2):024023, 2008.
- [41] G. Drenkhahn. Acceleration of GRB outflows by Poynting flux dissipation. *Astron. Astrophys.*, 387(2):714–724, 2002.
- [42] T.I. Gombosi, G. Tóth, D.L. De Zeeuw, K.C. Hansen, K. Kabin, and K.G. Powell. Semirelativistic magnetohydrodynamics and physics-based convergence acceleration. *J. Comput. Phys.*, 177(1):176–205, 2002.
- [43] V.N. Goncharov. Theory of the ablative Richtmyer-Meshkov instability. *Phys. Rev. Lett.*, 82(10):2091–2094, 1999.
- [44] H.H. Gutbrod, K.H. Kampert, B. Kolb, A.M. Poskanzer, H.G. Ritter, R. Schicker, and H.R. Schmidt. Squeeze-out of nuclear matter as a function of projectile energy and mass. *Phys. Rev. C*, 42:640–651, 1990.
- [45] H.H. Gutbrod, A.M. Poskanzer, and H.G. Ritter. Plastic ball experiments. *Rep. Prog. Phys.*, 52(10):1267, 1989.
- [46] H. Helmholtz. XLIII. On discontinuous movements of fluids. *Philos. Mag., Ser.4.*, 36(244):337–346, 1868.
- [47] L. Hernquist and N. Katz. TREESPH - A unification of SPH with the hierarchical tree method. *Astrophys. J. Supp. Ser.*, 70:419–446, 1989.
- [48] M. Hesse, T.G. Forbes, and J. Birn. On the relation between reconnected magnetic flux and parallel electric fields in the solar corona. *Astrophys. Journal*, 631(2):1227, 2005.
- [49] F.J. Higuera and J. Jimenez. Boltzmann approach to lattice gas simulations. *Europhys. Lett.*, 9(7):663, 2007.

- [50] D. Hupp, M. Mendoza, I. Bouras, S. Succi, and H.J. Herrmann. Relativistic lattice Boltzmann method for quark-gluon plasma simulations. *Phys. Rev. D*, 84(12):125015, 2011.
- [51] C.H. Jaroschek, H. Lesch, and R.A. Treumann. Relativistic kinetic reconnection as the possible source mechanism for high variability and flat spectra in extragalactic radio sources. *Astrophys. J. Lett.*, 605(1):L9, 2004.
- [52] J.G. Kirk, O. Skjraasen, and Y.A. Gallant. Pulsed radiation from neutron star winds. *Astron. Astrophys.*, 388(2):L29–L32, 2002.
- [53] E.A. Johnson. *Gaussian-Moment Relaxation Closures for Verifiable Numerical Simulation of Fast Magnetic Reconnection in Plasma*. PhD thesis, University of Wisconsin, 2013.
- [54] F. Jüttner. Das maxwellsche gesetz der geschwindigkeitsverteilung in der relativtheorie. *Annalen der Physik*, 339:856–882, 1911.
- [55] W.T. Kelvin. *Mathematical and Physical Papers Vol. 4*. Cambridge University Press, Cambridge, England, 1910.
- [56] R. Keppens, G. Tóth, R.H.J. Westermann, and J.P. Goedbloed. Growth and saturation of the Kelvin-Helmholtz instability with parallel and antiparallel magnetic fields. *J. Plasma Phys.*, 61(01):1–19, 1999.
- [57] S.S. Komissarov. Numerical simulations of relativistic magnetized jets. *Mon. Not. R. Astron. Soc.*, 308(4):1069–1076, 1999.
- [58] S.S. Komissarov. Multidimensional numerical scheme for resistive relativistic magnetohydrodynamics. *Mon. Not. R. Astron. Soc.*, 382(3):995–1004, 2007.
- [59] M.J. Korpi, A. Brandenburg, A. Shukurov, I. Tuominen, and . Nordlund. A supernova-regulated interstellar medium: Simulations of the turbulent multiphase medium. *Astrophys. J. Lett.*, 514(2):L99, 1999.

-
- [60] A.D. Kotelnikov, J. Ray, and N.J. Zabusky. Vortex morphologies on reaccelerated interfaces: Visualization, quantification and modeling of one-and two-mode compressible and incompressible environments. *Phys. Fluids*, 12:3245, 2000.
- [61] L.D. Landau and E.M. Lifshitz. *Fluid Dynamics*. Butterworth-Heinemann, Oxford, 1987.
- [62] Q. Li, Y.L. He, Y. Wang, and W.Q. Tao. Coupled double-distribution-function lattice Boltzmann method for the compressible Navier-Stokes equations. *Phys. Rev. E*, 76(5):056705, 2007.
- [63] A.P. Lobanov and J.A. Zensus. A cosmic double helix in the archetypical quasar 3C273. *Science*, 294(5540):128–131, 2001.
- [64] M. Luzum and P. Romatschke. Conformal relativistic viscous hydrodynamics: Applications to RHIC results at $\sqrt{s_{NN}} = 200$ GeV. *Phys. Rev. C*, 78:034915, 2008.
- [65] Y.E. Lyubarsky. On the relativistic magnetic reconnection. *Mon. Not. R. Astron. Soc.*, 358(1):113–119, 2005.
- [66] A.I. MacFadyen and S.E. Woosley. Collapsars: Gamma-ray bursts and explosions in. *Astrophys. J.*, 524(1):262, 1999.
- [67] C. Marle and C.R. Hebad. Modèle cinétique pour l’établissement des lois de la conduction de la chaleur et de la viscosité en théorie de la relativité. *Seances Acad. Sci.*, 260:6539, 1965.
- [68] Y. Masada, S. Nagataki, K. Shibata, and T. Terasawa. Solar-type magnetic reconnection model for magnetar giant flares. *Publ. Astron. Soc. Japan*, 62(4):1093–1102, 2010.
- [69] A. M. Soderberg *et al.*. A relativistic type Ibc supernova without a detected γ -ray burst. *Nature Letters*, 463:513, 2010.
- [70] C.F. McKee and B.T. Draine. Interstellar shock waves. *Science*, 252:397, 1991.

-
- [71] G.R. McNamara and G. Zanetti. Use of the Boltzmann equation to simulate lattice-gas automata. *Phys. Rev. Lett.*, 61:2332–2335, 1988.
- [72] R. Mei and W. Shyy. On the finite difference-based lattice Boltzmann method in curvilinear coordinates. *J. Comput. Phys.*, 143(2):426–448, 1998.
- [73] M. Mendoza, B. M. Boghosian, H.J. Herrmann, and S. Succi. Derivation of the lattice Boltzmann model for relativistic hydrodynamics. *Phys. Rev. D*, 82(10):105008, 2010.
- [74] M. Mendoza, B. M. Boghosian, H.J. Herrmann, and S. Succi. Fast lattice Boltzmann solver for relativistic hydrodynamics. *Phys. Rev. Lett.*, 105:014502, 2010.
- [75] M. Mendoza, H.J. Herrmann, and S. Succi. Preturbulent regimes in graphene flow. *Phys. Rev. Lett.*, 106(15):156601, 2011.
- [76] M. Mendoza, I. Karlin, S. Succi, and H.J. Herrmann. Relativistic lattice Boltzmann model with improved dissipation. *Phys. Rev. D*, 87:065027, 2013.
- [77] M. Mendoza, I. Karlin, S. Succi, and H.J. Herrmann. Ultrarelativistic transport coefficients in two dimensions. *J. Stat. Mech. Theor. Exp.*, 2013(02):P02036, 2013.
- [78] M. Mendoza and J.D. Muñoz. Three-dimensional lattice Boltzmann model for electrodynamics. *Phys. Rev. E*, 82(5):056708, 2010.
- [79] E.E. Meshkov. Instability of the interface of two gases accelerated by a shock wave. *Fluid Dyn.*, 4(5):101–104, 1969.
- [80] P. Meszaros. Gamma-ray bursts. *Rep. Prog. Phys.*, 69(8):2259, 2006.
- [81] I.F. Mirabel and L.F. Rodríguez. Sources of relativistic jets in the galaxy. *Annu. Rev. Astron. Astrophys.*, 37(1):409–443, 1999.

-
- [82] Y. Mizuno. The role of the equation of state in resistive relativistic magnetohydrodynamics. *Astrophys. J. Suppl. Ser.*, 205(1):7, 2013.
- [83] A. Montakhab, M. Ghodrat, and M. Barati. Statistical thermodynamics of a two-dimensional relativistic gas. *Phys. Rev. E*, 79:031124, 2009.
- [84] M. Müller and S. Sachdev. Collective cyclotron motion of the relativistic plasma in graphene. *Phys. Rev. B*, 78(11):115419, 2008.
- [85] M. Müller, J. Schmalian, and L. Fritz. Graphene: A nearly perfect fluid. *Phys. Rev. Lett.*, 103:025301, 2009.
- [86] B.T. Nadiga. An Euler solver based on locally adaptive discrete velocities. *J. Stat. Phys.*, 81(1):129–146, 1995.
- [87] T.K.M. Nakamura and M. Fujimoto. Magnetic reconnection within MHD-scale Kelvin–Helmholtz vortices triggered by electron inertial effects. *Adv. Space Res.*, 37(3):522–526, 2006.
- [88] K. Nishihara, J.G. Wouchuk, C. Matsuoka, R. Ishizaki, and V.V. Zhakhovsky. Richtmyer–Meshkov instability: theory of linear and non-linear evolution. *Phil. Trans. R. Soc. A*, 368(1916):1769–1807, 2010.
- [89] K.S. Novoselov, A.K. Geim, S.V. Morozov, D. Jiang, M.I. Katsnelson, I.V. Grigorieva, and S.V. Dubonos. Two-dimensional gas of massless dirac fermions in graphene. *Nature Letters*, 438(10):197, 2005.
- [90] K.S. Novoselov, A.K. Geim, S.V. Morozov, D. Jiang, Y. Zhang, S.V. Dubonos, I.V. Grigorieva, and A.A. Firsov. Electric field effect in atomically thin carbon films. *Science*, 306(5696):666–669, 2004.
- [91] C. Palenzuela, L. Lehner, O. Reula, and L. Rezzolla. Beyond ideal MHD: towards a more realistic modelling of relativistic astrophysical plasmas. *Mon. Not. R. Astron. Soc.*, 394(4):1727–1740, 2009.
- [92] X.F. Pan, A. Xu, G. Zhang, and S. Jiang. Lattice Boltzmann approach to high-speed compressible flows. *Int. J. Mod. Phys. C*, 18(11):1747–1764, 2007.

-
- [93] E.N. Parker. Sweet's mechanism for merging magnetic fields in conducting fluids. *J. Geophys. Res.*, 62(4):509–520, 1957.
 - [94] H.E. Petschek. Magnetic field annihilation. Technical report, DTIC Document, 1963.
 - [95] T. Piran. The physics of gamma-ray bursts. *Rev. Mod. Phys.*, 76:1143–1210, 2005.
 - [96] S. Qamar and G. Warnecke. A high-order kinetic flux-splitting method for the relativistic magnetohydrodynamics. *J. Comput. Phys.*, 205(1):182–204, 2005.
 - [97] R.D. Richtmyer. Taylor instability in shock acceleration of compressible fluids. *Commun. Pure Appl. Math.*, 13(2):297–319, 1960.
 - [98] D.H. Rischke, S. Bernard, and J.A. Maruhn. Relativistic hydrodynamics for heavy-ion collisions: I. general aspects and expansion into vacuum. *Nucl. Phys. A*, 595(3):346 – 382, 1995.
 - [99] P. Romatschke. New developments in relativistic viscous hydrodynamics. *Int. J. Mod. Phys. E*, 19(01):1–53, 2010.
 - [100] P. Romatschke, M. Mendoza, and S. Succi. Fully relativistic lattice Boltzmann algorithm. *Phys. Rev. C*, 84:034903, 2011.
 - [101] D. Ryu, I. Chattopadhyay, and E. Choi. Equation of state in numerical relativistic hydrodynamics. *Astrophys. J. Supp. Ser.*, 166(1):410, 2006.
 - [102] L.M. Satarov, H. Stcker, and I.N. Mishustin. Mach shocks induced by partonic jets in expanding quark-gluon plasma. *Phys. Lett. B*, 627(14):64 – 70, 2005.
 - [103] X. Shan and X. He. Discretization of the velocity space in the solution of the Boltzmann equation. *Phys. Rev. Lett.*, 80(1):65–68, 1998.
 - [104] E. Shuryak. Why does the quark–gluon plasma at RHIC behave as a nearly ideal fluid? *Prog. Part. Nucl. Phys.*, 53(1):273–303, 2004.

-
- [105] S. Siegler and H. Riffert. Smoothed particle hydrodynamics simulations of ultrarelativistic shocks with artificial viscosity. *Astrophys. J.*, 531(2):1053, 2008.
- [106] J. Stewart. *Non-equilibrium Relativistic Kinetic Theory*. Springer, Berlin, 1971.
- [107] H. Stoecker. Collective flow signals the quark–gluon plasma. *Nucl. Phys. A*, 750(1):121–147, 2005.
- [108] S. Succi. *The lattice Boltzmann equation for Fluid Dynamics and Beyond*. Oxford University Press, New York, 2001.
- [109] S. Succi. Lattice Boltzmann across scales: from turbulence to DNA translocation. *The European Physical Journal B-Condensed Matter and Complex Systems*, 64(3):471–479, 2008.
- [110] S. Succi and R. Benzi. Lattice Boltzmann equation for quantum mechanics. *Physica D*, 69 3-4:327, 1993.
- [111] S. Succi, M. Mendoza, F. Mohseni, and I. Karlin. Relativistic lattice kinetic theory: Recent developments and future prospects. *Eur. Phys. J. ST*, 223(11):2177–2188, 2014.
- [112] S. Succi, J. Wang, and Y.H. Qian. Clustering instability in granular gases: A mesoscopic investigation. *Int. J. Mod. Phys. C*, 08(04):999–1008, 1997.
- [113] P.A. Sweet. The neutral point theory of solar flares. In *Electromagnetic phenomena in cosmical physics*, volume 6, page 123, 1958.
- [114] J.L. Synge. *The relativistic gas*. North-Holland Amsterdam, 1957.
- [115] H.R. Takahashi, T. Kudoh, Y. Masada, and J. Matsumoto. Scaling law of relativistic Sweet-Parker-type magnetic reconnection. *Astrophys. J. Lett.*, 739(2):L53, 2011.

- [116] M. Takamoto and T. Inoue. A new numerical scheme for resistive relativistic magnetohydrodynamics using method of characteristics. *Astrophys. J.*, 735(2):113, 2011.
- [117] K.W. Thompson. The special relativistic shock tube. *J. Fluid Mech.*, 171(1):365–375, 1986.
- [118] M. Vandenboomgaerde, C. Mügler, and S. Gauthier. Impulsive model for the Richtmyer-Meshkov instability. *Phys. Rev. E*, 58(2):1874, 1998.
- [119] M. Vietri, A. Ferrara, and F. Miniati. The survival of interstellar clouds against Kelvin-Helmholtz instabilities. *Astrophys. J.*, 483(1):262, 1997.
- [120] C.Y. Wang and R.A. Chevalier. Instabilities and clumping in type IA supernova remnants. *Astrophys. J.*, 549(2):1119, 2001.
- [121] L. Wen, A. Panaitescu, and P. Laguna. A shock-patching code for ultrarelativistic fluid flows. *Astrophys. J.*, 486(2):919, 1997.
- [122] D.C. Wilson, C.W. Cranfill, C. Christensen, R.A. Forster, R.R. Peterson, N.M. Hoffman, G.D. Pollak, C.K. Li, F.H. Séguin, J.A. Frenje, et al. Multifluid interpenetration mixing in directly driven inertial confinement fusion capsule implosions. *Phys. Plasmas*, 11:2723, 2004.
- [123] J.G. Wouchuk. Growth rate of the linear Richtmyer-Meshkov instability when a shock is reflected. *Phys. Rev. E*, 63(5):056303, 2001.
- [124] J.G. Wouchuk and K. Nishihara. Linear perturbation growth at a shocked interface. *Phys. Plasmas*, 3:3761, 1996.
- [125] Z. Xu, C. Greiner, and H. Stöcker. Perturbative QCD calculations of elliptic flow and shear viscosity in Au+ Au collisions at $\sqrt{s_{NN}} = 200$ GeV. *Phys. Rev. Lett.*, 101(8):082302, 2008.
- [126] J.Y. Yang, M.H. Chen, I.N. Tsai, and J.W. Chang. A kinetic beam scheme for relativistic gas dynamics. *J. Comput. Phys.*, 136(1):19–40, 1997.

-
- [127] S. Zenitani, M. Hesse, and A. Klimas. Two-fluid magnetohydrodynamic simulations of relativistic magnetic reconnection. *Astrophys. J.*, 696(2):1385, 2009.
- [128] S. Zenitani, M. Hesse, and A. Klimas. Resistive magnetohydrodynamic simulations of relativistic magnetic reconnection. *Astrophys. J. Lett.*, 716(2):L214, 2010.

Curriculum Vitae

Farhang Mohseni, born 03.08.1986

Current address:

Stettbachstrasse 43

8051 Zürich, Switzerland

Education

2012 - 2015	Ph.D. student in Civil Engineering, ETH Zürich, Switzerland
2009 - 2011	Master of Science in Mechanical Engineering (Fluid dynamics & Heat Transfer), University of Tabriz, Iran
2004 - 2009	Bachelor of Science in Mechanical Engineering (Fluid dynamics & Heat Transfer), Shiraz University, Iran
2000 - 2004	Diploma in Mathematics & Physics (High School), Shiraz, Iran

Professional Experience

2012 - 2015	Research Assistant at ETH Zürich, Switzerland: Group of Computational Physics for Engineering Materials, Supervisor: Prof. Hans J. Herrmann
2008 - 2011	Private Tutor for Mathematics, Physics and Heat Transfer, Self-employed, Iran
2008 - 2008	Internship as Process Engineer at Ramak Dairy Company, Iran: Research and Development

Peer-reviewed publications

- F. Mohseni, M. Mendoza, S. Succi, and H.J. Herrmann. Relativistic effects on the Richtmyer-Meshkov instability. *Phys. Rev. D*, 90: 125028, 2014.
- S. Succi, M. Mendoza, F. Mohseni, and I. Karlin. Relativistic lattice kinetic theory: recent developments and future prospects. *Eur. Phys. J. Special Topics*, 223:2177, 2014.
- F. Mohseni, M. Mendoza, S. Succi, and H.J. Herrmann. Lattice Boltzmann model for ultrarelativistic flows. *Phys. Rev. D* 87:83003, 2013.
- H. Aminfar, M. Mohammadpourfard, and F. Mohseni. Two-phase mixture model simulation of the hydro-thermal behavior of an electrical conductive ferrofluid in the presence of magnetic field. *J. Magn. Magn. Mater.* 324:839, 2012.
- H. Aminfar, M. Mohammadpourfard, and F. Mohseni. Numerical investigation of thermocapillary and buoyancy driven convection of nanofluids in a floating zone. *Int. J. Mech. Sci.* 65:147, 2012.

Publications in review process

- F. Mohseni, M. Mendoza, S. Succi, and H.J. Herrmann. Lattice Boltzmann model for resistive relativistic magnetohydrodynamics, in review process.

Attended conferences and summer schools

- 23th International Conference on Discrete Simulation of Fluid Dynamics, DSFD 2014. Place: Paris, France. Type: Oral presentation. Date: 28th of July to 1st of August 2014.
- 51st Culham Plasma Physics Summer School. Place: Culham Science Centre, Oxford, UK. Type: Attendance. Date: 14th to 25th of July 2014.
- 19th Conference of Iranian Society of Mechanical Engineering, ISME 2011. Place: Birjand, Iran. Type: Oral presentation. Date: 10th to 13th of May 2011.